universität wien

DISSERTATION / DOCTORAL THESIS

Titel der Dissertation /Title of the Doctoral Thesis

Modifying low-dimensional materials using energetic charged particles

verfasst von / submitted by

Mukesh Tripathi

angestrebter akademischer Grad / in partial fulfilment of the requirements for the degree of

Doktor der Naturwissenschaften (Dr. rer. nat.)

Wien, 2019

Studienkennzahl lt. Studienblatt / degree programme code as it appears on the student record sheet:	A 796605411
Dissertationsgebiet lt. Studienblatt / field of study as it appears on the student record sheet:	Physik
Betreut von / Supervisors:	Ass.-Prof. Dr. Toma Susi Assoc.-Prof. Dr. Jani Kotakoski

Abstract

Low-dimensional materials including graphene, single-layer transition metal dichalcogenides and carbon nanotubes have attracted significant attention due to their unique intrinsic properties. To fully exploit their potential for novel applications, these properties need to be tailored. Defect engineering via electron and ion irradiation is one way to achieve this in a controlled way. While aberration-corrected scanning transmission electron microscopy (STEM) can be used to image such modified structures, it has also proven capable of manipulating individual impurity atoms in covalently bound materials using its Å-sized focused beam.

First, we demonstrated the incorporation of so far the heaviest reported impurity, Ge, into single-layer graphene via low-energy ion implantation. Atomic resolution STEM imaging revealed that despite its size, Ge can directly substitute single carbon atoms. Since sample contamination is a challenge in studies like this, we developed vacuum annealing methods to mitigate it. Next, we induced nanopores in both molybdenum and tungsten disulfide via highly charged Xe ion irradiation. By varying the ion parameters, the size of the pores could be controlled. We further showed that nanopores are also intrinsically present along grain boundaries of chemically grown single-layer molybdenum disulfide, with a size distribution dependent on the grain misorientation angle.

Finally, we used aberration-corrected STEM to both observe and control the electron-beam driven dynamics of various heteroatoms in graphene and single-walled carbon nanotubes. Atomic resolution imaging revealed both atom-conserving and non-conserving dynamics under electron irradiation, which has implications for the fabrication of nanostructures. We further explored electron-beam manipulation of silicon and phosphorus impurities within single-layer graphene. Individual silicon atoms could be precisely moved over hundreds of lattice sites, whereas phosphorus atoms are more challenging to move. Manipulation of silicon was also achieved in single-walled carbon nanotubes.

Even with manual operation, the rate of electron-beam manipulation is already comparable to the state-of-the-art in any atomically precise technique including scanning probe microscopy, demonstrating the great potential of STEM for atomic engineering of low-dimensional materials.

Zusammenfassung

Niedrigdimensionale Materialien, wie Graphen, Übergangsmetalldichalkogenid-Monoschichten und Kohlenstoffnanoröhren sind aufgrund ihrer einzigartigen Eigenschaften Gegenstand aktueller Forschung. Damit diese Materialien ihr gesamtes Potential entfalten können, müssen ihre Eigenschaften für die Verwendung in modernen Anwendungen zugeschnitten werden. Eine Möglichkeit dies gezielt durchzuführen ist die Bestrahlung mit Elektronen oder Ionen. Einerseits kann aberrationskorrigierte Rastertransmissionselektronenmikroskopie (STEM) dazu verwendet werden solche veränderten Strukturen abzubilden, andererseits hat sich gezeigt, dass man mithilfe dieser auch in der Lage ist einzelne Fremdatome innerhalb eines kovalent gebundenen Materials gezielt zu verschieben.

Zuerst wurde gezeigt, dass es möglich ist durch Beschuss mit niedrigenergetischen Ionen Germanium als Fremdatom in Graphen zu implantieren. Atomar aufgelöste STEM Bilder zeigen, dass Germaniumatome trotz ihrer Gröe einzelne Kohlenstoffatome substituieren können. Da die Verunreinigung der Proben durch die Bestrahlung eine der gröten Herausforderungen bei der skizzierten Vorgangsweise ist, wurde ein Vakuumglühverfahren entwickelt, um den Verunreinigungsprozess abzuschwächen. Auerdem wurden Nanoporen in Molybdän- und Wolframdisulfid mittels hochionisierter Xe-Atome erzeugt. Durch verändern der Bestrahlungsparameter konnte die Gröe der Poren kontrolliert werden. Weiters wurde gezeigt, dass Nanoporen auch intrinsisch an Korngrenzen von Molybdändisulfid vorkommen und deren Gröenverteilung vom Missorientierungswinkel zwischen den Körnern abhängt.

Zuletzt wurde ein STEM verwendet, um elektronenstrahlinduzierte Dynamiken verschiedener Heteroatome in Graphen und einwandigen Kohlenstoffnanoröhren, sowohl zu beobachten als auch mit atomarer Präzision zu kontrollieren. Atomar aufgelöste Bilder zeigen Prozesse, bei denen sich die Anzahl der Atome ändert, als auch solche bei denen diese konstant bleibt. Dies hat Auswirkungen auf die Herstellung von Nanostrukturen. Der Elektronenstrahl wurde verwendet, um Silizium- und Phosphor-Fremdatome in Graphen gezielt zu verschieben. Einzelne Silizium-Fremdatome konnten kontrolliert hunderte Gitterstellen weit verschoben werden. Dies wurde auch in einwandigen Kohlenstoffnanoröhren gezeigt.

Auch mit manueller Steuerung ist die elektronenstrahlinduzierte Sprungrate der Fremdatome auf einer Ebene mit anderen hochmodernen atomar auflösenden Methoden, wie Rastersondenmikroskopie. Dies zeigt das enorme Potential von STEM für die Nanotechnik.

Acknowledgements

This journey would not have completed without the support of many people involved in the process, without whom this thesis would not have been possible not just in terms of direct contributions but also the moral support throughout my research. First and foremost I would like to express my sincere gratitude to Prof. Toma Susi, not only for his tremendous academic support, encouragement, knowledge, enthusiasm, patience over three years and valuable insights into the project, but also providing me with many wonderful opportunities to attend conferences during my PhD.

I would like to express similar profound gratitude to Prof. Jani Kotakoski, who has been incredibly supportive and encouraging right from the beginning in ways both personal and professional. His immense knowledge, insightful comments and ideas have provided valuable inputs to my PhD study. I really enjoyed discussing with him and I am truly indebted for his generous support. I was very lucky to get the opportunity to learn from both Prof. Susi and Prof. Kotakoski as my advisors and mentors. A collective guidance from both of them has helped me throughout my PhD, including the writing of this thesis. I would also like to thank Prof. Jannik C. Meyer for useful discussions and gratefully appreciate and acknowledge Dr. Clemens Mangler for his support throughout, and for making sure the microscope is working at optimal performance.

I would like to thank all my former and present colleagues: Dr. Kimmo Mustonen, Dr. Alexander Markevich, Dr. Giacomo Argentero, Dr. Andreas Mittelberger, Dr. Kenan Elibol, Christoph Hofer, Georg Zagler, Heena Inani, Alex Chirita, Rajendra Singh, and Andreas Postl, who have been very supportive. A special mention goes in particular to Ursula Ludacka for helping me with administrative matters at the beginning of my PhD, and Gregor Leuthner and Thuy An for translation of the abstract of this thesis into German. It was amazing to work with all of them. Finally I would like to acknowledge Ms. Regina Pinter for all the administrative support, she has been extremely helpful. Last but not the least, I am grateful to my friends and family for their unconditional support.

Contents

List of acronyms

1 Introduction **1**
1.1 Materials . . . 1
1.1.1 Graphene . . . 1
1.1.2 Carbon nanotubes . . . 3
1.1.3 Transition metal dichalcogenides . . . 4
1.2 Defects in 2D materials . . . 6
1.2.1 Point defects . . . 6
1.2.2 Line defects and nanopores . . . 9
1.3 Outline . . . 11

2 Experimental methods **13**
2.1 Transmission electron microscopy . . . 13
2.1.1 Energy-dispersive X-ray spectroscopy . . . 14
2.2 Scanning transmission electron microscopy . . . 16
2.2.1 Annular dark field imaging . . . 16
2.2.2 Electron energy loss spectroscopy . . . 17
2.2.3 Nion UltraSTEM100 . . . 18
2.3 Sample preparation . . . 20
2.3.1 Mechanical exfoliation . . . 20
2.3.2 Chemical vapor deposition . . . 20
2.3.3 Preparing freestanding samples . . . 22
2.4 *Ex-situ* and *pre-situ* annealing . . . 25
2.5 Defect engineering using charged particles . . . 27
2.5.1 Defect engineering using ions . . . 28
2.5.1.1 Low-energy ion implantation . . . 28
2.5.1.2 Highly charged ion irradiation . . . 31
2.5.2 Defect engineering using electrons . . . 33
2.5.2.1 Electron-beam manipulation . . . 34

3 Results **37**
3.1 Sample cleaning 37
3.1.1 Untreated samples 37
3.1.2 *Ex-situ* cleaning 38
3.1.2.1 Air annealing 38
3.1.2.2 Vacuum annealing 39
3.1.3 *Pre-situ* cleaning 42
3.2 Nanopores in transition metal dichalcogenides 47
3.2.1 MoS_2 and WS_2 nanopores by highly charged ions 47
3.2.2 Intrinsic nanopores along MoS_2 grain boundaries 53
3.3 Implanting germanium into graphene 59
3.4 Beam-driven dynamics at heteroatom sites 64
3.4.1 Pyridinic nitrogen in graphene 65
3.4.2 Phosphorus and germanium substitutions in graphene . 67
3.4.3 Silicon impurities in graphene and SWCNTs 69
3.5 Electron-beam manipulation of impurities 74
3.5.1 Manipulation of impurities in graphene 74
3.5.2 Manipulation of Si in SWCNTs 81

4 Summary **85**

List of publications **87**

Contributions to scientific events **91**

Bibliography **108**

List of acronyms

0D zero-dimensional

1D one-dimensional

2D two-dimensional

3D three-dimensional

ADF annular dark field

AFM atomic force microscopy

BF bright field

CNT carbon nanotube

CBED convergent beam electron diffraction

CCD charge-coupled device

CFEG cold field emission gun

CVD chemical vapor deposition

DFT density functional theory

EBIT/EBIS electron beam ion trap/ion source

EDX energy-dispersive X-ray

EELS electron energy loss spectroscopy

FFT fast Fourier transform

FOV field of view

GPA geometric phase analysis

GB grain boundary

HAADF high angle annular dark field

hBN hexagonal boron nitride

HCI higly charged ion

IPA isopropyl alcohol

MAADF medium angle annular dark field

MoS_2 molybdenum disulfide

MWCNT Multi-walled carbon nanotube

PMMA poly(methyl 2-methylpropenoate)

QF Quantifoil®

SAED selected-area diffraction

STEM scanning transmission electron microscopy

STM scanning tunneling microscopy

SW Stone-Wales

SWCNT single-walled carbon nanotube

TEM transmission electron microscopy

TMD transition metal dichalcogenides

UHV ultra-high vacuum

WS_2 tungsten disulfide

ZLP zero-loss peak

Chapter 1

Introduction

Low-dimensional materials including graphene, transition metal dichalcogenides (TMDs) and single-walled carbon nanotubes (SWCNTs) can be used for many novel applications due to their unique intrinsic properties. However, these often need to be modified, and defect engineering via ion and electron irradiation is one way to accomplish this. To control structural modification on the atomic scale by individual impacts, it is necessary to understand defect creation in detail, which still remains a challenge. In this thesis, I will explore low-energy ion implantation and highly charged ion irradiation as means to modify low-dimensional materials. Further, I will use aberration-corrected scanning transmission electron microscopy (STEM) to image atomic structures, reveal their dynamics and to manipulate individual impurity atoms.

1.1 Materials

1.1.1 Graphene

Graphite is a three-dimensional (3D) allotrope of carbon that is abundant in nature and has been studied since the sixteenth century. Two-dimensional (2D), one-dimensional (1D) or zero-dimensional (0D) materials change their electronic structure compared to bulk 3D crystals. 2D materials were presumed not to exist in free state and believed to be thermodynamically unstable due to thermal fluctuations in the low-dimensional crystal lattice [1, 2]. Although the existence of the one-atom-thick 2D crystal graphene was studied theoretically [3], experimentally it was not shown until Andre Geim and Kostya Novoselov isolated a single layer of graphite using adhesive tape in 2004 at the University of Manchester [4]. Graphene is the first observed 2D material and has attracted significant attraction since its discovery due to its unique physical properties. Conceptually, a graphene sheet can be wrapped into 0D fullerenes, rolled into 1D nanotubes, and stacked into 3D graphite with weak interlayer coupling.

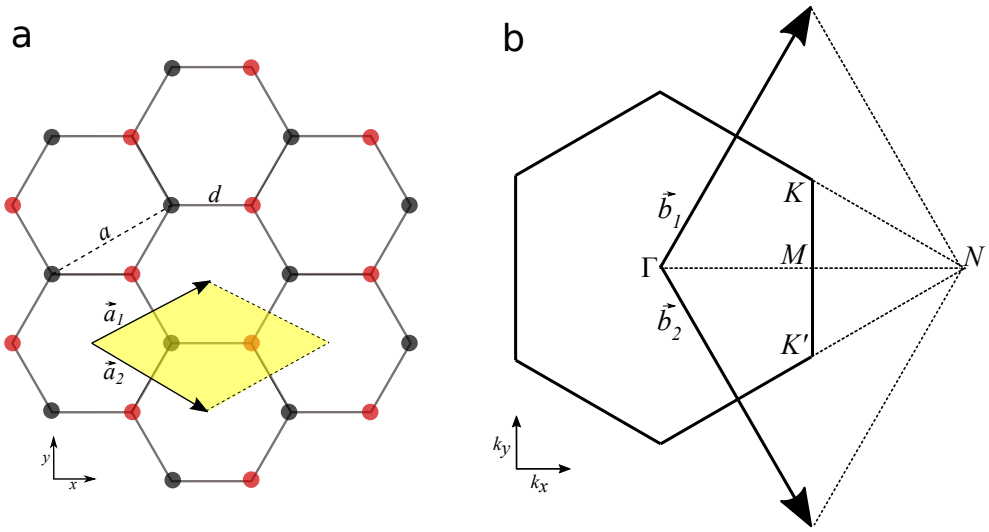

Figure 1.1: Honeycomb lattice structure of graphene and its first Brillouin zone with corresponding symmetry points. (a) Lattice structure of graphene, made of two interpenetrating triangular lattices; $\vec{a}_1$ and $\vec{a}_2$ are the unit vectors. The unit cell is highlighted in yellow. The lattice constant a is 2.46 Å. The interatomic distance d is 1.42 Å. (b) Corresponding first Brillouin zone.

Graphene is a one-atom thin plane of sp^2 hybridized carbon atoms arranged in a honeycomb lattice. This lattice is not a Bravais lattice because the two neighbouring sites are not equivalent, but consists of two sublattices marked with red and black circles in Figure 1.1a. The sp^2 hybridization between one s orbital and two p orbitals make a trigonal planar structure with the formation of σ bonds between the three neighbouring carbon atoms. These bonds are aligned at 120° angles in a single plane, and the fourth valence electron arranges in the unaffected p orbital perpendicular to it [5], leading to the formation of π bonding forming the valence and conduction bands in graphene.

The real-space unit vectors can be written as

$$\vec{a}_1 = \frac{d}{2}\left(3, \sqrt{3}\right), \quad \vec{a}_2 = \frac{d}{2}\left(3, -\sqrt{3}\right), \tag{1.1}$$

where $d = 1.42$ Å is the carbon-carbon distance. The corresponding reciprocal lattice vectors $\vec{b}_1$ and $\vec{b}_2$ are rotated by 30° with respect to the lattice orientations as shown in Figure 1.1b and are written as

$$\vec{b}_1 = \frac{2\pi}{3d}\left(1, \sqrt{3}\right), \quad \vec{b}_2 = \frac{2\pi}{3d}\left(1, -\sqrt{3}\right). \tag{1.2}$$

The first Brillouin zone of graphene is a hexagon, with its center Γ and the two inequivalent points (K and K′) of a triangular lattice in the reciprocal space. The high-symmetry K and K′ points in the corners of the Brillouin zone are also called Dirac points. These play an important role in the electronic transport of graphene. The positions of the Dirac points in momentum space are

$$\vec{K}' = \left(\frac{2\pi}{3d}, \frac{2\pi}{3\sqrt{3}d}\right), \quad \vec{K} = \left(\frac{2\pi}{3d}, -\frac{2\pi}{3\sqrt{3}d}\right). \tag{1.3}$$

The electronic properties of graphene vary significantly with the number of layers (monolayer to few-layer graphene and bulk graphite) [6]. Electrons in monolayer graphene are massless relativistic fermions that exhibit a linear dispersion near the Dirac point, whereas in bilayer graphene, they are non-zero effective mass Dirac fermions with a parabolic dispersion [7].

Its unique intrinsic properties [4, 8–10] make graphene attractive for many potential applications. In combination with large-scale fabrication of high-quality single-crystal graphene films [11] they make it also the ideal material for many practical applications ranging from optoelectronics [12] to sample supports for electron microscopy [13]. Due to high transmittance (97.7 %) of incident white light in the visible spectrum and its electronic structure, graphene can be used in flexible displays and touch screen applications [14].

1.1.2 Carbon nanotubes

Carbon nanotubes (CNTs) are composed of carbon, bonded in a hexagonal structure, with each atom covalently sp^2 bonded to three other carbon atoms. They are categorized as single-walled nanotubes (SWCNTs) and multi-walled nanotubes (MWCNTs) [15, 16]. A SWCNT is a sheet of graphene rolled into a cylinder with a high aspect ratio. A MWCNT is multiple layers of rolled graphene sheets like tubes within tubes. CNTs are considered as 1D as their length-to-diameter ratio is very high.

Depending on the orientation of graphene upon rolling into a cylinder, there are three different symmetries of SWCNT: armchair (n,n), zigzag (n,0) and chiral (n,m), as shown in Figure 1.2. The structure of a nanotube can be specified by the chiral vector $C_h = na_1 + ma_2$ (a_1 and a_2 are the unit cell vectors of graphene in real space) in terms of the integers (n,m), which define how the graphene sheet is rolled up [17]. SWCNTs can be synthesized using arc-discharge, laser ablation or chemical vapor deposition methods and tubes can be semiconducting or metallic depending on the the chiral angle and radius of the tube.

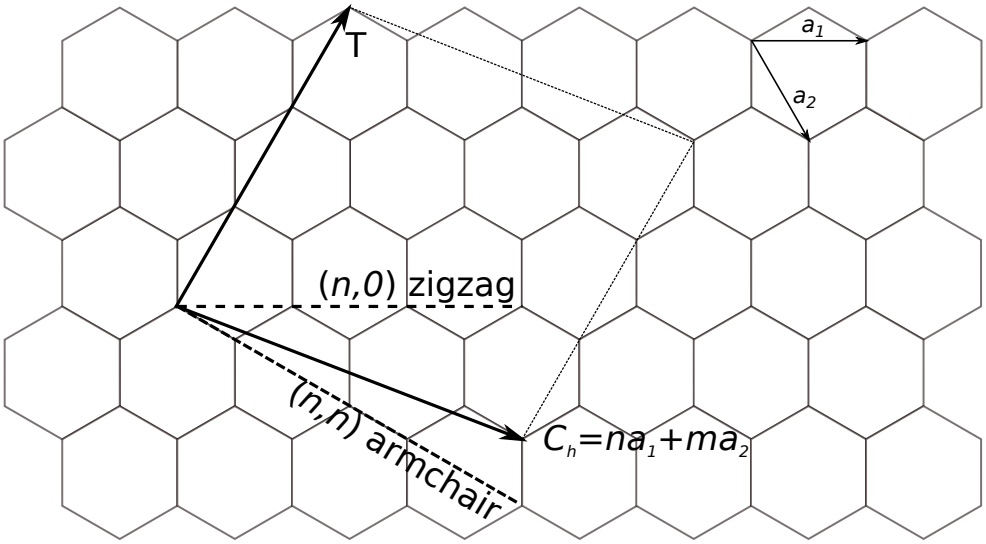

Figure 1.2: Schematic illustration of the construction of SWCNTs by rolling a graphene sheet along lattice vectors a_1 and a_2, which leads to armchair, zigzag, and chiral tube symmetry.

1.1.3 Transition metal dichalcogenides

Beyond graphene, other 2D materials such as transition metal dichalcogenides (TMDs) are significant because of their complementary properties. TMDs are MX_2 type compounds where M is a transition metal (Mo, W) and X is a chalcogen atom (S, Te). The transition metal atoms are sandwiched between two chalcogen atomic layers. TMDs can be semiconducting, metallic and even superconducting. TMDs have strong in-plane bonds and weak van der Waals bonds between the layers, leading to anisotropic properties.

MoS_2 has been one of the most studied members of the TMD family and used in the bulk form as dry lubricant since the late 1960s. A single layer of MoS_2 forms a hexagonal crystal structure consisting of two sulfur (S) atomic layers and one atomic layer of molybdenum (Mo) in between in a trigonal prismatic arrangement as shown in Figure 1.3. The in-plane lattice constant is 3.18 Å, and the lengths for Mo-S and Mo-Mo bonds are 2.4 Å and 3.16 Å, respectively. The distance between the upper and lower sulfur atoms is 3.1 Å.

Bulk MoS_2 is semiconducting with an indirect bandgap of 1.2 eV, whereas single-layer MoS_2 has a direct bandgap of 1.8 eV [18, 19]. The most common crystal phase configurations for MoS_2 are hexagonal (2H), octahedral (1T) and rhombohedral (3R). The metastable 1T form shows metallic behavior, while both 2H and 3R forms exhibit semiconducting behavior. Because graphene lacks an electronic band gap, MoS_2 has attracted significant attention for its fascinating semiconducting properties and potential applications in biosensors [20], and nanoelectronics and optoelectronics [21].

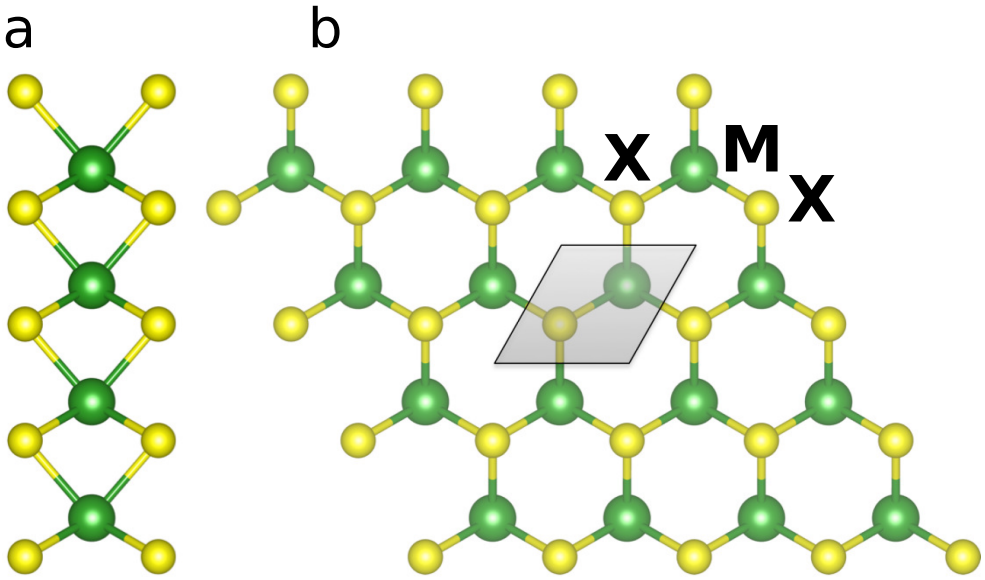

Figure 1.3: The atomic structure of monolayer trigonal prismatic (2H) transition metal dichalcogenides (TMDs). (a) Side view. (b) Top view. M is a transition metal (Mo, W) and X is a chalcogen atom (S, Se, Te). Image is reused with permission from Ref. [24] (CC-BY).

Tungsten disulfide (WS_2) also belongs to the TMD family and is similar to MoS_2 in structure. Monolayer WS_2 is formed by two S layers and one atomic layer of tungsten (W) in a trigonal prismatic arrangement. The lattice constant is 3.18 Å. The W-W bond length is 3.15 Å. Depending on the arrangements of W and S atoms and stacking between layers, WS_2 also has 2H, 1T and 3R phases. Similar to MoS_2, the electronic structure of WS_2 is sensitive to the number of layers, exhibiting an indirect-to-direct band gap transition from the bulk form to a single layer [22]. Monolayer WS_2 has attracted significant interest for use in optical devices due to its direct bandgap and high photoluminescence intensity [23].

Similar to graphene, the isolation of few-layer and even single-layer 2D crystals was shown by the micromechanical cleavage technique using adhesive tape [25], as layers are stacked together with weak van der Waals interactions. In addition to mechanical exfoliation, several other synthesis methods such as liquid phase exfoliation and chemical vapor deposition (CVD) have been used for the large-scale production of single-layer MoS_2 and WS_2 sheets even on arbitary substrates [26, 27].

1.2 Defects in 2D materials

"*Crystals are like people, it is the defects in them which tend to make them interesting*"- Colin Humphreys.

Defects are discontinuities in the crystal lattice that break the lattice symmetry, caused often by missing or additional atoms or ions. It is well known that structural defects exist in practically all materials and can significantly alter their properties. However, defects are not always detrimental but can also be beneficial for tailoring the properties of materials to enhance their functionalities. Similar to bulk crystals, also low-dimensional materials are not free from atomic-scale defects [1, 2, 28]. Therefore, it is important to understand these structural defects and their influence on fundamental electronic, optical, thermal, magnetic and mechanical properties of the materials [28].

Defects can also be deliberately introduced into 2D materials using techniques such as chemical methods and electron or ion irradiation to modify them and to achieve desirable properties. I will discuss the techniques used for defect engineering for this thesis in detail in Section 2.5.

Different structural defects observed in 2D materials can be mainly classified as point or line defects. Point defects can be further categorized in bond rotations such as the Stone-Wales defect, single, double and multiple vacancies, foreign adatoms and substitutional impurities. Point defects can be created with energetic particles such as electron or ion irradiation in graphene [29, 30] and in other 2D materials such as TMDs [31]. Due to electron irradiation of TMDs, single S vacancies may agglomerate and form line defects [31].

1.2.1 Point defects

The graphene lattice can be locally reorganized into nonhexagonal rings by a 90° rotation of two carbon atoms with respect to the midpoint of their bond, resulting in the transformation of four hexagons into two heptagons and two pentagons. This is called a Stone-Wales transformation [29, 32]. Stone-Wales defects are the most elementary topological disorder in graphene and do not involve any removal or addition of carbon atoms or dangling bonds. In contrast to graphene, Stone-Wales defects are not commonly observed in other 2D materials, for example TMDs, but similar defects can be formed by sequential rotations of metal-chalcogen bonds in the trigonal prismatic lattice [33].

Single vacancies are one of the simplest defects in any material, defined by one missing lattice atom. For example in graphene, upon removal of a single atom from lattice, either the distorted bonds remain as dangling bonds or the structure undergoes a bond reconstruction through a Jahn-Teller rearrangement, forming a five-membered and a nine-membered ring [28]. However, single vacancies are not very common and have seldom been observed due to their diffusion [34] and reactivity.

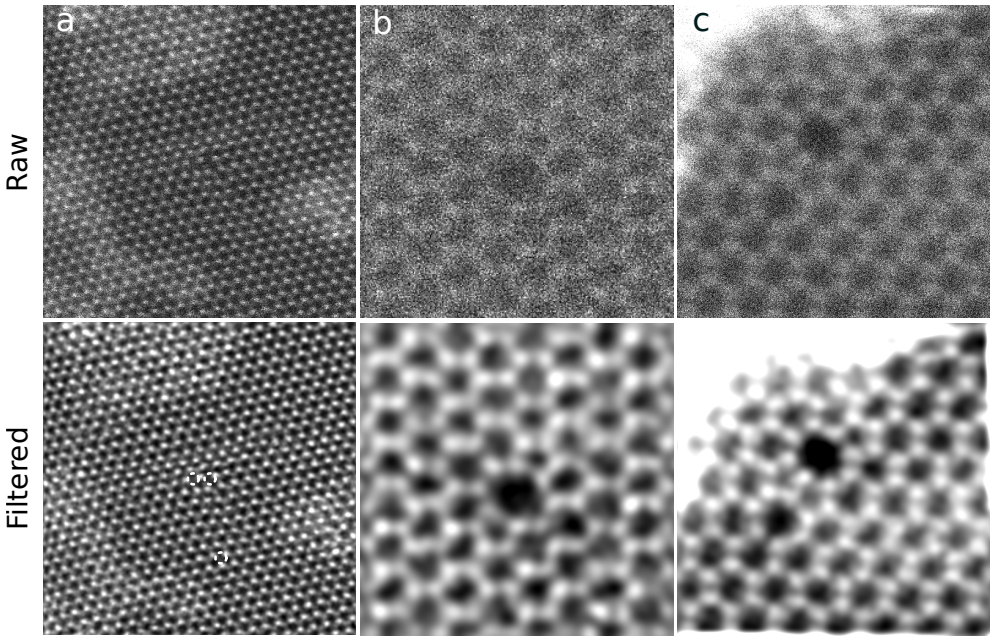

Figure 1.4: Defects in MoS_2 (a) and in graphene (b,c) as observed in scanning transmission electron microscopy images. Images in the bottom row have been processed using double Gaussian filtering [35]. Point defects in MoS_2 have been highlighted with white circles on the filtered image of panel a. Panel b shows a divacancy and panel c a more complex defect structure.

Double vacancies are created by merging two single vacancies or by removing two neighboring carbon atoms from the lattice. After structural rearrangement, four hexagons are replaced by two pentagons and one octagon with no dangling bonds. The defect can further transform into more complex reconstructions such as a combination of three pentagons and three heptagons or of three pentagons, one hexagon and three octagons [36]. As an example, Figure 1.4b shows a divacancy in graphene. Double vacancies are more energetically favorable than single vacancies and can migrate in graphene [28, 36]. In the case of TMDs, the most abundant defects are chalcogen single or double vacancies and metal atom vacancies in combination with three or all six of its neighboring chalcogen missing atoms [37, 38]. As an example, single sulfur vacancies (marked with white circles) in MoS_2 are presented in Figure 1.4a.

Heteroatoms are present in real-life samples due to their growth and the subsequent transfer process, probably because of the use of various chemicals or glassware for example in chemical vapor deposition of graphene. Impurities can also be introduced deliberately by substituting one or few atoms in the lattice either using chemical routes or ion irradiation. Intentional doping with heteroatoms can modify the electronic structure, leading to a band gap

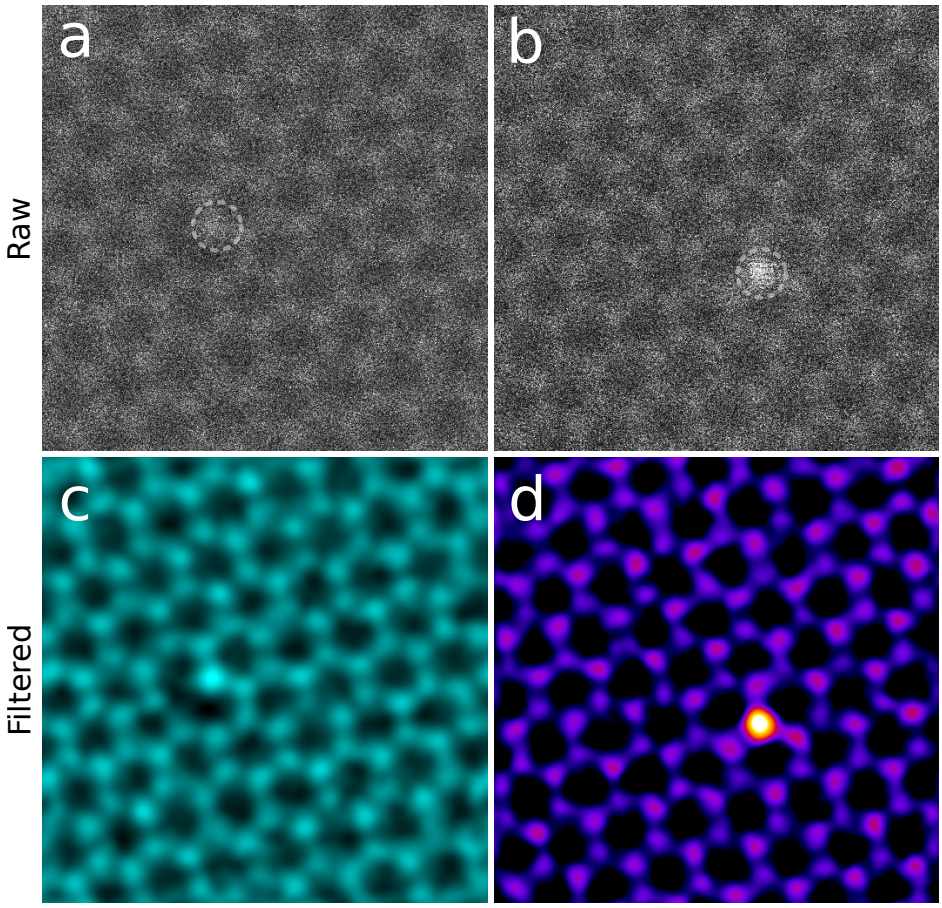

Figure 1.5: Heteroatoms in graphene. Scanning transmission electron microscopy raw and filtered images showing a nitrogen atom in a vacancy site (a) and a substituted silicon impurity in graphene (b). Heteroatoms have different contrast as highlighted by a circle in panels a & b, which will be explained in Chapter 2.

opening in graphene. Boron (B) and nitrogen (N) are the obvious choice for carbon atom substitution in graphene since they are its nearest neighbors in the periodic table, and their atomic size is close to carbon. After B and N dopant incorporation in CNTs [39], their atomic sites and the chemical nature of individual B and N dopants in graphitic configuration were directly observed in graphene [40, 41]. In addition to graphitic substitution, different atomic bonding configurations of nitrogen dopant atoms, known as pyridinic and pyrrolic, have been observed [42]. Much larger and heavier dopants in comparison to carbon, for example aluminum (Al) [43], silicon (Si) [44, 45], phosphorous (P) [46] and germanium (Ge) [47] can also substitute carbon atoms in graphene and form a stable configuration due to strong covalent

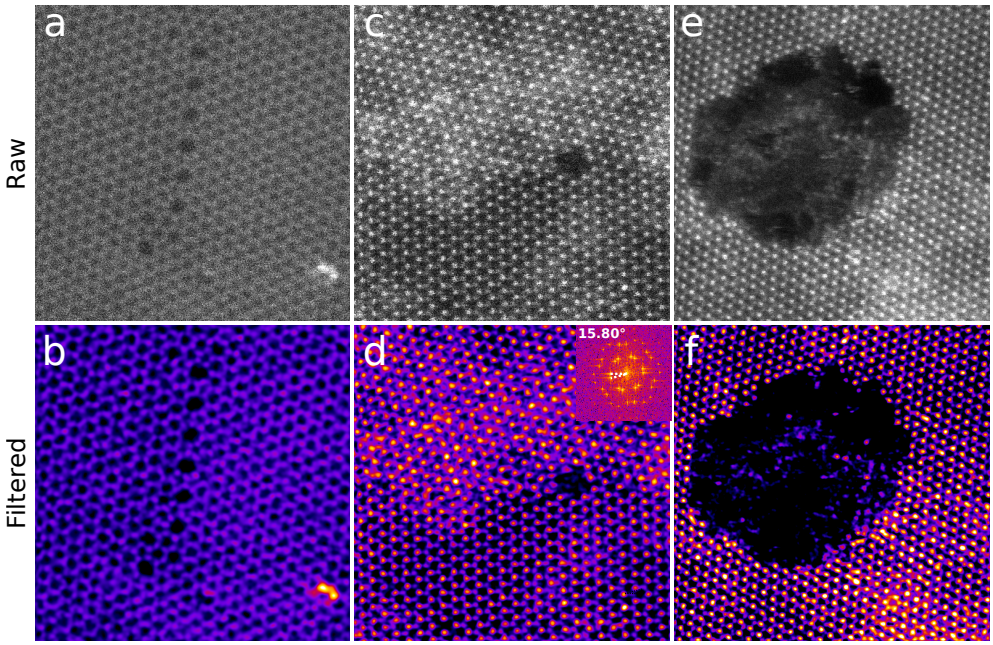

Figure 1.6: Scanning transmission electron microscopy raw and filtered images show a chain of vacancies in graphene (a,b), a grain boundary (c,d) and nanopores (e,f) in MoS_2. Fast Fourier transform (FFT) image in the inset of panel d shows a 15.80° misorientation angle between the two grains in MoS_2.

bonding. These heavier atoms reside in an out-of-plane configuration. Figure 1.5 shows N in pyridinic configuration and a silicon substitution. Dynamics of heteroatoms in graphene will be explored in detail in Chapter 3. Beyond graphene, dopants can also be incorporated in other 2D materials such as hexagonal boron nitride or TMDs [48].

In addition to a substitution, heteroatoms can also be adsorbed onto the surface of 2D materials as adatoms. In the case of graphene, they can form a covalent bond with the nearest carbon atoms if the interaction between the impurity and carbon is strong. Adatoms can form various configurations such as on top of an atom, on top of a center of a hexagon or the bridge position between two atoms, but they are rarely stable and tend to migrate and can fill vacant lattice sites [49].

1.2.2 Line defects and nanopores

In graphene, line defects may consist of a line of pairs of pentagons separated by octagons or heptagons, and can be formed by aligning divacancies along the zigzag or armchair lattice direction of graphene [50]. For TMDs, as discussed above, chalcogen vacancies are the most common defects. They tend

to agglomerate into lines as a chain of reconstructed point defects [38].

Grain boundaries are a topological disorder in the lattice that separate the domains of a material with different crystallographic orientations. Grain boundaries are formed when grains with different atomic orientations merge together during growth [51]. Grain boundaries can be viewed as periodic arrays of dislocation cores with pentagon-heptagon pairs with no dangling bonds forming a tilt boundary. In graphene, the migration of grain boundaries has been reported under electron irradiation [52]. In addition to chalcogen line defects, grain boundaries with various complex dislocation core structures such as a pentagon-heptagon, tetragon-tetragon, tetragon-hexagon and hexagon-octagon membered rings are often observed in TMDs, along with tilt and mirror twin boundaries [53–56]. Grain boundaries influence the properties and typically weaken the mechanical strength of the materials [57].

Nanopores are holes, either already present along grain boundaries due to a mismatch between different grains in the materials [55] or can be intentionally fabricated in suspended or free-standing 2D sheets using controlled electron or ion irradiation [58]. Despite the extreme thinness of the 2D sheets, nanopores are structurally robust and can find applications in DNA translocation and sequencing, chemical separation and water desalination [59]. Figure 1.6 shows a chain of vacancies in graphene (a,b), a grain boundary (c,d) and nanopores (e,f) in MoS_2.

1.3 Outline

In this thesis, I will first compare various heat treatments used to clean low-dimensional materials such graphene or SWCNTs. In particular, I will introduce a new *pre-situ* cleaning method. This technique uses radiative heating via a tungsten wire or laser in the same vacuum system as the electron microscope. To prove the effectiveness of these methods, I will show atomically resolved STEM images of clean graphene. I will then move to nanopores intrinsically present along the grain boundaries in single-layer MoS_2, showing how the pore areas linearly decrease until 15° misorientation angle and then increase again for higher angles.

The next part of my thesis is devoted to ion irradiation of two-dimensional materials, namely graphene and TMDs. Using highly charged Xe ions, the properties of freestanding monolayer MoS_2 and WS_2 can be tailored via the formation of roundish pores in MoS_2 and triangular pores with sharp edges in WS_2. I will further show how the radius of these pores can be controlled by the ion charge state and how the pore creation efficiency from each ion depends on the ion potential energy. Then, I will move to low-energy ion irradiation of graphene. I will present the implantation of germanium impurities, and show that despite being significantly larger in size than carbon atoms, they can directly substitute single C atoms.

Finally, aberration-corrected STEM is used for two different purposes: to reveal beam-induced dynamics on the atomic scale, and to manipulate individual impurity atoms with its focused electron beam. I will show greatly improved electron-beam manipulation of Si in graphene, explore the possibility of manipulating P, and for the first time show that Si can be manipulated also in SWCNTs. The results included in this thesis show that aberration-corrected STEM is an invaluable tool not only for the study of heteroatom dynamics but in some cases also for their manipulation with atomic precision.

Chapter 2

Experimental methods

In this Chapter, I will introduce the experimental methods that were used for the research presented in this thesis. First, I will describe transmission electron microscopy (TEM) and related spectroscopy techniques, concentrating on scanning TEM. Second, I will introduce sample synthesis, the preparation of freestanding samples, and the cleaning methods that were developed. Finally, I will describe defect engineering using charged particle irradiation, including both low-energy and highly charged ions as well as relativistic electrons.

2.1 Transmission electron microscopy

Transmission electron microscopy (TEM) is used to form images from thin samples by passing a parallel beam of electrons through the specimen in high vacuum. The formed image is magnified and focused onto an imaging system. The operating principle of a TEM is analogous to the light microscope. However, TEM has greater resolving power because it uses high-energy electrons, which have a much shorter wavelength ($\sim 10^{-12}$ m) than visible light (~ 0.4–0.7×10^{-6} m). A schematic illustration of electron trajectories inside a conventional TEM is shown in Figure 2.1.

It is convenient to discuss the fundamental components of a TEM in parts: an electron source, sample illumination (condenser lens), imaging system (objective lens), magnification and projection (intermediate and projector lenses) and detector. An electron gun emits electrons from a filament tip by either thermionic or field emission and then accelerates them by an electrostatic potential typically to an energy in the range of 30–300 kV. The electron beam then passes through the condenser system, where a set of electromagnetic lenses are used to control and direct the beam. At the sample, due to the scattering of an incident electron beam by the specimen, an image is formed when it passes through the objective lens. The objective lens in combination with the sample stage system is the heart of a TEM as they are responsible for image formation. Finally, the image is magnified using intermediate and

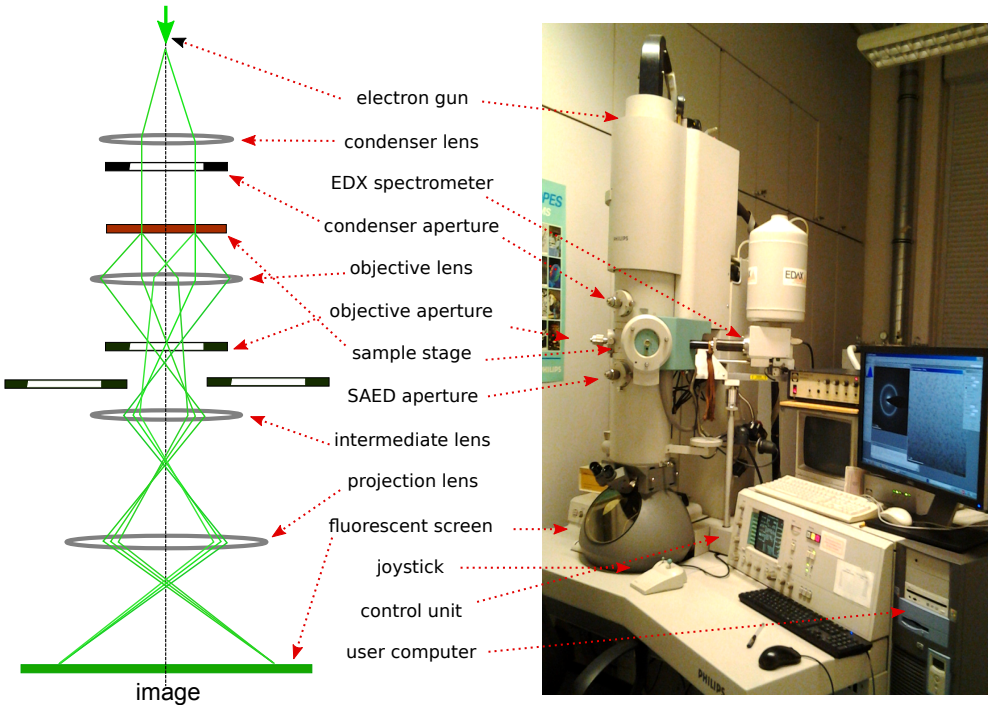

Figure 2.1: Simplified electron path ray diagram in a conventional transmission electron microscope, with a photograph of the Philips CM200 microscope.

projection lenses and viewed using a charged coupled device (CCD) camera or a fluorescent devices.

TEM can be operated in two principal modes; parallel and convergent beam. Parallel beam is mainly used for TEM imaging and selected-area diffraction (SAED) whereas convergent beam is used for scanning (STEM) imaging, X-ray and electron spectroscopy (EDX & EELS), and convergent-beam electron diffraction (CBED). In parallel beam imaging mode, intermediate and projector lenses magnify and project the image plane of the objective lens to the camera. In diffraction mode, intermediate and projector lenses magnify and project the back focal plane of the objective lens to the camera.

2.1.1 Energy-dispersive X-ray spectroscopy

Peaks in an energy-dispersive X-ray (EDX) spectrum are characteristic of the sample elemental composition, arising from atoms which have gone through core shell ionization after an interaction with the electron beam and transitioned from the ground state to a higher energy excited state leaving a hole behind. In the de-excitation process, electrons relax back to the ground state, releasing excess energy which corresponds to the difference between the energy

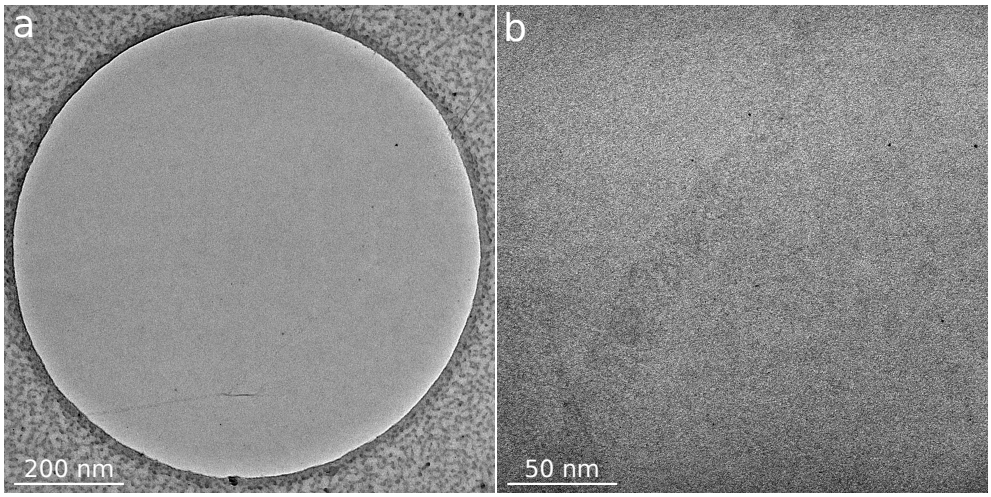

Figure 2.2: An example of bright-field imaging of suspended graphene at 80 kV acceleration voltage. Dark features in panel b show contamination covering the sample.

levels, and subsequently emit energetic photons that are called X-rays. The X-rays are detected by an EDX spectrometer. In terms of instrumentals, charge pulses generated by the detector are converted to a voltage proportional to the X-ray energy. These pulses translate the X-ray energy into a signal in a specific channel using a processor. The counts in the energy channels are then displayed as a spectrum and show peaks corresponding to the elemental composition [60]. Detectors are cooled with liquid N_2 to avoid noise from the electronics and to minimize electron-hole pair generation activated by thermal energy.

The TEM imaging, diffraction and EDX results contained in this thesis were obtained with a bench-top transmission electron microscope or "mini TEM"(Delong instruments LVEM5) and a conventional TEM (Philips CM200). The mini TEM was operated at 5 kV acceleration voltage. The CM200 contains a 80–200 kV electron gun, a sample stage (Compustage goniometer), an EDX spectrometer and heating holders for in-situ experiments. Figure 2.2a & b shows a bright-field (BF) image of a suspended graphene sheet at 80 kV.

2.2 Scanning transmission electron microscopy

STEM provides a greater control over the positioning of the beam and in the detection of useful signals in comparison to conventional TEM. In TEM, the electron beam is spread over the whole area of interest and the image is formed by an objective lens after the electrons are transmitted through the sample. In STEM, the electron probe is focused by probe-forming lens before the sample and then raster-scanned across it. Multiple detectors can be used simultaneously to collect the transmitted electrons from the sample at each point and to form the image. Spatial resolution in (S)TEM is limited due to lens aberrations. The development of spherical aberration correction in dedicated STEMs [61] provides advantages over TEM such as making it possible to achieve a focused electron probe around 1 Å in diameter to position on individual atoms.

Currently, dedicated aberration-corrected STEM provides the most analytical sensitivity at the highest spatial resolution [62, 63]. (Quasi-) elastically scattered electrons resulting from interactions with atomic nuclei are used for annular dark field (ADF) imaging (also called Z-contrast imaging) and detected by high angle annular dark field (HAADF) and medium angle annular dark field (MAADF) detectors. Inelastically scattered electrons mainly due to electron-electron interactions are mainly exploited for elemental analysis and phonon measurements using techniques such as EELS. Bright-field images can also be formed in STEM using transmitted electrons similar to TEM.

2.2.1 Annular dark field imaging

ADF imaging was introduced by Crewe [64] and refers to an image formed by an annular detector that collects electrons scattered to a specific angular range. The central region is a hole and the electrons passing through it can be used to form either a BF image or an electron energy loss spectrum. The scattering intensity of individual atoms is approximately proportional to Z^n, where Z is the atomic number and the exponent n is close to 1.6–1.8 [35]. For "true" Z-contrast, the imaging process needs to be incoherent and intensities detected by ADF detector to be integrated scattered intensities by each atom [65]. However, if the probe images more than one atom, image contrast increases leading to dependency on the atomic potential and sample thickness [66]. Images acquired with ADF detectors are much more strongly dependent on Z than phase-contrast images in TEM, which use a smaller scattering angle. The incoherent image formation process where only intensities are involved and interference between scattering from different regions does not influence the image contrast leads to a straightforward qualitative interpretation of atomic resolution ADF images. Therefore, ADF imaging in STEM is an extremely useful technique to probe the local atomic structure and defects, and for the direct identification of heteroatoms.

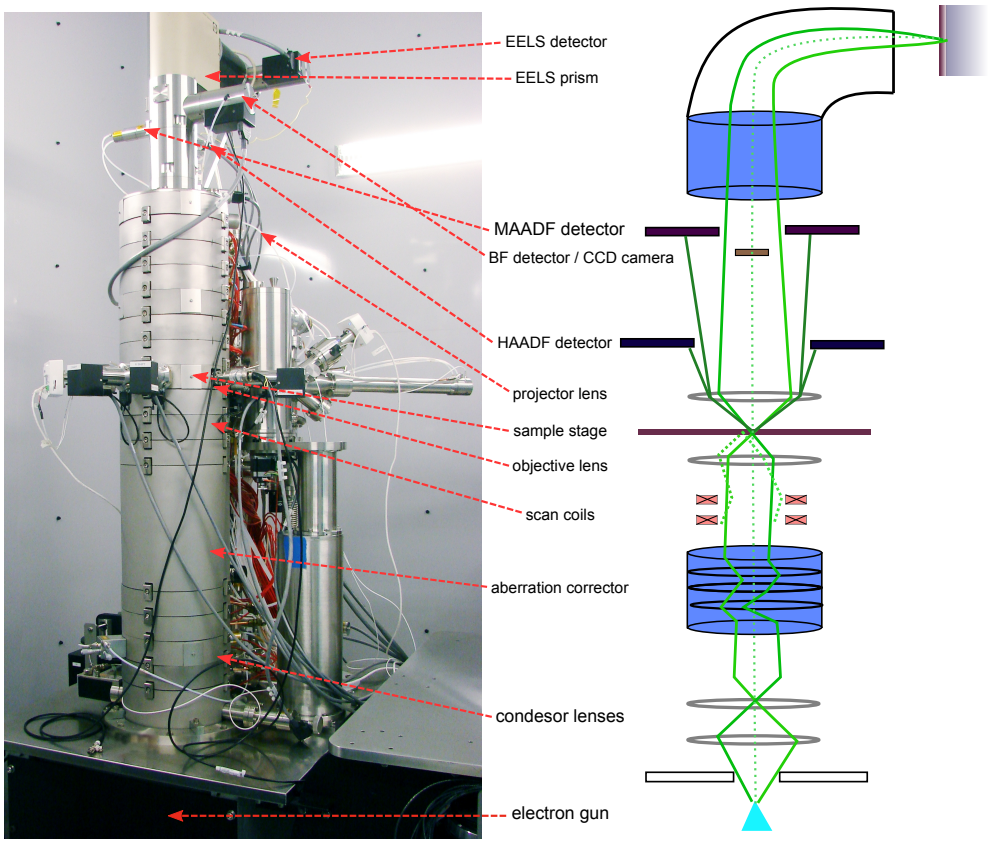

Figure 2.3: The Vienna Nion UltraSTEM100 before additional modifications and a simplified schematic of its important components with paths of electron rays through the instrument.

Residual aberrations can cause an extended tail in the electron beam shape. This spreading is in the probe tail can contribute peak intensities to the nearest-neighbor sites. In order to measure and compare atomic intensities, probe tail contribution can be removed using a double Gaussian filter [35]. It consist of one positive Gaussian which smooths the pixel-by pixel intensity variation by cutting off the spatial frequencies beyond those actually transferred by the microscope, and a negative Gaussian which adds a negative skirt to the image of each atom to null the extended probe tail at the location of the nearest neighbors [35].

2.2.2 Electron energy loss spectroscopy

EELS is a technique to measure the change in the kinetic energy of electrons as a result of inelastic scattering between the incident beam and sample, mainly due to electron-electron interactions. An EEL spectrum can be acquired when

the inelastically scattered intensities are dispersed as a function of kinetic energy by a magnetic prism spectrometer and focused on a scintillator that converts the electrons into visible light recorded by a CCD detector. EELS is commonly used to reveal chemical composition and electronic properties, sample thickness, bonding/valence state, free electron density and dielectric response [67].

An EEL spectrum is often divided into zero-loss, low-loss and high-loss regions. The zero-loss peak is the most intense feature in a spectrum and represents unscattered electrons. The full-width at half-maximum (FWHM) of the zero loss peak is used to measure the spectral resolution, which is limited by the energy spread of the source. With a CFEG source, the energy resolution is ∼0.3 eV. However, with electron monochromators, sub-10 meV energy resolution in EELS-STEM has been achieved [68].

The region after the zero-loss peak until about 50 eV is called the low-loss region. Plasmons, its most intense feature, are collective excitations of the weakly bound outer-shell electrons of the atoms. The plasmon peak position is sensitive to valence electron density and can be used to measure the thickness of the sample. Low-loss may also exhibit inter-band transitions between the valence and conduction bands.

The high (core) loss region in an EEL spectrum appears after 50 eV. Its characteristic features are called ionization edges and show a drastic rise followed by gradual decrease in signal with increasing energy. These edges are labeled in standard spectroscopic notation (e.g., K, L, M) and correspond to those electrons that have lost energy by excitation of the specimen's core shell electrons to states above the Fermi level. Thus the edge shape depends on the sample electronic structure. The ionization edges can be used for composition analysis for all elements except hydrogen [69]. In addition to chemical identification, ionization edges have intensity fluctuations above their edge onset, called the fine structure, which are sensitive to the local environment of the ionized atoms and can be used to probe their local bonding.

2.2.3 Nion UltraSTEM100

Figure 2.3 shows an image of a dedicated STEM and a simplified schematic illustration of the instrument. The microscope shown in this figure is a Nion UltraSTEM100 installed in Vienna that was used for most of the results presented in this thesis. As principal design elements, it uses a 100 kV high-brightness cold field emission electron gun (CFEG) and is equipped with a 3^{rd} generation C3/C5 aberration corrector. It has a minimum probe size of 1–1.3 Å at 60–100 kV acceleration voltages. The instrument is operated under ultra-high vacuum (UHV) conditions. The base pressure at the gun and sample is typically in the $\sim 10^{-11}$ mbar and 10^{-10} mbar range respectively, which is about two orders of magnitude lower than other commercially available (S)TEMs. It is equipped with two ADF detectors with semiangular ranges of

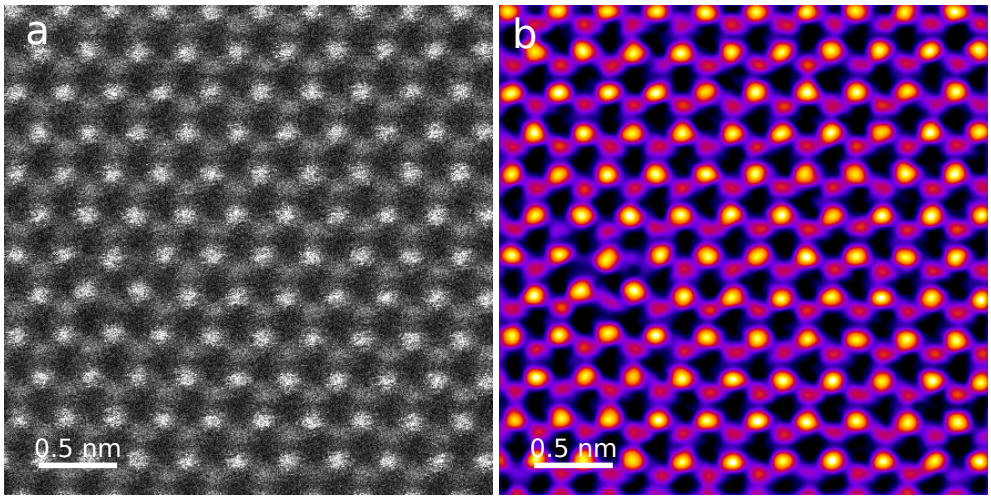

Figure 2.4: MoS_2 lattice. (a) shows a raw image of MoS_2 captured with a HAADF detector at 60 kV acceleration voltage. Since Mo atoms are heavier in comparison to S atoms, they appear brighter owing to their Z-contrast. (b) is obtained after post-processing the image by applying a double Gaussian filter. To highlight each atom, the image is colored using the ImageJ look–up table "fire".

60–200 mrad for MAADF and 80–300 mrad for HAADF, and a Gatan EEL spectrometer combined with an Andor iXon Ultra 897 electron-multiplying charge-coupled device (EMCCD) camera. For tuning and fine adjustment of the electron beam, a BF CCD camera is installed. A full description of the Nion UltraSTEM100 microscope can be found in Ref. [61]. The objective and sample stage have been customized by connecting an UHV line into the instrument. A high power laser or a tungsten wire has been fixed in this connected vacuum line for removing contamination from samples, which will be discussed later in this Chapter. As an example, an atomically resolved ADF image acquired with this microscope is presented in Figure 2.4.

2.3 Sample preparation

For this thesis, monolayer graphene samples grown via chemical vapor deposition (CVD) were used for most experiments. The samples were either grown by collaborators or commercially purchased graphene on Quantifoil® from Graphenea Inc. [70]. A small number of additional samples were produced by mechanical exfoliation.

2.3.1 Mechanical exfoliation

In mechanical exfoliation, graphene sheets are separated from a bulk graphite crystal. The mechanical exfoliation method was introduced by Geim and Novoselov in 2004 using highly oriented pyrolytic graphite and Scotch tape [4]. In this method, adhesive tape is repeatedly applied to a bulk crystal and peeled back (Figure 2.5a). Due to weak van der Walls attractions between the layers, they can easily detached from the graphite crystal. After peeling, the tape with thin crystals is placed on top of a SiO_2/Si substrate and gently pressed, resulting in the mechanical exfoliation of a monolyer or few-layer graphene flakes as shown in Figure 2.5b & c.

After exfoliation, an optical microscope can be used to search and identify the number of graphene layers (Figure 2.5d). The oxide thickness is selected to visualize the layers. In this thesis, wafers with 90 nm thick oxide were used. In our case, the optical contrast for monolayer graphene is ∼7%. It increases linearly with the number of layers (up to 5–7 layers) [71]. However, contrast may vary with different camera set ups and certain oxide thicknesses.

The quality of graphene flakes obtained by mechanical exfoliation is high in comparison to CVD-grown graphene. However, the layers vary significantly in thickness and size, ranging from nanometers to several tens of micrometers for monolyer graphene.

2.3.2 Chemical vapor deposition

During the CVD process, a carrier gas which is often a mixture of Ar and H_2 is fed into a quartz tube connected to a vacuum pump and gas inlet system and passes through a hot zone in a furnace, where hydrocarbon precursors such as methane (CH_4) decompose to carbon radicals at metal substrates (i.e. nickel or copper films) and subsequently form monolayer and few-layers graphene. CVD is the most widely used technique to synthesize graphene and significant advances have been made in optimizing growth parameters such as temperature, pressure, growth time, choice of precursor gas and substrate, preparation of the catalyst, flow rate and cooling rate [72, 73].

Monolyer MoS_2 films of high quality and large area were synthesized in a CVD microreactor setup in Dublin [26]. It utilizes a close-proximity precursor supply of liquid-phase exfoliated MoO_3 nanosheets dispersed in IPA solution

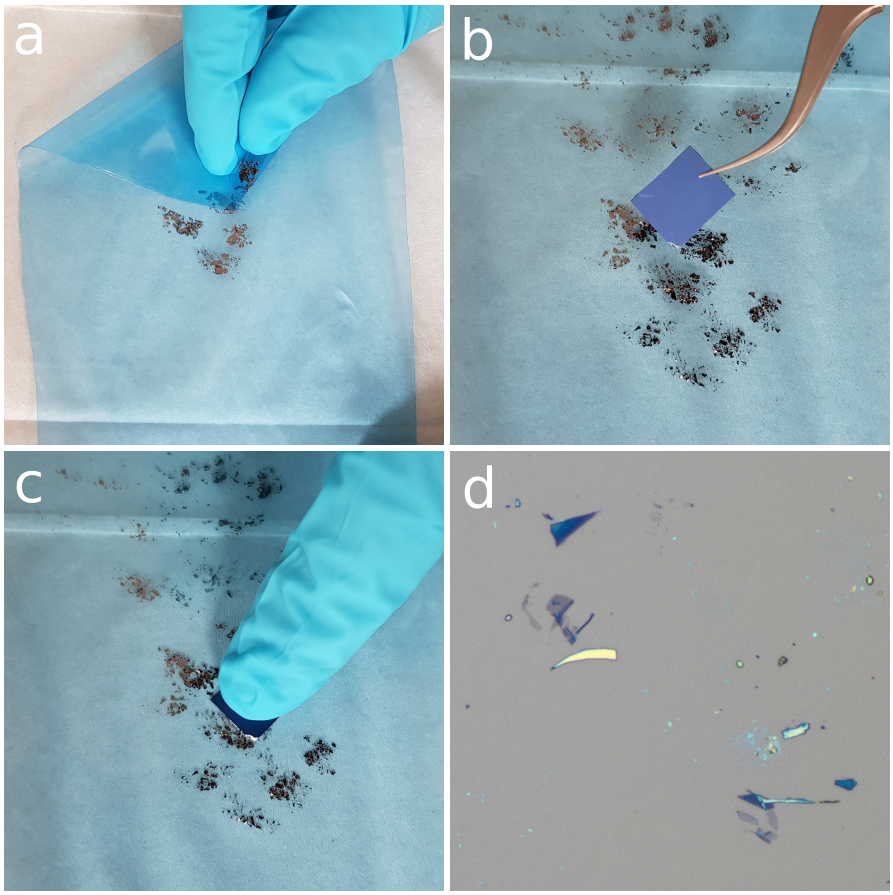

Figure 2.5: Mechanical exfoliation. (a) Layers are detached from a graphite cystal by opening and folding the adhesive tape. (b-c) Deposition of exfoliated flakes on top of a SiO_2/Si substrate. (d) Optical microscope image of exfoliated graphene on top of SiO_2/Si.

and drop-casted onto a substrate as precursor. A silicon substrate coated by 290 nm thick SiO_2 acts as a growth substrate in the quartz tube furnace. The samples sit in the hot zone of the furnace and sulfur powder as a reactant is heated up to vaporize it and passed to the samples using Ar as a carrier gas. Due to the reaction between MoO_3 and S in the vapor phase, nucleation of MoS_2 layers occurs directly on the substrate.

To synthesize single-walled carbon nanotubes, ethanol was used as the carbon source in a customized floating catalyst CVD reactor. As the catalyst precursor and growth promoter, ferrocene and thiophene were first dissolved in ethanol to form a liquid feedstock and then injected with a syringe pump. The solution was evaporated in a heating line and N_2 and H_2 were used as carrier gases. More detailed information on the growth process is given in Ref. [74].

2.3.3 Preparing freestanding samples

For this thesis, mechanically exfoliated graphene and MoS_2 films grown on SiO_2/Si substrates were transferred without polymer directly onto golden TEM grids coated with perforated amorphous carbon foil (Quantifoil®). Figure 2.6 shows a schematic illustration of the transfer process. Flakes are identified first in the optical microscope and a TEM grid is then placed directly on the target region of the substrate and a drop of IPA is evaporated on the TEM grid to enhance the adhesion between graphene and the carbon support of the grid. In the next step, to detach the flakes from the substrate, a few drops of potassium hydroxide (KOH) solution are released directly on top of the grid. After a few minutes, the KOH solution etches the SiO_2 layer and the TEM grid with the transferred flake detaches. As the last step, the grid is washed in de-ionized water to remove residuals and subsequently in IPA solution to dry.

To check whether the flakes were transferred successfully onto TEM grids, the samples were characterized using a bench-top electron microscope. Figures 2.7 & 2.8 show low-magnifiaction images of a suspended exfoliated graphene layer and suspended large MoS_2 single crystal films.

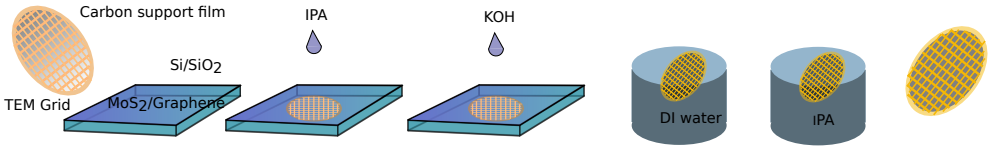

Figure 2.6: Schematic illustration of the direct transfer process.

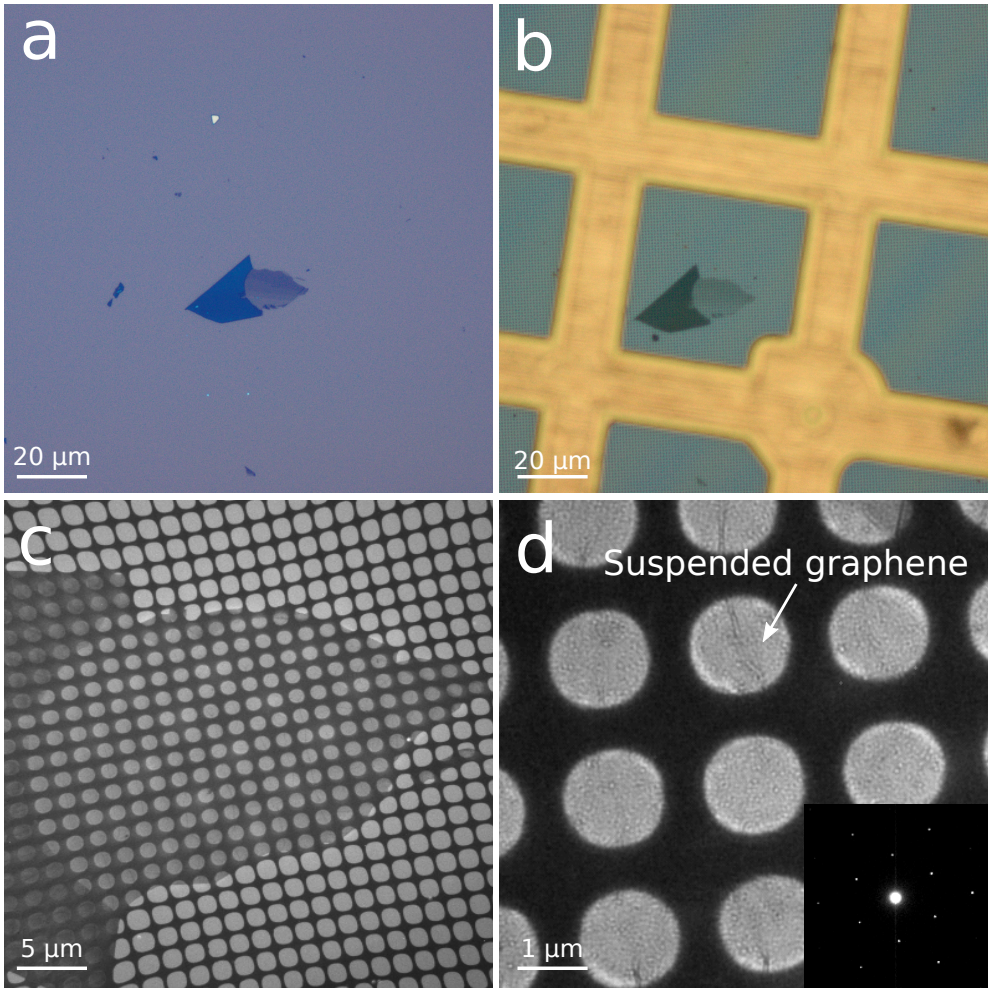

Figure 2.7: Exfoliated graphene transfer. (a) Optical micrograph of exfoliated graphene flakes. (b) A TEM grid placed directly on top of the flake. (c) Low-magnification TEM overview image of the suspended flakes on the Quantifoil® grids after transfer. (d) Magnified view of the same flake. Inset in (d) shows a diffraction pattern of the transferred flake.

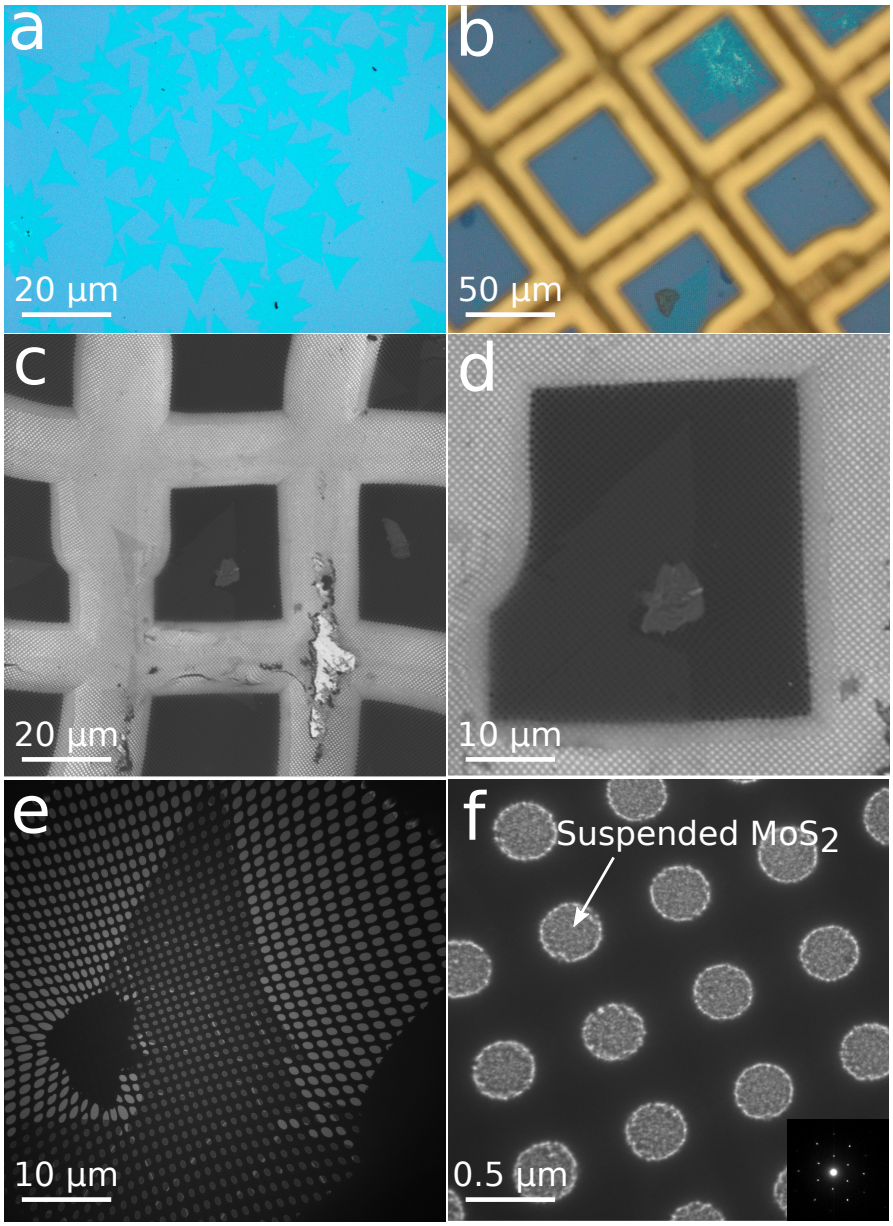

Figure 2.8: MoS_2 transfer. (a) Optical micrograph of CVD-grown MoS_2 flakes. (b) TEM grid placed directly on the flakes. (c) Low-magnification scanning electron microscope image shows the suspended flakes on the TEM grid after transfer. (d) Zoomed-in view of the same region. (e) Low-magnification TEM image after successful transfer. (f) Magnified view of same flake. Inset in (f) shows the diffraction pattern of the transferred flake.

2.4 *Ex-situ* and *pre-situ* annealing

Hydrocarbon impurities and contamination often seriously diminish the properties of graphene. Additionally, clean samples are an essential requirement for most experiments. However, contamination is especially problematic for the low-dimensional materials presented in this thesis. Common sources for hydrocarbon contamination are polymeric residues from sample preparation, the transfer process, and adsorbates from air. Their chemical nature is still not precisely known, but most of the literature points to (-CH_2-) and (-CH_3-) groups [75]; carboxyl, methoxy, and sp^3-hybridized carbon [76]; and CO functional groups [77]. Although various methods have been reported to remove the contaminants, annealing the samples in air or in vacuum is the most used method. These can be divided into *ex-situ*, *in-situ* and "*pre-situ*"methods. In *ex-situ* annealing, samples are treated in air or vacuum. After the treatment, the samples are transferred through the ambient to be characterized using another setup. In *in-situ* and "*pre-situ*" methods, annealing and characterization is done in a same vacuum system without changing the sample environment, with "*pre-situ*" denoting a separate vacuum chamber connected to the instrument. For this thesis, two *ex-situ* and two *pre-situ* annealing techniques were used to clean graphene samples.

Ex-situ annealing in air was done by heating the samples on a hot plate between 300–500 °C for times ranging from 15 min to 1 h. Vacuum annealing was carried out in MANTIS HEX deposition system from Korvus Technology, with resistive heating achieved by passing a current through a filament in vacuum. The amount of heating depends on the current through the filament. Graphene samples were placed in a ceramic boat inside the vacuum chamber and a thermocouple attached to the boat to measure the temperature. The base pressure of the chamber was $\sim 10^{-6}$ mbar. After the treatment, samples can be taken out for characterization by venting the vacuum chamber into N_2 atmosphere.

To implement *pre-situ* annealing, modification of the characterization setup is required. In our case, a custom-built vacuum system is connected to the Nion UltraSTEM100, which allows us to implement various methods for sample treatment without exposing it to air. For *pre-situ* annealing, we developed laser cleaning and radiative heating via a tungsten wire in these vacuum chambers. For laser annealing, a high power laser diode (tunable up to 6 W, 445 nm wavelength) from Lasertack GmbH was aimed through a viewport at the sample held in the parked pneumatic transfer arm from an angle of about 45°. The vacuum level was about $\sim 10^{-8}$ Torr and the laser spot diameter was about ~ 1 mm^2 in size. Distance between the laser source and the sample was approximately 40 cm. Figure 2.9a & b show the sample cleaning laser in operation. Recently, laser re-alignment was done so that it hits the sample sitting in the microscope objective, allowing sample treatment *In-situ*. Laser

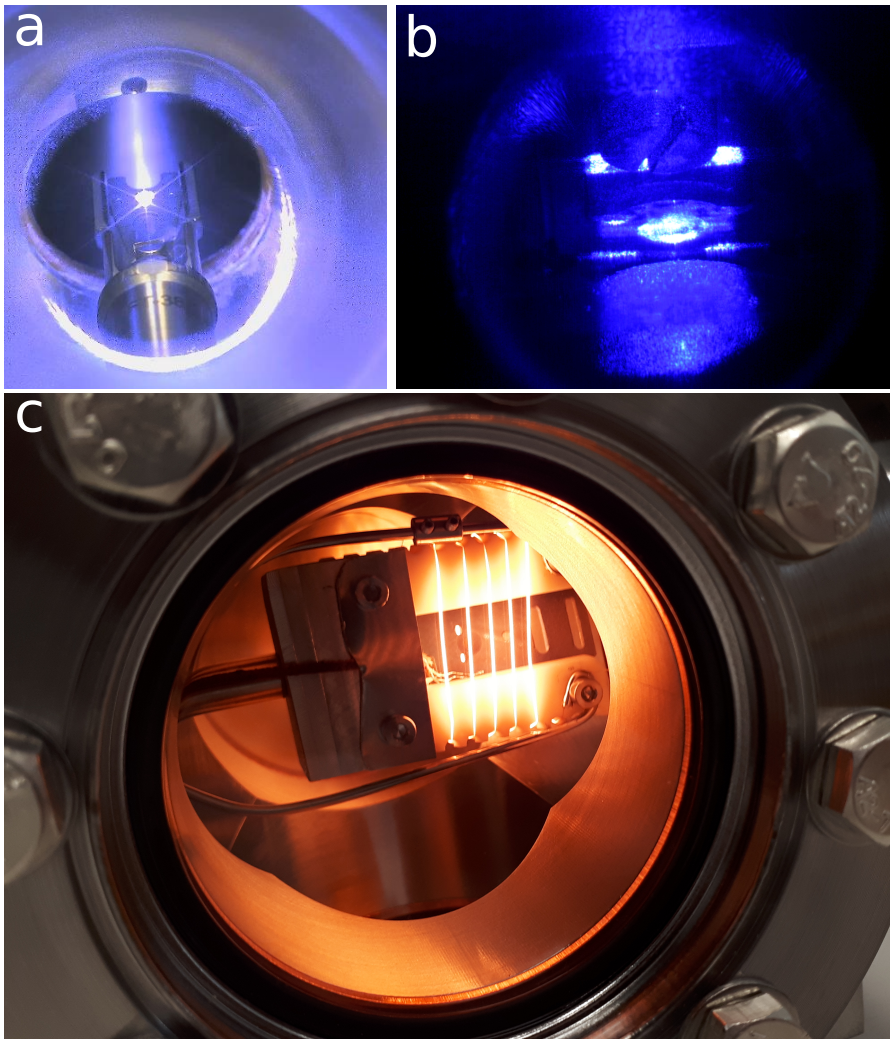

Figure 2.9: *Pre-situ* cleaning of graphene via laser irradiation in (a-b), and resistive heating with a glowing tungsten wire (c). The bright spot in the center of the image in panel (a-b) is the location of the sample in the holder, and the reflections of the laser light from the sample holder are also visible on the camera.

pulses can be used iteratively with increasing power until cleaning is observed for all types of samples in standard holders. However, due to continuous heating, thermal drift is induced in the sample stage of the microscope. Also, the power must be carefully controlled since at higher power the laser will destroy the sample, as discussed in Section 3.1.2.

The second approach to clean samples in vacuum was by radiative heating with a tungsten wire that can be resistively heated to high temperatures,

mounted in a vacuum chamber attached to the microscope. Figure 2.9c shows a glowing W wire in operation. Distance between the wire and sample was about to 2–3 *mm* and the vacuum level about $\sim 10^{-8}$ Torr. In similar way to laser cleaning, the heating power and treatment time can be varied to get the cleanest samples. The wire starts to glow at about 1000 K. As the wire temperature increases, its color varies through the spectrum up to orange and yellow until fully white. The wire current and corresponding thermal power should be chosen carefully in order to not destroy the sample.

All *ex-situ* samples were characterized using a bench-top low acceleration voltage (5 kV) transmission electron microscope (LVEM5). Selected *ex-situ* and all *pre-situ* cleaned samples were characterized at high resolution using the aberration-corrected Nion UltraSTEM100 operated at 60 kV (with a standard 12 hr pre-baking at 130 °C before inserting into the microscope).

2.5 Defect engineering using charged particles

Defects significantly alter the properties of 2D materials. These effects are not always detrimental and can even be beneficial for specific properties. Thus, defect engineering is one way to modify 2D materials and control their physical, electronic, chemical and optical properties. In order to implement the desired functionalities, many methods of particle irradiation (bombardment with electron or ion beams) have been employed [78].

While the response of 2D materials to energetic charged particles can be characterized using atomic resolution imaging or spectroscopic methods, one needs to be careful because structural transformations can occur in the materials when they are analyzed. For example, highly energetic electrons are used in TEM, although modern aberration-corrected TEMs are typically operated at low primary beam energies between 30–100 kV. In order to understand structural modification on the atomic scale by individual electron impacts, it is necessary to precisely understand the radiation damage mechanism, which still remains a challenge.

When a highly energetic particle such as an electron or ion hits the sample, energy or momentum can be transferred either to the electronic system or to the nuclei, leading to radiation damage. Thus, radiation damage limits the ability of microscopy to resolve samples at high resolution. The two most fundamental radiation damage mechanism are knock-on displacement and bond breaking via ionization (radiolysis), depending on the charge state and kinetic energy of the projectile and the electronic properties of the sample. Several other mechanism such as chemical etching, specimen heating and electrostatic charging can also cause damage in the materials. However, such phenomena are not relevant to the studies presented here.

2.5.1 Defect engineering using ions

The slowing down of an ion passing through a materials can be described by electronic (inelastic) and nuclear (elastic) stopping [79]. The electronic stopping is due to charge exchange between the moving ion and electrons in the target and ionization or electronic excitation of the target. Energy deposition S can be defined as energy dE per unit length dx,

$$S_n = -\frac{dE_n}{dx},\ S_e = -\frac{dE_e}{dx}, \tag{2.1}$$

where n denotes nuclear and e electronic stopping. Generally, nuclear stopping dominates for slow and heavy ions while electronic stopping is dominant for ions with high kinetic energies [78, 80]. However, in the case of highly charged ions (HCIs), the kinetic energy is in the nuclear stopping regime whereas due to their high potential energy (sum of the ionization energies of the missing electrons), electronic excitation of the target occurs at the same time [78].

The interaction between the ion and a target atom can be described by the screened Coulomb potential

$$V(r) = \frac{1}{4\pi\varepsilon_0}\frac{Z_1 Z_2 e^2}{r} \cdot \phi\left(r\right), \tag{2.2}$$

where Z is atomic number of the moving ion (Z_1) and the target atom (Z_2), e the elementary charge, $\phi\left(r\right)$ a screening function and ε_0 the dielectric constant. When the target atoms acquire enough kinetic energy from the ions they are displaced from their original lattice sites. The maximum elastic energy transfer can be calculated from momentum conservation as

$$E_{\max} = \frac{4m_1 m_2}{(m_1+m_2)^2}\frac{m_1 v_1^2}{2}, \tag{2.3}$$

where v_1 and m_1 are the velocity and mass of the projectile, and m_2 of the atom. The cross section for this energy transfer [78, 81] can be calculated as

$$\sigma(E_{\max}) = \frac{2\pi(Z_1 Z_2 e^2)^2}{m_2 v_1^2}\frac{1}{E_{\max}^2}. \tag{2.4}$$

2.5.1.1 Low-energy ion implantation

Ion implantation is an established and efficient post-synthesis technique to modify the structure of materials. It does not require any additional chemistry that may introduce residual contaminants, and offers great flexibility such as different ion species, a range of implantation energies, and control over the dopant concentration through the ion fluence. It is widely used by the

modern semiconductor industry to introduce controlled concentrations of p and n-type dopants at precise depths below crystal surfaces. Although it is a mature industrial technology for bulk materials, in recent years the application of this method has been extended to 2D materials in research laboratories.

As the ions impinge on materials, they undergo a series of collisions with the host atoms losing energy due to Coulomb interactions with nuclei (elastic collisions) and electrons (inelastic collisions) in the target. In nuclear stopping, energy lost by the incoming ion is transferred to the target atom that can be recoiled away from its lattice site creating a defect. In contrast, energy loss by incident ions in electronic stopping generates excitations of the electrons in the target. Electronic stopping is proportional to the ion velocity and the momentum transferred from electrons to the ion is too small to cause deviation in direction, but nuclear stopping causes a significant deviation in the path of ions. The sum of nuclear and electronic stopping power corresponds to the total energy loss per distance traveled.

The interaction of ions with the material depends on implantation parameters such as incident ion energy, mass, sample temperature and dose rate. If energy transferred from the ion to a target atom is comparable to the displacement threshold energies (T_d) of the material, the ion can replace lattice atoms or create other defects within a few atomic layers. However, at higher energies the ion will penetrate deeper and can sputter atoms. Ion fluence (dose) corresponds to the total number of ions incident per unit area of the target material and is another crucial parameter to control the concentration of dopants. Heating during implantation might be necessary to prevent hydrocarbon contamination on the surface of the material. At the same time it can also reduce lattice damage via defect annealing.

The response of 2D materials to ion irradiation can be different from bulk materials since relatively little energy is required to remove one or more atoms from the lattice, yet for successful implantation the ions must be retained within the atomically thin structure [82]. Therefore, transferable kinetic energies from the incident ions to carbon atoms during collisions should be on the order of T_d and the remaining kinetic energy of the ion after collision should be low enough to allow it to stay in the lattice.

Boron and nitrogen are the most obvious elements to implant into graphene as their atomic radii are similar to carbon and they have one electron less and more, respectively. After the theoretical prediction of direct doping of N and B atoms into graphene via ion implantation, the first direct observation was made via atomic resolution imaging in combination with spectroscopy [40, 82]. Although silicon is the most common impurity found in the graphene lattice, it has not been implanted so far even after theoretical predictions [83]. Very recently, efforts have been done to implant graphene with heavier elements such as phosphorous [46]. Apart from graphene, low-energy ion implantation has already been applied for example in MoS_2 and hBN [84].

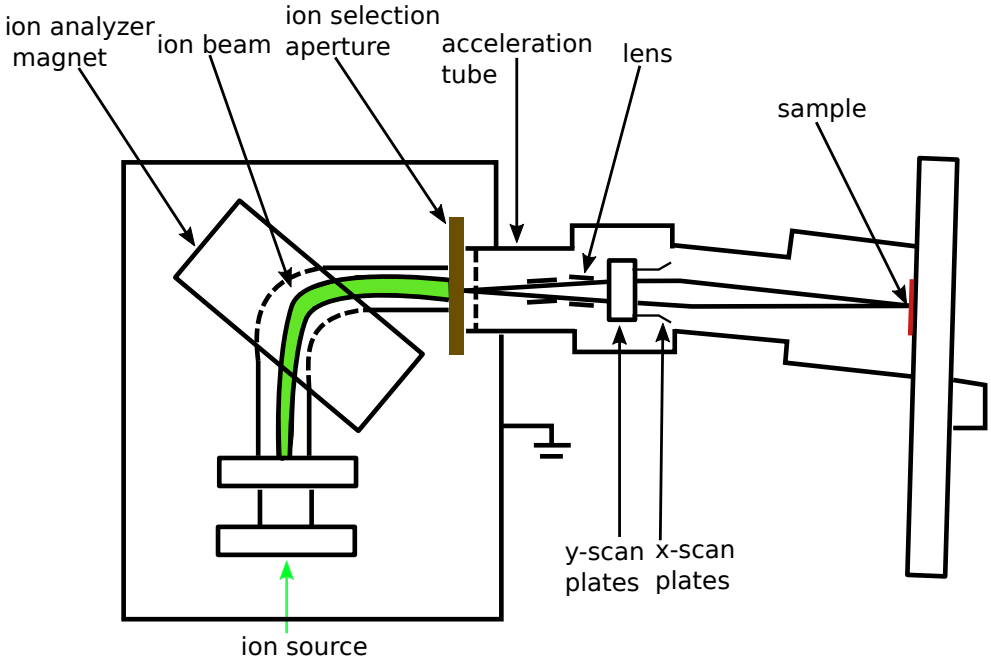

Figure 2.10: Schematic illustration of an ion implanter.

For ion implantation, ions are created by volatilizing the source (solid or gas) and extracted by a high electric field. A magnetic field mass analyzer selects and separates the appropriate ion by its mass-to-charge ratio. Ions are electrostatically accelerated to desired kinetic energies and deflected to eliminate neutral ions, and finally decelerated toward the target, with a bias voltage setting the ion energies. Figure 2.10 shows a simplified schematic illustration of a typical ion implanter set-up.

In the work presented here, we used a mass-selected, twofold electrostatic raster-scanned ion implantation system (Danfysik A/S, Denmark, Model 1050), providing ion energies down to 100 eV at the Helmholtz Zentrum Dresden Rossendorf Ion Beam Center in Germany. In order to substitute carbon atoms in graphene, we implanted a variety of ions (Ge, P, Al, B) using very low ion energies in the range of 15–60 eV to avoid irradiation-induced defects in the lattice. To reduce energies down to 15 eV, a bias voltage was set to the sample holder by an adjustable anode potential. The samples were irradiated in 9×10^{-7} mbar vacuum at room temperature with a fluence of 1×10^{14} cm^{-2} (estimated with multiple Faraday cups).

Typically, ion-irradiated graphene samples were afterwards almost fully covered with amorphous carbon contamination, likely due to ion-beam induced deposition of mobile hydrocarbons that are present on the sample surface and in the vacuum system, despite using a sample heating laser during irradiation. Figure 2.11 shows a direct comparison of the sample before and after ion

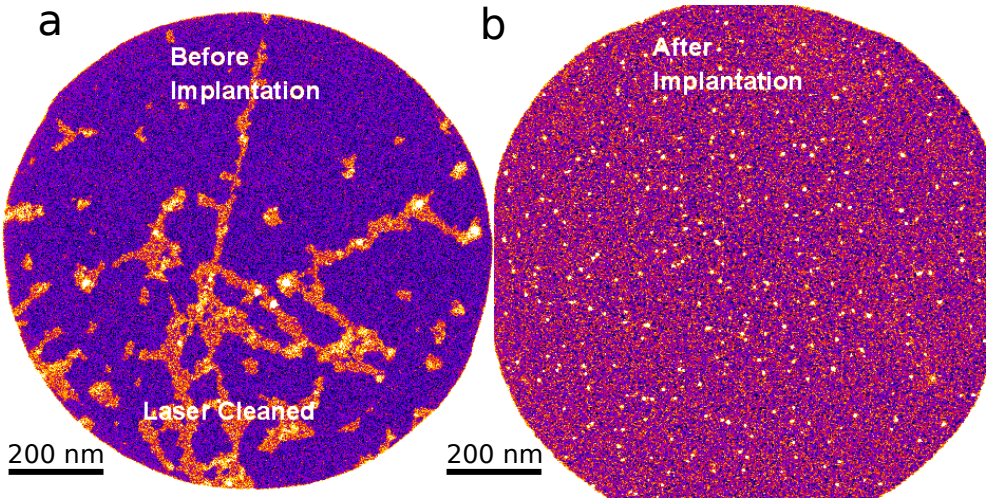

Figure 2.11: Sample comparison before and after implantation. (a) Except for chain-like contamination, the laser-cleaned sample appears clean. (b) Uniform layers of contamination covering the sample after implantation. The images show two different holes.

implantation. The initially clean sample has become severely contaminated during irradiation. Unfortunately, in the case of Al and B dopants, despite exhaustive searching, we could not find a single impurity atom in the lattice.

2.5.1.2 Highly charged ion irradiation

Highly charged ion (HCI) irradiation is a unique method to modify the atomic structure of materials. HCIs are produced by stripping electrons from neutral atoms by energetic collisions. In the case of HCIs, due to ionization they store a very high potential energy, which is a sum of all binding energies of the missing electrons. Thus the potential energy is dependent on the charge state, i.e., higher the charge state, the greater the potential energy. Upon each ion impact on a target, ions release their stored energy leading to electronic excitations. Ion-induced electron emission has been studied for structural modification in solid bulk materials [85]. HCI irradiation of 2D materials is a relatively new technique and its mechanism is not very well understood [78].

As an incoming HCI impacts on a solid surface, it attracts electrons from the surface leading to its neutralization and the deposition of the potential energy in a strongly localized volume of the surface in a very short (femtosecond) time-scale. Due to electronic exchange interactions, release and deposition of the potential energy of ions is different from that of their kinetic energy, but may also lead to a modification of the structure by atom removal [86]. A helium ion beam [87] or an electron beam [31] have been used to drill pores in MoS_2, but these methods are not suitable for mass-production.

Theoretical studies point to mainly mono- and divacancies in MoS_2 from single ion impacts at few keV kinetic energies [88]. The first HCI irradiation experiments were performed for MoS_2 samples supported on KBr substrate using Xe ions [89]. Atomic force microscopy (AFM) images showed defects in the sample as pits or hillocks, induced by single ion impacts. The same group further irradiated mono- and few-layer graphene on SiO_2 substrates using highly charged Xe ions at different potential energies [90]. No defects were observed in conventional contact-mode AFM images. However, round-shaped pores were detected in friction-force mode. Freestanding ultra-thin carbon membranes were also irradiated via HCIs [91] and TEM images showed the formation of pores. Further analysis showed that the pore diameter can be increased with increase in potential energy, but pore formation at higher charge states also depends on the kinetic energy of the impacting ions.

Surprisingly, atomic resolution STEM images showed no pores or defects in free-standing monolayer graphene even after irradiating it with Xe^{40+} ions [92]. Since graphene has very high electron mobility, it may be able to provide tens of electrons to neutralize the charge of a slow HCI within a few femtoseconds. Defects in graphene can also be healed quickly [93] or covered with hydrocarbon contamination. Recent experiments on hexagonal boron nitride supported on different substrates showed no defects in surface topography after irradiation with Xe^{40+} ions, while in the friction-force mode defects appear, similar to supported graphene experiments [90, 94].

HCIs can be produced by powerful ion sources for almost all elements and charge states. Currently available sources are electron cyclotron resonance ion sources, electron beam ion traps (EBITs) and electron beam ion sources (EBIS). For this thesis, an EBIT/EBIS was used to produce highly charged xenon (Xe) ions at the University of Duisberg-Essen, Germany. Figure 2.12 show a schematic illustration of the set-up. First, an electron beam is generated by the emitting source (hot cathode) and focused by means of a strong magnetic field. HCIs are produced by successive electron impact ionizations (removal of bound electrons by collisions of high energy electrons with the atom) inside the electron beam and are trapped radially due to the negative space charge of the electron beam. Ions are confined axially in the beam direction by applying electrostatic potentials to the drift tubes. Thereby a strong electric field creates an electrostatic ion trap due to the greater potentials on the outer drift tubes. Thus, by changing the axial trap potential, the ionization time can be controlled. After leaving the drift tube and strong magnetic field, the beam broadens again and then is finally dumped at the electron collector where electrons are separated from the extracted ions.

For this thesis, free-standing MoS_2 and WS_2 samples were irradiated with highly charged Xe ions of different charge states (q = 20–40). Round-shaped pores in MoS_2 and triangular-shaped sharp-edged pores were directly observed in atomically resolved STEM images.

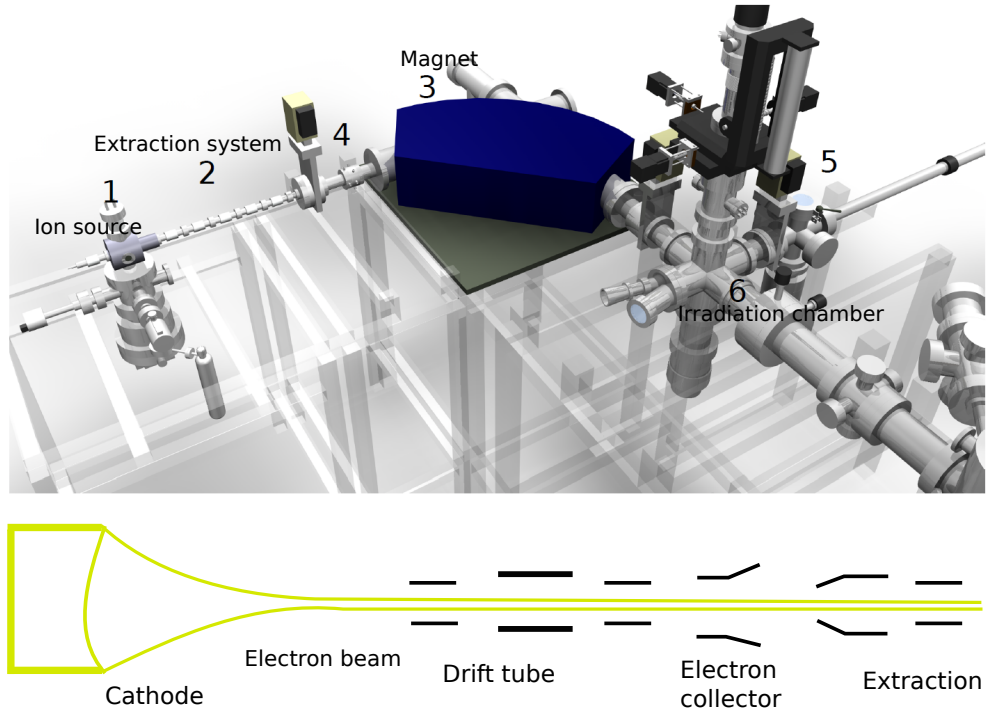

Figure 2.12: Schematic illustration of an electron beam ion source set-up for the formation of highly charged ions. Instrument image reprinted with permission from [95]. Copyright © (2008) Elsevier B.V.

2.5.2 Defect engineering using electrons

Electronic excitations can be caused by inelastic (electron-electron) scattering involving an interaction with the electron cloud of an atom [96]. When conduction band electrons are excited above the Fermi level, this leaves a hole in the valence band. In metallic systems, these holes are filled rapidly (in femtoseconds) due to high density of conduction electrons, which reduces the effect of ionization damage [97]. In contrast, ionization damage caused by inelastic scattering dominates in insulators and semiconductors, where the lifetime of the excited electrons is long enough that the structure can be modified [98], hBN [39] and MoS_2 [99]. Ionization damage is difficult to avoid, but efforts such as cooling with liquid nitrogen or helium, or protecting the samples with well-conducting (e.g. graphene) layers have been used to mitigate damage in 2D materials [100].

Knock-on damage is dominant in the case of metal samples [101] including CNTs [102] or graphene [103], and is caused by elastic (electron-nucleus) scattering of energetic electrons or ions from the nuclei of target atoms. This can result in an atomic displacement within a sample due to momentum and energy transfer. Knock-on damage can be avoided by lowering the primary

beam energy, unlike ionization damage which is stronger at lower energies. With the development of aberration correction, modern microscopes can be operated at very low acceleration voltages even down to 30 kV.

The minimum energy required to displace an atom from its lattice position is called the displacement threshold energy and denoted by T_d. Coulomb scattering of a relativistic fast electron from a nucleus was described by Mott [104] and further approximated by McKinley and Feshbach [105].

The maximum energy transferred from an electron with energy E_e to a target element with atomic mass M at rest (out-of-plane velocity v_z=0, where z is the direction parallel to the electron beam) can be calculated as

$$E_{max}\left(v_z = 0, E_e\right) = 2E_e(E_e + 2m_e c^2)/Mc^2, \tag{2.5}$$

where m_e is the mass of electron and c is the speed of light. For a realistic estimation of the cross section, out-of-plane lattice vibrations of the atoms should be considered. Taking the velocity of the target atoms into account, the maximum transferred kinetic energy is higher than it is at rest. With the approximation

$$E_e + E_n - E \approx E_e, \tag{2.6}$$

where E_n is the energy of nucleus before collision and E after collision, the maximum transferred energy from an electron to an atom with velocity v_z becomes

$$E_{max}(v_z, E_e) = \left(2\sqrt{E_e(E_e + 2mc^2)} + Mv_z c\right)^2 / Mc^2. \tag{2.7}$$

Calculating cross sections using this equation and comparing with experimental STEM measurements for graphene at different primary beam energies between 80–100 kV shows a good agreement [106, 107]. Cross sections σ can be estimated using

$$\sigma(T, E_e) = \int_{(E_{max}(v_z, E_e) > T_d)} P(v_z, T)\sigma\left(E_{max}\left(v_z, E_e\right)\right) dv, \tag{2.8}$$

where P(v_z,T) is the velocity distribution of the atoms parallel to the electron beam. T_d for graphene is 21.14 eV [107].

2.5.2.1 Electron-beam manipulation

Since almost 30 years, scanning probe microscopy (SPM) has been used to manipulate individual atoms on surfaces and to fabricate nanostructures at the atomic scale [108, 109]. Although the use of STM for atom manipulation

continues to provide technological advancements such as atomic memory arrays [110], its application is limited to surface atoms. In order to move an atom from its location, the energy acquired from the tool E_{tool} ($\sim$1 eV for STM) should be higher than the energy barrier $E_{barrier}$ for moving an atom,

$$k_B T << E_{barrier} < E_{tool}, \tag{2.9}$$

but also higher than the thermal energy $k_B T$, where k_B is the Boltzmann constant and T the absolute temperature. To stabilize and manipulate surface adatoms with STM tips, ultra-low temperature is required. By contrast, covalently bound impurity atoms in the lattice of low-dimensional materials are stable at room temperature due to very high migration barriers [111]. However, the focused Å-sized electron probe of aberration-corrected scanning transmission electron microscopy [62] can provide enough energy to overcome the barrier and induce dynamics of individual atoms in the lattice.

Due to momentum conservation, the mass of heavier impurity atoms plays an important role. As an example, a 60 kV electron beam can transfer much less energy to a nucleus of heavier impurities such as Ge than their displacement threshold energy (11.75 eV [112]). It also cannot provide enough energy to displace C atoms from pristine graphene. However, carbon atoms next to heteroatoms are less strongly bound in the lattice and can be affected [113]. Figure 2.13a shows a STEM/MAADF image of a three-coordinated Si atom (Si-C_3), which is bonded with three C atoms in a buckled out-of-plane configuration either above or below the graphene plane with respect to the beam direction [44, 114]. At low primary electron energies, the beam cannot eject C atoms from the lattice, but it can impart enough of a *kick* to the C to displace it from its lattice position. However, due to a attractive force between Si and C atoms, the C atom is *pulled* back. In the meantime, the Si atom relaxes into the vacancy left by the C atom, which ends up on the opposite site [44]. Figure 2.13b & c shows the same area of graphene where the Si has jumped by one lattice site. Following this, the atoms can be manipulated in a controlled way by iteratively placing a focused electron probe on the top of the desired C atom next to the dopant. For this thesis, the manipulation of Si and P atoms in graphene and Si atoms in SWCNTs have been demonstrated.

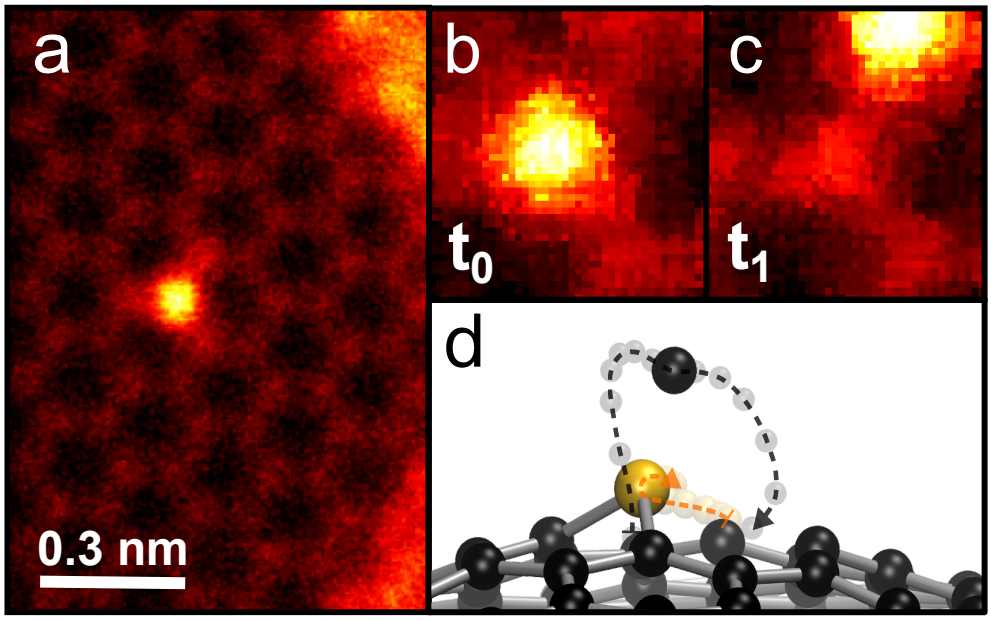

Figure 2.13: STEM/MAADF images show a three-coordinated Si (bright) atom in graphene (a). A zoomed-in view of the local structure at its initial position at time t_0. (b) The same area, where Si has jumped by one lattice site after time t_1 upon electron beam irradiation at 60 kV primary energy. (d) represent a structural model with the trajectories of the ejected C atom (black) and the Si atom (yellow) overlaid by semi-transparent balls and dashed lines. Image reused with permission from Ref. [115] (CC-BY).

Chapter 3

Results

This Chapter is dedicated to the results that were achieved during the course of this thesis, and it is divided into five parts. Section 3.1 is devoted to sample cleaning, especially using *pre-situ* annealing. Section 3.2 presents nanopores in single-layer transition metal dichalcogenides, induced either by highly charged ion irradiation or intrinsically present along its grain boundaries. Section 3.3 is dedicated to low-energy ion irradiation, particularly germanium implantation into graphene. Section 3.4 focuses on the electron-beam driven dynamics of different heteroatoms in graphene and single-walled carbon nanotubes. Finally, Section 3.5 presents the electron-beam manipulation of impurities, primarily silicon, in graphene and single-walled carbon nanotubes.

3.1 Sample cleaning

This Section is dedicated to the pre-situ cleaning method developed to clean graphene in vacuum during the course of my PhD. The content is based on entry 1 and the mechanical exfoliated graphene results on entry 4 of the list of publications.

Here, we analyze and compare the effectiveness of heat treatments in air and in vacuum to clean graphene. We investigate its relative cleanliness after *ex-situ* annealing in air on a hot plate or in a vacuum chamber. We further demonstrate a new, effective and reliable cleaning approach using radiative heating via a tungsten wire or a high power laser in vacuum, as explained in Section 2.4 in the previous Chapter. Samples were characterized using low acceleration voltage TEM and atomic resolution aberration-corrected STEM.

3.1.1 Untreated samples

Figure 3.1 shows STEM/MAADF images of an untreated commercially available CVD-grown single-layer graphene sample, transferred onto Quantifoil®

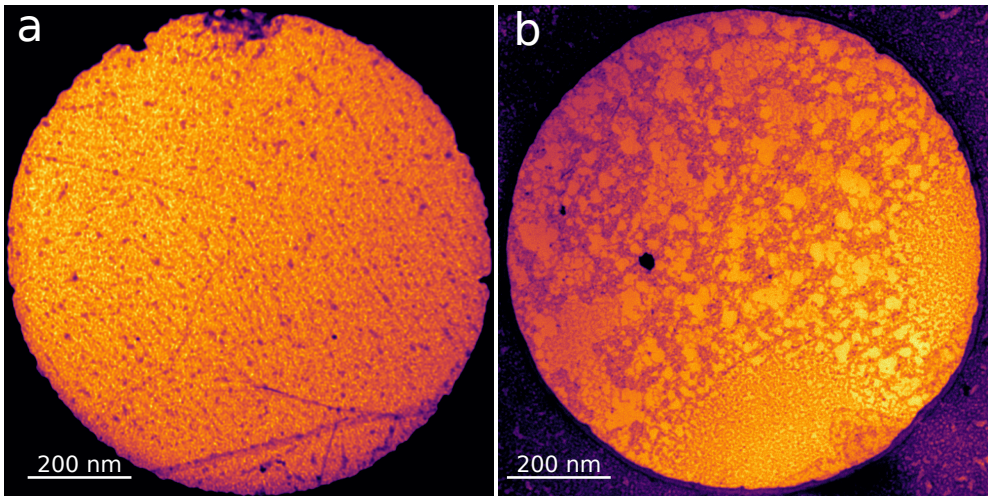

Figure 3.1: STEM/MAADF images of a typical graphene sample without treatment.

TEM grids. In dark-field STEM images, darker contrast is an indication of the amount of contamination overlying the atomically thin graphene sheets, as can be seen in Figure 3.1: the sample looks fully covered with the dark patches of contamination.

3.1.2 *Ex-situ* cleaning

3.1.2.1 Air annealing

Air annealing was done by heating the samples on a hot plate. The experimental details are described in Section 2.4. Figure 3.2 shows TEM images of suspended monolayer graphene after annealing in air at temperatures between 400–500°C (treatment at lower temperatures does not yield larger clean areas, even if contamination layers are thinner). After air treatment at 400°C for 1 h, structural damage of graphene starts to emerge, but residues have not been much affected as shown in Figure 3.2a & b. By increasing the temperature to 450°C for 30 min, tearing of graphene sheets becomes frequent and the concentration of impurities is reduced as illustrated in Figure 3.2c & d. However, significant contamination still remains. At 500°C for 15 min, crack formation is evident almost everywhere on the sample, as shown in Figure 3.2e & f. At the same time, some regions of the contamination appear to be thicker after the treatment. Thus, air annealing at high temperatures does help in removing residues, but severe damage occurs [116] in the suspended graphene regions, presumably assisted by the etching of grain boundaries.

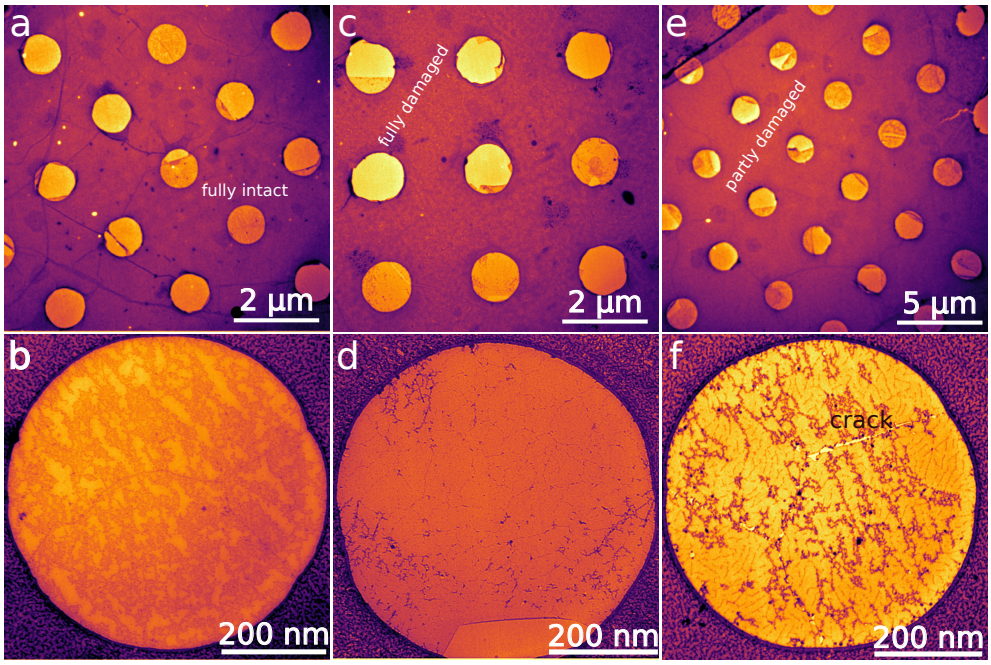

Figure 3.2: TEM images of CVD-grown monolayer graphene after heat treatment in air. (a) Overview and (b) magnified view after annealing at 400°C for 1 h. (c) Overview and (d) magnified view after 450°C for 30 min. (e) Overview and (f) magnified view after 500°C for 15 min.

3.1.2.2 Vacuum annealing

In vacuum, graphene can withstand significantly higher temperatures [116, 117], but cleaning is also expected to be slower without a reactive atmosphere. Samples were annealed in a vacuum chamber (see Section 2.4) and characterized using TEM and further STEM. Figure 3.3 shows TEM and STEM/MAADF images of graphene annealed between 600–750°C (heated at a rate of 10°C/min and cooled to room temperature in N_2). Figure 3.3a shows TEM images of a sample that was heated to 600°C. However, contaminants cover the surface, with small clean spots no larger than a few tens of nm^2. After thermal treatment at 650°C for 15 min, surface contamination was reduced (Figure 3.3b). However, long treatments at high temperature start to cause crack formation even in vacuum. We further increased the annealing temperature to 750°C but reduced the time to only 3 min, and observed that many contaminants had been removed (Figure 3.3c). We also found apparently almost fully clean areas (Figure 3.3c), apart from some remaining chains of thicker impurities including heavier particles (probably due to greater binding of impurities at wrinkles, local strain variation, or grain boundaries). However, even this short treatment resulted in severe tearing of the suspended

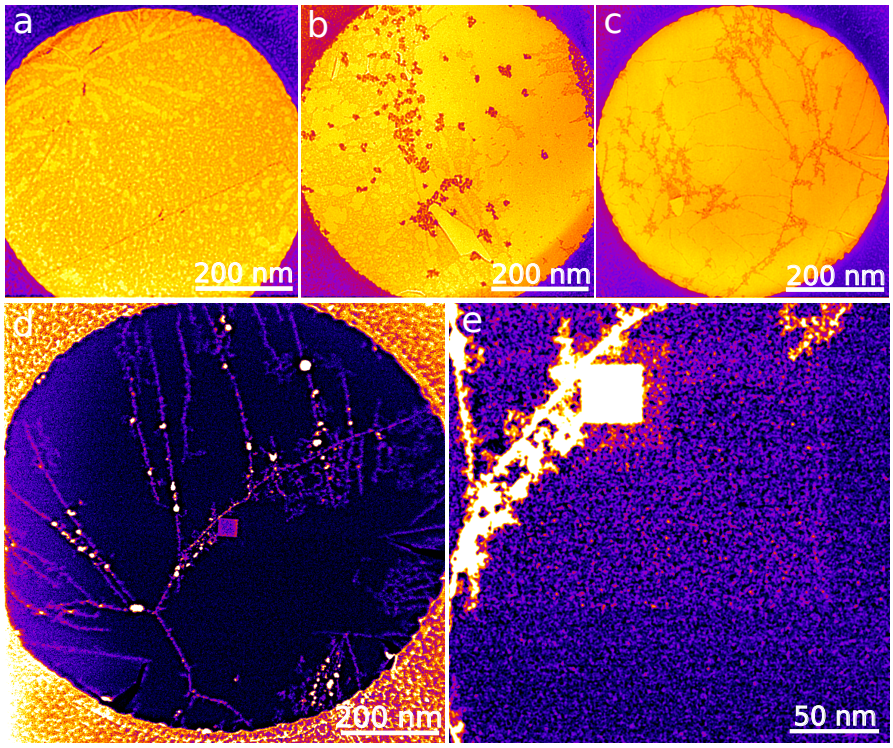

Figure 3.3: TEM (a–c) and STEM/MAADF (d–e) images of CVD-grown monolayer graphene after vacuum annealing at (a) 600°C for 30 min, (b) 650°C for 15 min, (c) 750°C for 3 min. After annealing at 750°C, this sample was transferred via ambient to the Nion UltraSTEM100. (d) Low-magnification STEM image and (e) magnified view of a clean-looking area, revealing that a layer of contamination still covers the surface (noisy contrast), and more rapidly accumulates under the beam (bright squares).

graphene. While chemical etching should be suppressed in vacuum, the mismatch in the coefficients of thermal expansion of graphene [118] and the gold substrate [119] causes a mechanical stress of 1.7 % (as the support expands by 1.46 % and graphene contracts by -0.2 %) at this temperature.

To verify the cleaning, we imaged the 750°C sample at higher resolution. The STEM/MAADF image in Figure 3.3d includes both large clean-looking areas and chain-like impurity patterns. Since ADF contrast is directly proportional not only to the number of atoms in the beam path but also their atomic number [35], the bright spots possibly contain heavier elements such as gold from the support grid that have become mobile at high temperatures. At higher magnifications, we observed that a thin layer of contamination is still covering the regions that appear clean at lower resolution. The square bright contrast in Figure 3.3e was caused by mobile contamination pinned onto the

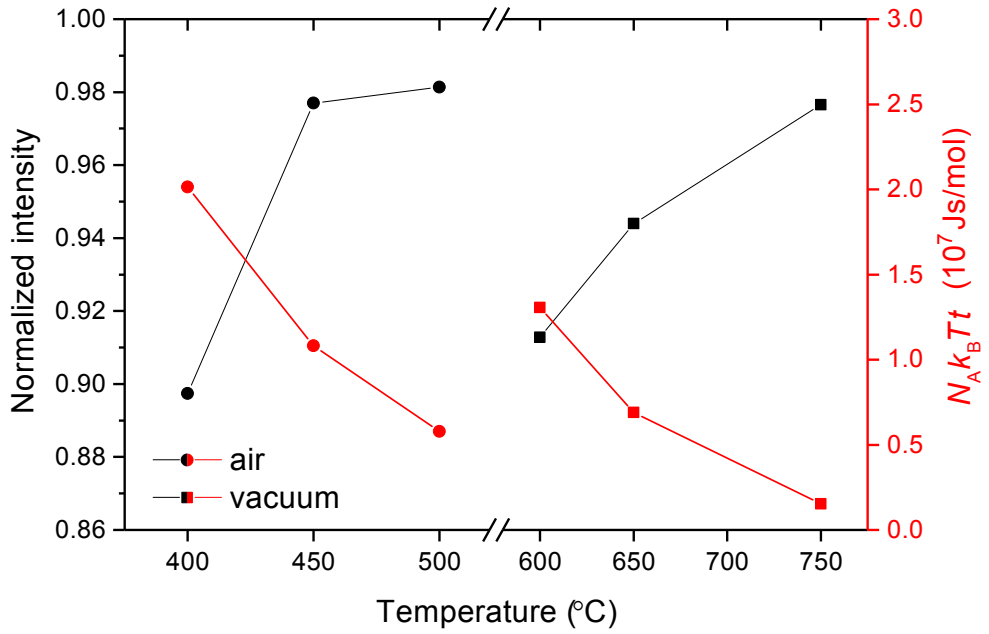

Figure 3.4: Cleaning effect of heat treatments in air and in vacuum. The left axis shows the normalized integrated intensity as a function of annealing temperature (for untreated samples, a typical value was ∼0.61). As the temperature increases, the integrated intensity approaches that of vacuum, corresponding to the removal of contamination. The right axis shows the thermal energy per mole multiplied by the treatment time (Eq. 3.1), suggesting that higher temperature treatments are more effective [121].

surface by the electron beam. These findings may be explained by the highly lipophilic nature of graphene: a thin layer of contamination quickly adsorbs on the surface when graphene is exposed to the ambient [120].

To quantify the effect of cleaning, in Figure 3.4 we plot the integrated intensity which is sum of pixel intensities within a TEM image, measured over several hundred nm^2 of graphene (divided by the intensity measured over vacuum to normalize for differences in beam focusing) for air and vacuum annealing at different temperatures [121]. For both treatments, the integrated intensity approaches a value close to unity with increasing temperature, indicating a decrease of impurity concentration as contaminants on the surface diffuse away. Since we used different treatment times at different temperatures, to compare the treatments we also calculate the time integral of the thermal energy per mole defined as

$$S_{th} = N_A k_B T_t, \tag{3.1}$$

where N_A is the Avogadro constant, k_B the Boltzmann constant, T the temperature in Kelvin, and t the treatment time. The normalized intensity plot in Figure 3.4 shows that relatively shorter treatments are required at higher temperature for the same or even better cleaning effect. This finding corroborates the effectiveness of rapid-thermal annealing.

3.1.3 *Pre-situ* cleaning

To clean graphene using *pre-situ* annealing in a custom-built vacuum chamber attached to the STEM column, we made use of both radiative energy transfer from a resistively heated W wire and from a laser aimed at the sample.

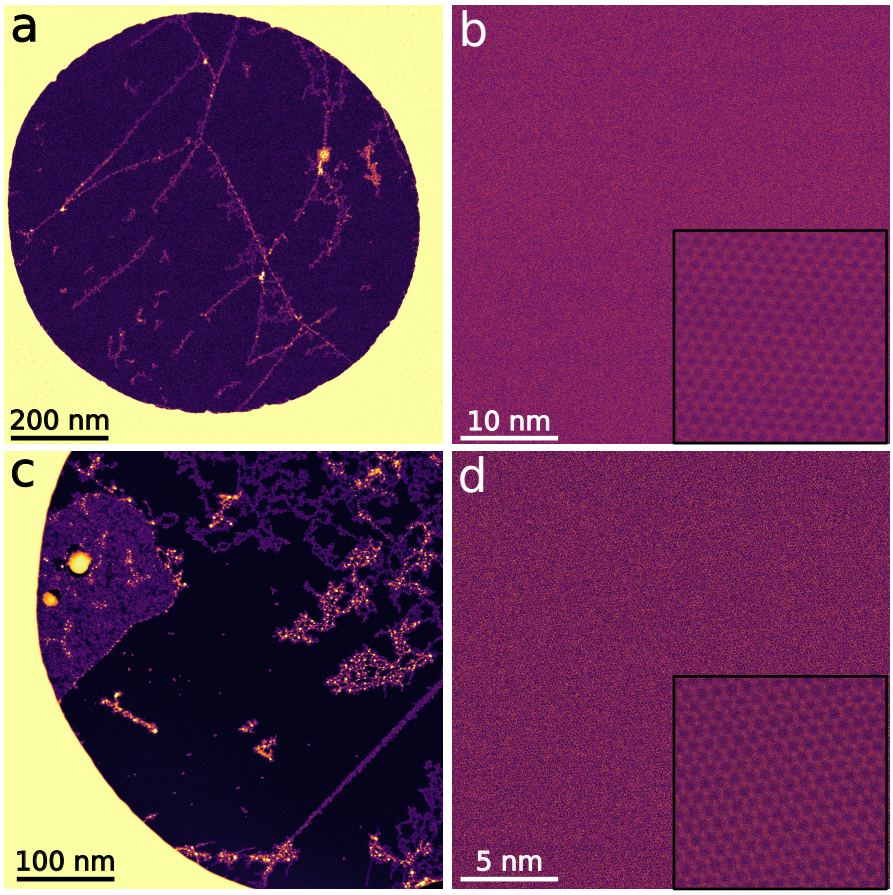

Figure 3.5: STEM/MAADF images show the effect of laser cleaning of CVD-grown monolayer graphene on Quantifoil® grids. (a & c) Overviews of almost fully cleaned holes covered with graphene. (b & d) Magnified views from the clean regions from the respective overview images. Insets in panels (b & d) show the graphene lattice.

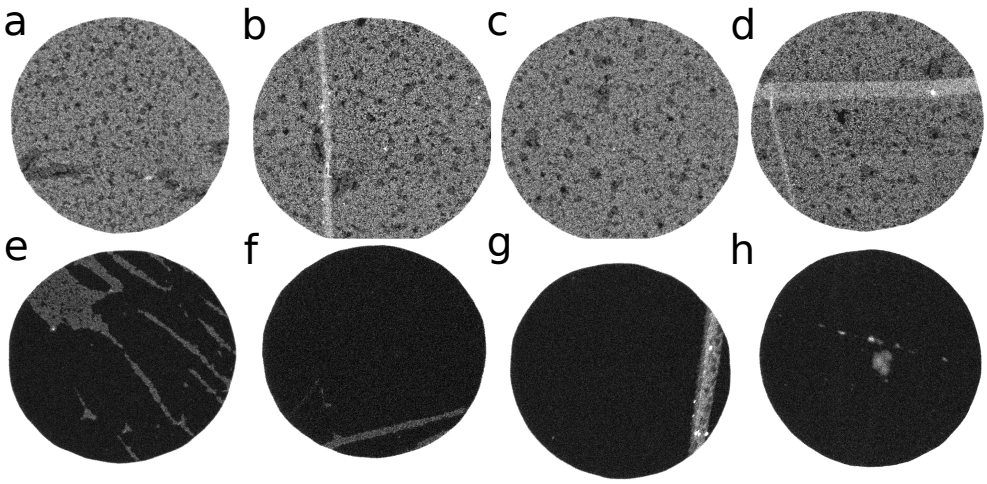

Figure 3.6: STEM/MAADF images showing the effect of laser cleaning on CVD-grown graphene transferred onto SiN grids. Panels (a–d) show overview images without treatment. Graphene holes are fully covered with contamination. After the treatment (iteratively using 55 % power for 1 min) the holes are almost fully cleaned as shown in panels (e–h). The field of view for all panels is 200 nm^2.

The STEM/MAADF overview images in Figure 3.5a & b show two different Quantifoil® holes covered with graphene after laser cleaning. Laser annealing cleaned most of the fixed contaminations from the surface except the thicker ones linked in a chain. Samples were again iteratively treated with increasing laser power until cleaning was observed, leading to good results with 600 mW (10% duty cycle) for 2 min. Several hundred nm^2 clean lattice regions could be achieved as shown in Figure 3.5c & d. Insets show the perfect hexagonal lattice of graphene from the respective regions.

Laser cleaning is thus a very efficient technique to remove the contamination, but irradiating the sample using high laser power (thus at higher temperatures) introduces thermal drift. The evaporation of contamination from the surface and thinning down of the Quantifoil® may also introduce mechanical instability. Silicon nitride (Si_3N_4) microchips with electron-transparent windows provide robust supports for electron microscopy and can withstand very high temperatures. The upper row in Figure 3.6 shows the untreated graphene samples covered completely with contamination. However, laser annealing at 55% power repeatedly for 1 min removed the contamination and retained almost fully intact graphene.

In the case of laser annealing, it is difficult to precisely estimate the heating caused by the laser. Both graphene and the gold support grid have very high thermal conductivity. By assuming that only about 20% (100–200 mW) of the laser power flux is deposited on the sample (due to the geometry, a significant

part missed the sample or was reflected), that the coupling to the sample holder is relatively poor because of the little contact pressure between the grid and the sample holder, and that the system reaches a thermal equilibrium of absorption and emission within a fraction of a second once the laser is switched on, we can roughly estimate a resulting temperature of around 1100–1300 °C from the radiant emittance. At higher power the laser destroyed the sample; since the melting point of the gold support is 1100°C, it appears that our optimum is close to this limit. However, realignment of the laser so that it hits the sample while sitting in the microscope objective, as explained in Section 2.6, may have later changed laser power deposition due to change in the geometry.

In addition to the intrinsic (fixed) contamination as explained earlier, hydrocarbon impurities tend to be mobile and diffuse over the surface of the sample. Such mobile contamination can quickly form a thick layer of carbonaceous film by the cross-linking of adsorbed organic molecules [122] and decomposition by the focused electron beam. STEM/MAADF images in Figure 3.7a & b show the continuously growing mobile contamination as brighter square regions. This process is called as electron-beam induced deposition (EBID). Although EBID of contaminants is unwanted, especially for electron microscopy as it degrades the quality of samples, it can also be used for creating arbitrary patterns with a nanometer-scale resolution in a TEM [123]. Interestingly, while we observed mobile contamination pinning under the beam in these samples, in most cases this occurred only when the field of view contained pre-existing contamination or other defects.

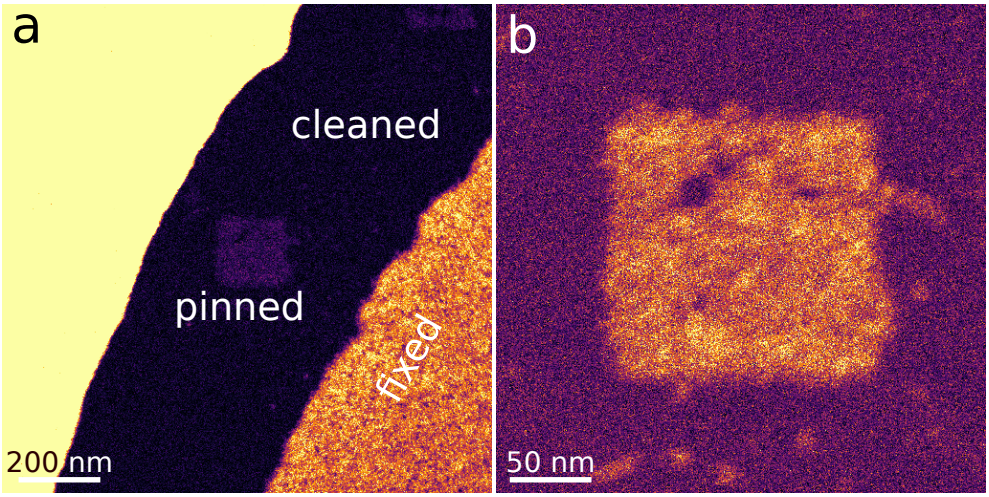

Figure 3.7: STEM/MAADF images show growing mobile contamination deposited under the electron beam. The brighter square in panels (a–b) is due to the pinning down of mobile contamination under the beam.

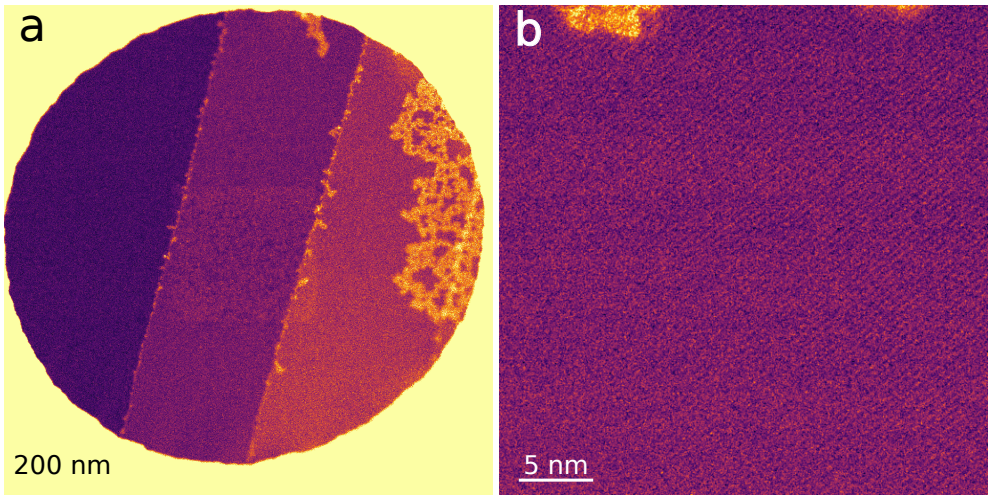

Figure 3.8: Laser-cleaned mechanically exfoliated few-layer graphene. (a) shows the varying graphene layer number by the direct contrast difference.

Figure 3.8 shows the laser annealing effect on mechanically exfoliated few-layer graphene. Irradiating with 10% laser power for 10 s (in a different laser geometry, with the laser spot directly hitting and covering the whole sample) removed most of the contamination from the sample. The effect of contamination on graphene to its core level binding energies was also measured by combining synchrotron-based scanning photoelectron microscopy with STEM and Raman spectroscopy [124].

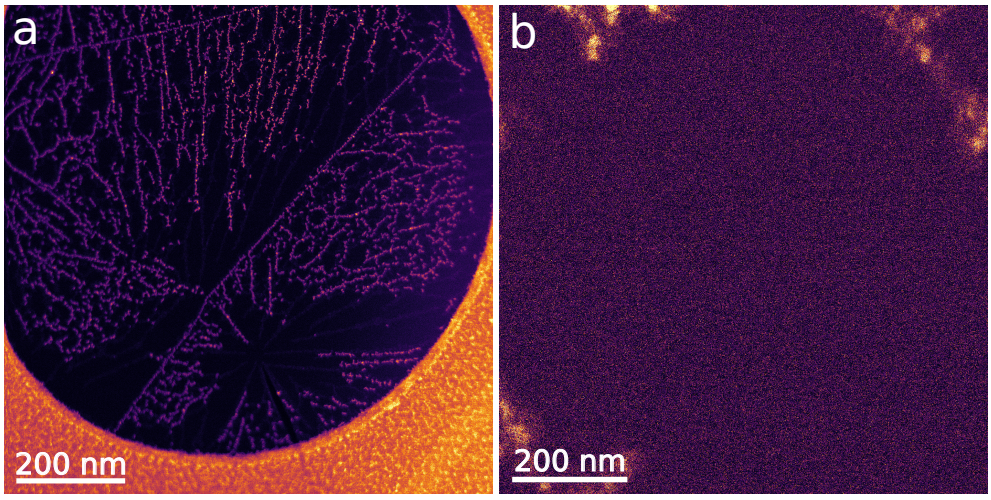

Figure 3.9: CVD-grown monolayer graphene cleaned with W wire radiative heating.

Table 3.1: Quantification of broken or damage Quantifoil® holes after treatment.

Condition		Air (°C)			Vacuum (°C)			*Pre-situ*	
	RT	400	450	500	600	650	750	Laser	W wire
damaged (%)	31	53	44	58	50	38	75	44	55
broken (%)	15	44	37	43	29	13	48	39	39
total	203	59	71	67	70	63	63	46	49

STEM/MAADF images in Figure 3.9 show the cleaned graphene after resistive heating via a tungsten wire mounted in a vacuum chamber attached to the microscope (as explained in Section 2.6). The treatment time was 15 min. The wire power was iteratively increased until cleaning was observed, yielding good results for a current of 7 A, corresponding to a thermal power of 64 W and a wire temperature of 1750 K. Intermediate-resolution images confirm the clean graphene lattice regions.

To estimate the amount of damage after treatments, we counted the number of partially and fully broken suspended graphene areas (some are damaged also in untreated samples), as shown in Table 3.1. These were increased by more than two-fold for all of our cleaning methods, *pre-situ* ones having the smallest increase (presumably due to the best vacuum conditions). Nonetheless, especially in the *pre-situ* samples, it was easy to find clean and fully intact areas. The cleaning effect was similar for both *pre-situ* treatments, although radiative heating causes slightly more structural damage than the laser treatment.

In conclusion, we have compared heat treatments to clean graphene in air and vacuum. We show that air annealing is not a good method: contamination remains on the surface, and severe damage occurs at higher temperatures where the treatment is more effective. Annealing at even higher temperatures in vacuum is more effective in removing surface contaminants, but some seem to re-adsorb upon exposure to an air ambient. This issue can be overcome with *pre-situ* annealing via radiative or laser-induced heating in the same vacuum system as the electron microscope. While some structural damage seems unavoidable, these methods appear to be reliable and controllable for cleaning graphene and potentially other 2D crystals. However, caution must be taken in selecting the treatment time and the laser or thermal power to avoid destroying the sample. With optimal parameters, large areas of atomically clean graphene can be easily obtained.

3.2 Nanopores in transition metal dichalcogenides

3.2.1 MoS_2 and WS_2 nanopores by highly charged ions

This Section is dedicated to highly charged ion irradition of MoS_2 and WS_2. The content is based on entry 5 of the list of publications and unpublished work.

The HCI method offers a unique approach to create pores in a controlled way and to achieve the desired pore density, irrespective of any intrinsic defects present already. We show a fine-tuning of pore diameter in the range of 0.5–5 nm in MoS_2 with the charge state of Xe ions. This corresponds to the energy associated with the charge state of the ion, which gives rise to the efficient removal of atoms from a nanometer-sized area. To study the response of HCIs with similar charge states, we also irradiated another member of the TMD family, i.e. WS_2. Although pore size dependency on the ion parameters and their variation for WS_2 are not conclusive yet, preliminary results show the formation of triangular pores with atomically sharp edges even in thicker (i.e. bi- or trilayer) WS_2.

MoS_2 monolayer samples were grown on SiO_2 by CVD in Dublin [26] as described in the previous Chapter, and transferred from the substrate to TEM

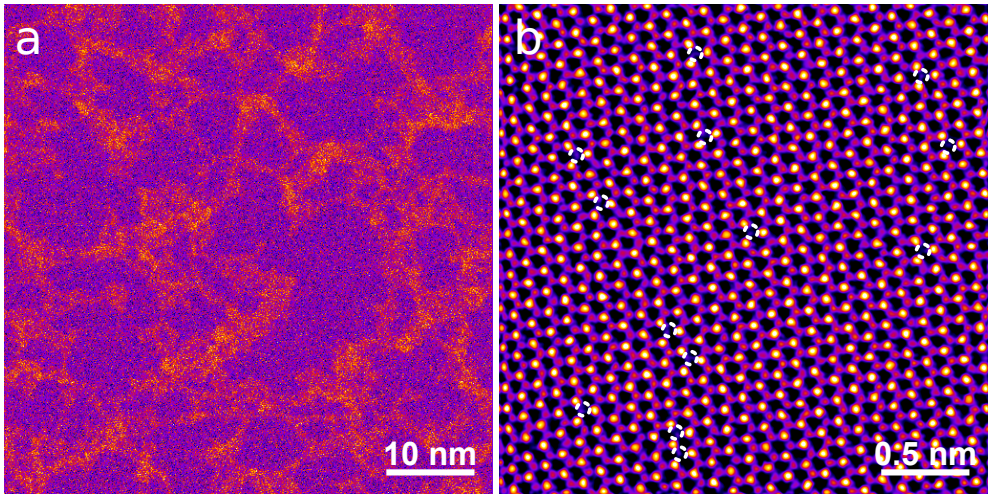

Figure 3.10: Monolayer pristine MoS_2 before irradiation. (a) STEM/HAADF overview image shows small clean areas of MoS_2. Brighter contrast represents contamination. (b) Double Gaussian filtered HAADF image shows the perfect atomic lattice of monolayer MoS_2. Single S vacancies caused by the electron irradiation during imaging have been highlighted. Due to their Z contrast [35], the heavier Mo atoms appear brighter in comparison to the S atoms.

grids. The irradiation experiments were performed at the the University of Duisburg-Essen HICS beamline [95], which contains an electron beam ion source that can deliver Xe ions with a maximum charge state of q= 48+. Samples were irradiated at room temperature and in $\sim 1 \times 10^{-9}$ mbar vacuum using different charge states within q = 20–40+, which can deliver potential energies in the range of 4.6 keV $\leq E_{pot} \leq$ 38.5 keV. Fluences ranged from ϕ = 28.00 μm^{-2} for Xe^{40+} up to ϕ = 18.000 μm^{-2} for Xe^{20+} at a perpendicular incidence angle. To study the effect of charge state and potential energy in the pore creation mechanism, the kinetic energy was kept constant for all the experiments with a value of E_{kin} = 180 keV. After irradiation, all samples were analyzed using the aberration-corrected Nion UltraSTEM100 in Vienna at 60 keV primary beam energy.

The STEM image in Figure 3.10 shows the pristine MoS_2 monolayer before irradiation. Figure 3.11 shows the presence of pores after irradiating the MoS_2 with highly charged Xe ions at different charge states. The shape of the pores is roundish as can be seen from the atomic resolution STEM images. Depending on the the charge state, the radius of the pores is increasing.

To investigate the dependency of the pore size on the charge state of the ion, the pore areas were estimated for each irradiation condition. Since the majority of the pores show a roughly round shape, the areas A have been measured using $A = \pi r^2$, where r is the radius. As an example, pore size histograms for Xe^{20+}, Xe^{31+} and Xe^{40+} are shown in Figure 3.12. All histograms have been normalized and fitted with a Gaussian function. It is clear from the

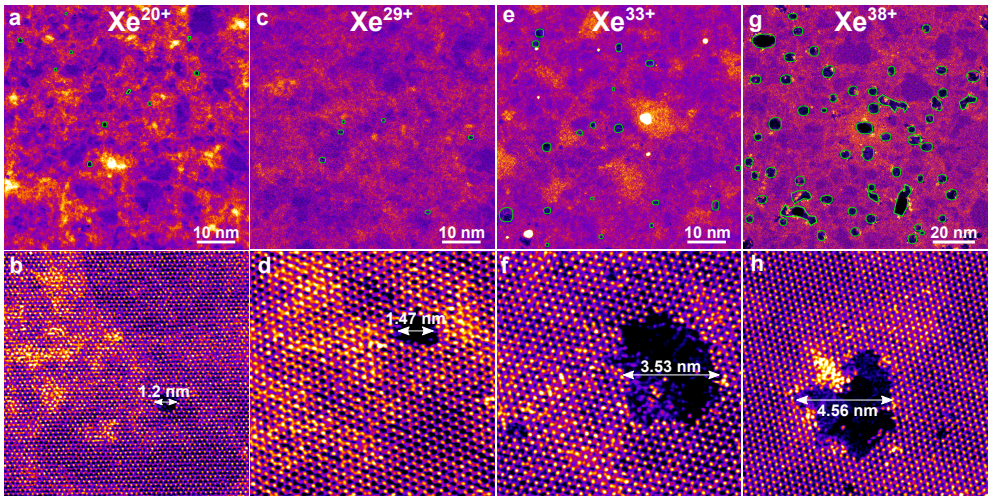

Figure 3.11: Pores in MoS_2 after irradiation with HCIs at different charge states. Pores have been overlaid with green circles (top row) to highlight them. Panels on bottom row have been processed to highlight the lattice.

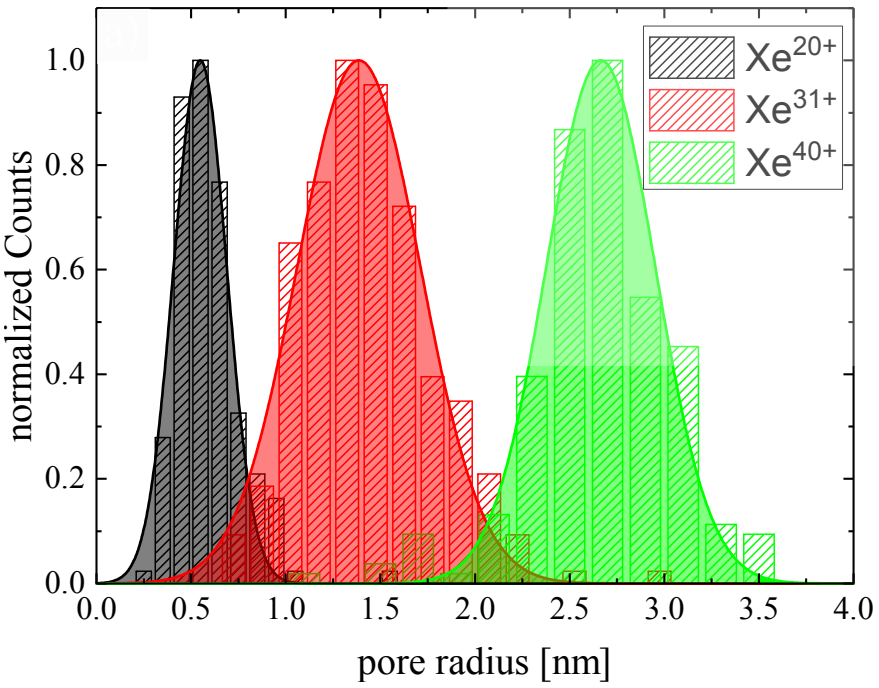

Figure 3.12: Normalized histograms show the distribution of MoS_2 pore sizes for Xe^{20+}, Xe^{31+} and Xe^{40+} ions. Each histogram is fitted with a Gaussian distribution.

histograms that for increasing charge state, the distribution shifts to larger radii. The mean value of the pore radius for the lowest charge state Xe^{20+} is ∼0.55 nm, whereas pores larger than 2.65 nm in radius are created by Xe^{40+} ions.

Figure 3.13a further shows a clear correlation between the potential energy and the pore radius for all charge states: the pore radii increase with the increase in the charge state. This dependency was best fitted using a linear function. We calculated the total number of missing atoms and found that on average ∼7 atoms per keV were removed from MoS_2 at low charge state 20+ (33 atoms in total), whereas at highest charge state 40+, this number increased threefold (∼20 atoms/ keV or 765 atoms in total). This can be understood by assuming that increasing potential energy leads to the sputtering of clusters of atoms which requires less energy than sputtering an individual atom as not all bonds must be broken [125]. As a consequence, more atoms (individually or in clusters) per energy unit can be emitted for higher charge states.

These results can be compared to those obtained for MoS_2 on a KBr substrate. In that case the pore radius is one order of magnitude higher than here [89], even though the kinetic energy used in our experiments is lower (180 keV instead of 260 keV). A reason for this discrepancy is the influence of

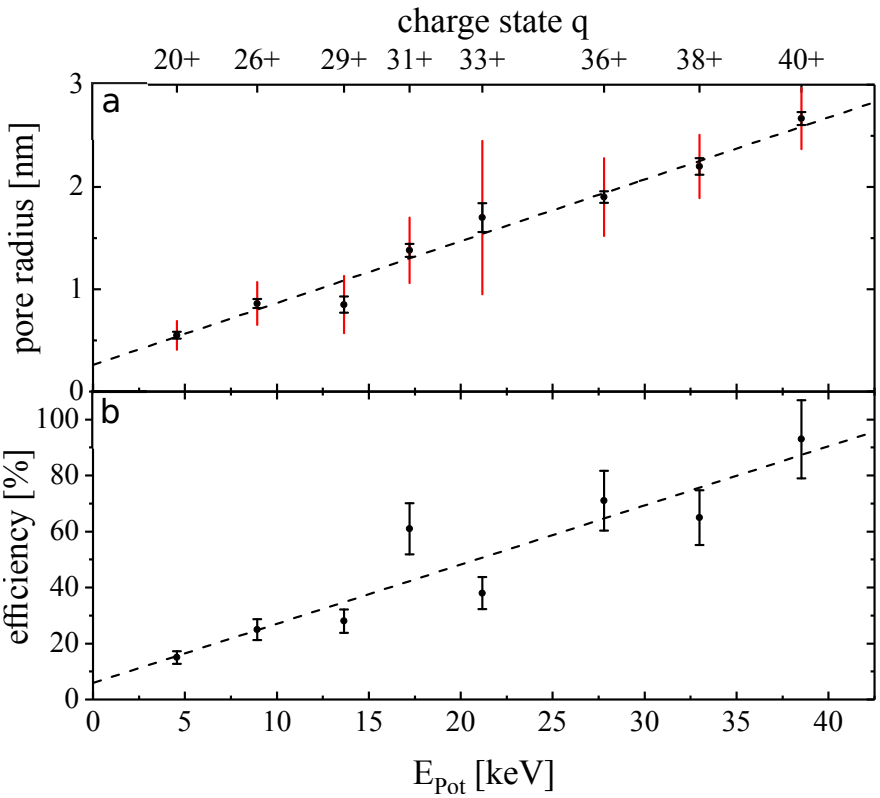

Figure 3.13: Charge state and potential energy dependency of pore creation in MoS_2. (a) A linear variation in pore radius with respect to the charge state or respective potential energy. (b) A direct correlation between the pore creation efficiency as a function of the charge state.

the substrate during the defect formation process, as also shown for graphene irradiation [126]. Atoms sputtered from the substrate may lead to additional removal of atoms from the material, resulting in an increase of the pore size for the supported structure [127].

We also calculated the probability to create a pore upon impact by dividing the pore density by the fluence. Interestingly, it is apparent from Figure 3.13b that the probability to create a pore decreases with decreasing E_{pot}. The pore creation efficiency for Xe^{40+} ions was (93 ± 14)%, which means that practically every incoming HCI created a pore in the sample. However, with decreasing potential energy of the ions, the defect creation efficiency decreases to (15 ± 2)%. It indicates that the probability for energy deposition from the HCI to the sample must depend either on the charge state or potential energy associated with the ion.

By decreasing E_{pot}, the radius can be reduced down to the offset value of the linear fit, representing the extrapolated limiting size of a pore that would

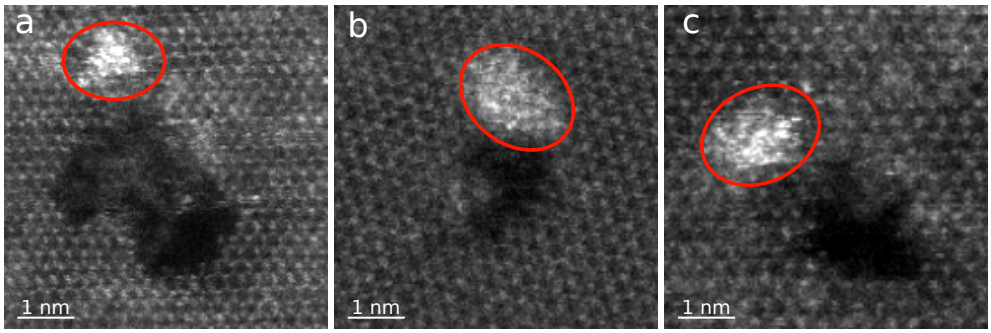

Figure 3.14: Mo rich areas next to HCI-induced pores in MoS_2.

be induced into a MoS_2 monolayer after interaction with a neutral Xe atom. Without potential energy, the pore creation process would be driven by the deposition of kinetic energy. This pore with a radius of 0.27 ± 0.06 nm would correspond to $\sim$9 missing molybdenum and twice as many missing sulphur atoms, and represents the lower limit of the achievable pore size in suspended MoS_2 by Xe irradiation for the given kinetic energy.

The impact of an HCI on a 2D material may lead to the emission of electrons and increase in temperature due to charge exchange between the ions and target atoms [90, 92, 128]. In the case of MoS_2, heat treatment and electron irradiation results in S vacancies, which can form into complex defects [37, 129]. Besides pore creation, lattice structure near the pore can be distorted when S atoms are sputtered. Red circled regions in the STEM/HAADF atomic resolution images of Figure 3.14 show Mo clusters near the pores.

Finally, the defect formation mechanism via highly charged ions should be similar for other TMDs. As a comparison, we also irradiated WS_2 with Xe^{40+} ions. The preliminary results show triangular pore formation in the WS_2 lattice (Figure 3.15). Magnified atomic resolution STEM/HAADF images show individual pores with sharp edges. The potential energy deposition of the HCI is very localized close to the surface [86], and interestingly, we observed the formation of pores in only the top layers, with a perfect atomic lattice of the bottom layers retained in bilayer WS_2 samples. Since triangular pores also have been observed due to premature termination of TMDs growth, this can not be totally excluded as an origin for these pores. Hence, a systematic study is required to investigate the pore-size dependency on the charge state and sample thickness.

In summary, we have shown here the first experiments on highly charged ion irradiation of freestanding monolayers of MoS_2 and compared them to irradiation of mono- and bilayer WS_2. The successful creation of pores in the otherwise pristine lattice of the TMDs was observed. In the case of MoS_2, the radius of the pores ranging from 0.55–2.65 nm was controlled by changing the charge state of the projectile. The kinetic energy was kept constant for all ex-

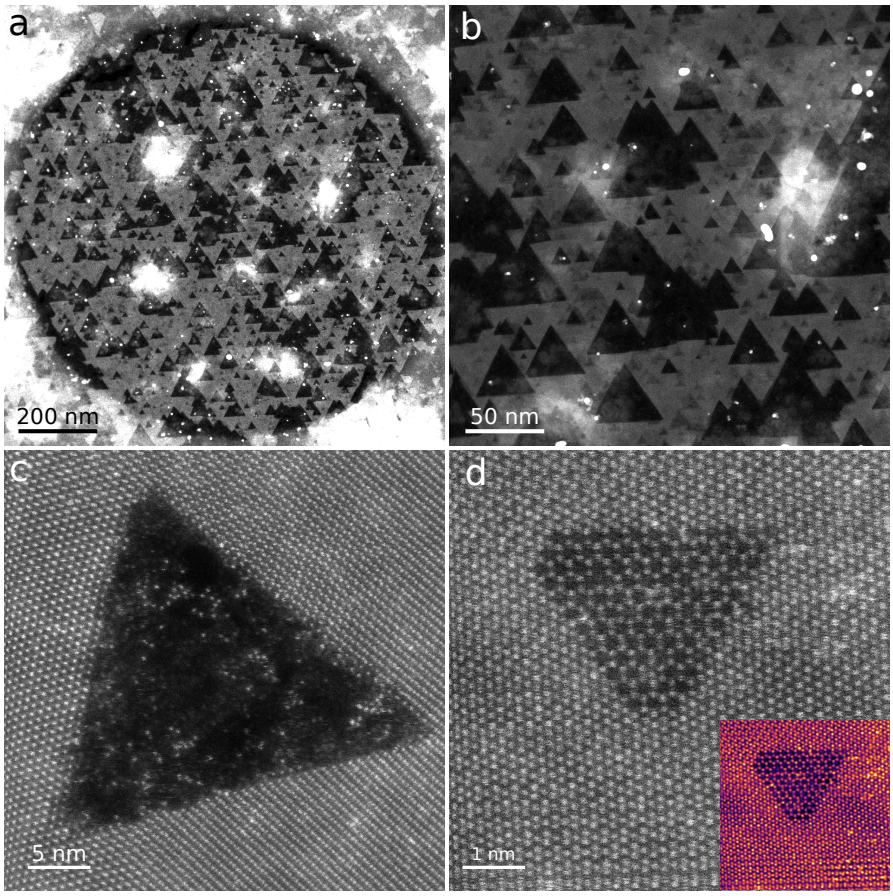

Figure 3.15: Triangular pores in WS_2. (a) Overview image after irradiation. (b) Magnified view shows clear sharp edges of triangular shaped pores. (c) Atomic resolution HAADF raw image shows individual pores in monolayer WS_2. (d) Atomic resolution HAADF raw and double Gaussian filtered (inset) image shows individual pores in bilayer WS_2.

periments and the deposition of the potential energy of the highly charged ion to the defect formation process at different charge states was studied, suggesting potential energy to be the only driving force for pore creation. Additional experiments need to be carried out to clarify the process in WS_2. Nonetheless, irradiation with highly charged ions clearly represents a novel technique for fabricating porous MoS_2 and WS_2 with pores in the size regime meeting the strict requirements of water desalination [130] or DNA sequencing [131].

3.2.2 Intrinsic nanopores along MoS_2 grain boundaries

We present here a detailed analysis of grain boundaries (GBs) in single-layer MoS_2. Grain boundaries are formed with the merging of differently oriented grains during growth. Atomic resolution imaging has been used to observe the GBs [56, 132], and the formation of nanopores and dislocation cores along them [55, 133]. Further, a dependency between the grain misorientation angle and the size distribution of nanopores along the GBs has been observed, where the density of dislocation cores and pore area increase with decreasing misorientation angle [55, 133]. However, until now only three nearly equal misorientation angles were studied. Interestingly, here we find a decrease in pore areas from ∼2–15° misorientation angle and then a nearly linear increase in area for higher angles. Moreover, the spacing between dislocation cores decreases with increasing grain misorientation angle.

MoS_2 samples were directly grown on SiO_2/Si substrates by CVD in Dublin [26] and transferred onto TEM grids as explained in Section 2.3.3. An aberration-corrected Nion UltraSTEM100 in Vienna operated at 60 kV was employed to map and image the grain boundaries at atomic resolution. Although this is lower than the knock-on damage threshold of MoS_2 [31], extended imaging can form defects and pores in the structure. Figure 3.16 shows STEM/HAADF images of various grain boundaries. Relative mismatch angles between two grain domains have been measured directly from the lattice orientations visible as two sets of reflections in the FFTs of the corresponding HAADF images.

Crack propagation near the grain boundary can be induced by electron irradiation [134, 135]. However, we observe here intrinsically present long and straight crack-like structures along the MoS_2 GBs (Figure 3.17). Although the surface is covered with hydrocarbon contamination, the adjoining of grains after large cracks is still clearly visible in magnified HAADF images.

Figure 3.18 shows a connected periodic chain of 4-8-4-membered rings between two different grain orientations at a relative misorientation angle of 60°. This particular GB structure is called a mirror twin or an anti-phase boundary [53, 133], predicted to be metallic in nature [54]. In addition to the periodic chain of dislocation cores, only one pore was found along this particular GB, in contrast to other mismatch angles where mostly larger pores were found.

Pore areas were directly measured from the atomic resolution HAADF images. The geometric mean (G.M.) of pore areas with respect to misorientation angle is shown in Figure 3.19. The scatter plot shows a decrease in pore area from ∼14 nm^2 to ∼2 nm^2 with increase in relative misorientation angle until 15° and then a nearly linear increase in area up to ∼32 nm^2 until 30°. However, most of the grain angles are close to ∼10–15°. A histogram in Figure 3.19b shows the pore area distribution for all the mismatch angles, with a mean close to ∼2.23 ± 0.21 nm^2.

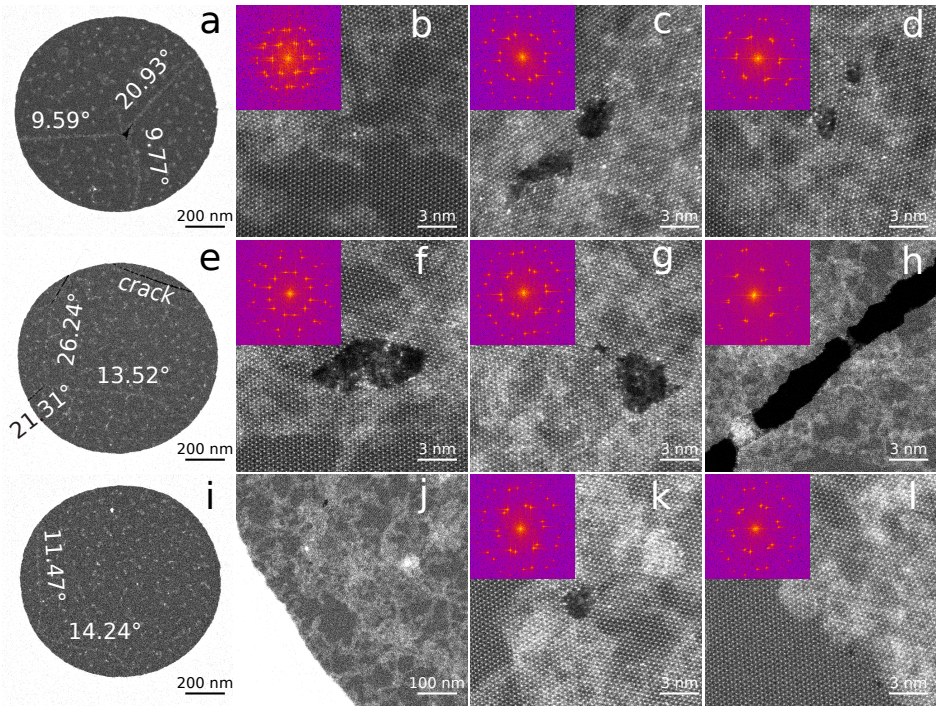

Figure 3.16: STEM/HAADF images of grain boundaries in MoS_2. Overviews (a), (e) and (i) show a position of grain boundary junctions. Zoomed-in images in the remaining panels present pores along the respective grain boundaries. Relative angles are measured from FFTs from the magnified images and are highlighted on the overview panels.

Hydrocarbon contamination sticks more to the grain boundaries than pristine regions due to their reactive nature [55]. Additional intensity in atomically resolved HAADF images corresponds to these contaminants, visible in all top panels of Figure 3.20. However, after subtracting background from the images, a linear arrangement of the dislocation cores in the structure along the GBs can be clearly seen. A Burgers closed circuit drawn in white is used to display the dislocation cores and a Burgers vector drawn in red provides a shortest dislocation edge (usually the nearest neighbor inter-atomic distance) [136]. As an example, Figure 3.20c shows seven Burger circuits overlaid around (1,0) dislocation cores along the GBs.

Geometric phase analysis (GPA) [137] can be used for estimating strain and local displacement with the STEM-CELL [138] software tool also used previously [55] to analyze the strain components along GBs. The lower panels in Figure 3.20 show the position of individual dislocations, matching the contrast of the HAADF images in the top panels. The panels in the bottom row show the geometric phase analysis ε_{xx} component strain maps displaying lobes configured in regular arrangements.

Dislocation spacings have been measured both directly from the experimental images and from the strain maps. The Frank-Bilby equation [139, 140] $d = b/[2\sin(\theta/2)]$ is commonly used to describe a relation between the dislocation spacing d and mismatch angle θ, where b is the length of the Burgers vector [141]. Figure 3.21 shows a plot of the average dislocation spacing as a function of relative mismatch angle between two grain domains, fitted with a double logarithmic reciprocal function [142]. Dislocation spacing is decreasing with increasing mismatch angle between adjacent grains. In earlier studies, this dependency of dislocation spacing was shown for small mismatch angles only. Here, we show a direct correlation between dislocation spacing for relative misorientation angles up to 22°, which agrees very well with the Frank-Bilby equation, confirming the presence of higher dislocation spacing at very small angles that decreases exponentially as a function of mismatch angle.

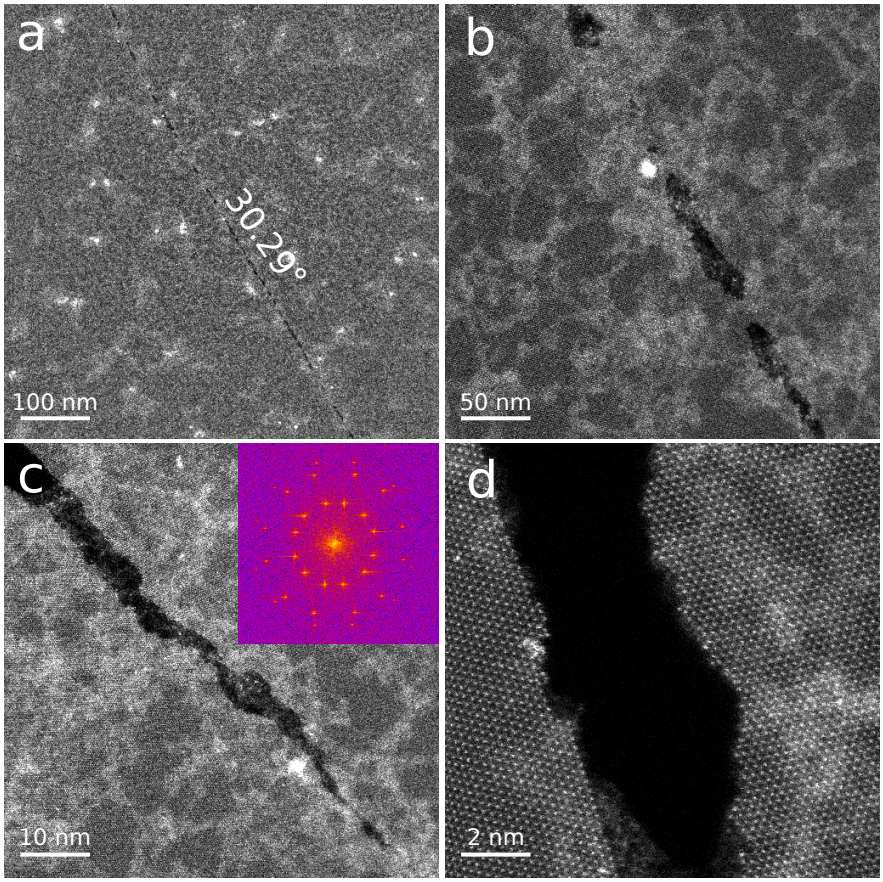

Figure 3.17: STEM/HAADF images of cracks at MoS_2 grain boundaries. (a) Overview image shows a long and straight crack-like structure. Panels (b–d) shows zoomed-in images with long pores along the GB with a relative mismatch angle of 30.29°.

In conclusion, we have made an extensive study of the grain misorientation-dependent size distribution of nanopores and dislocations along MoS_2 grain boundaries. Pore areas decrease from ∼14 nm^2 to ∼2 nm^2 with increase in relative misorientation angle until 15° and then show a nearly linear increase up to ∼32 nm^2 at 30°. The dislocation spacing decreases exponentially with the increase in relative mismatch angle, in agreement with the Frank-Bilby equation. In addition to cracks at a high misorientation angles, a mirror twin boundary with a connected periodic chain of 4-8-4-membered rings between two opposite grain orientations has been presented. Similar to the ion-induced pores in MoS_2 as described in the previous Section, intrinsically present nanopores along the GBs might also be used for potential applications.

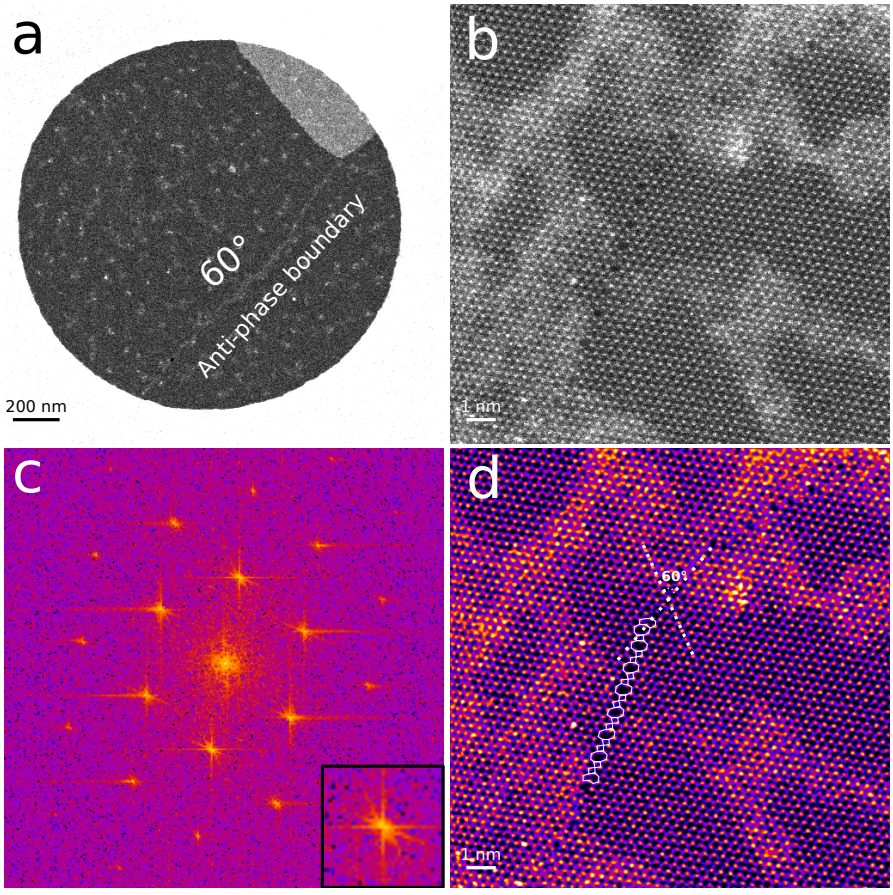

Figure 3.18: STEM/HAADF images of a 60° grain-boundary in MoS_2. (a) Overview image. (b) Atomic-resolution image of a connected periodic chain of 4-8-4-membered rings between two grains. (c) HAADF image (b). Inset shows only one set of Bragg reflections. (d) Double Gaussian filtered image of panel (b) with overlays.

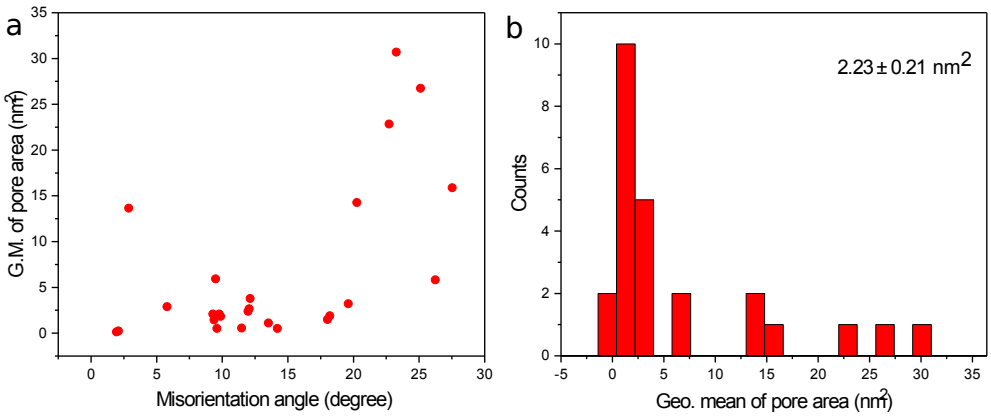

Figure 3.19: Pore area analysis at MoS_2 grain boundaries. (a) Distribution of the geometric mean of nanopores with relative misorientation angle. (b) Histogram of all geometric mean values.

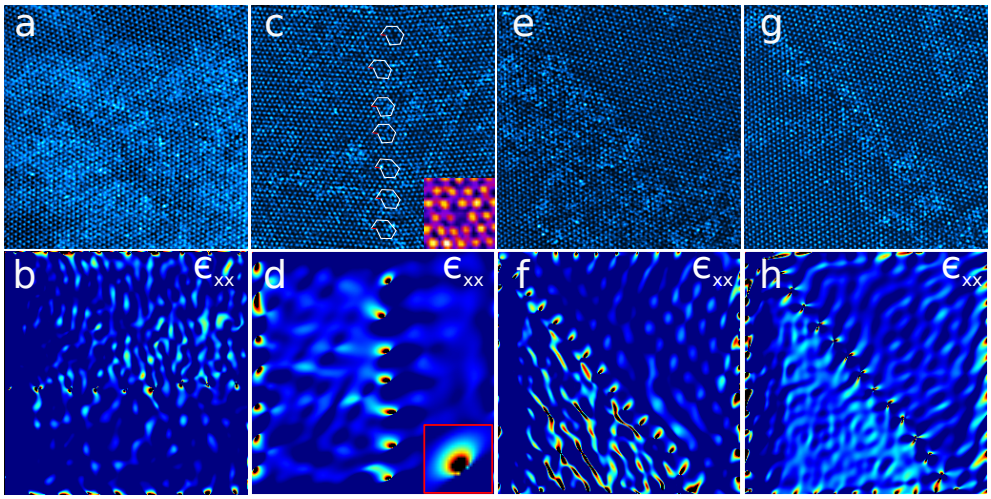

Figure 3.20: Dislocation cores along GBs. Top panels show background-subtracted filtered STEM/HAADF images. Bottom panels show geometric phase analysis ε_{xx} component strain maps from the corresponding images in top panels. White lines show Burgers circuits around dislocation cores and red lines indicate the Burgers vectors, which equals the lattice unit of MoS_2. Field of view for all panels is 5×5 nm^2.

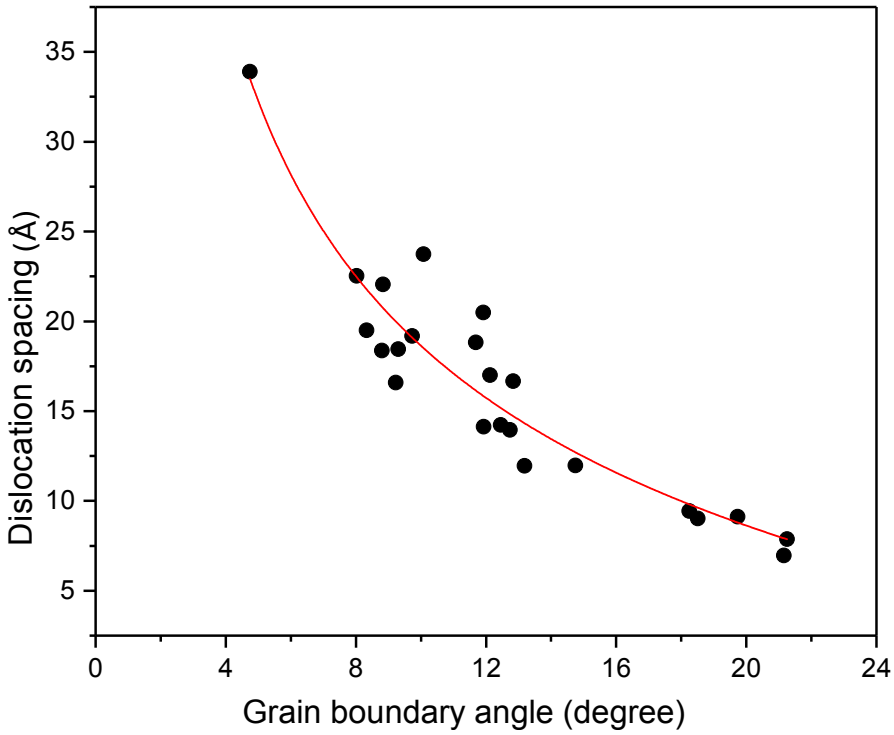

Figure 3.21: Dislocation spacing as a function of the misorientation angle between adjacent grains based on the Frank-Bilby equation.

3.3 Implanting germanium into graphene

This Section is dedicated to the incorporation of low-energy $^{74}Ge^{+}$ ions into single-layer graphene. The content is based on entry 2 of the list of publications.

Silicon is an ubiquitous impurity in graphene [45, 143, 144], and very recently also the slightly heavier phosphorous ions were implanted into the lattice [46]. Atomic resolution imaging in combination with EEL spectroscopy confirmed that the dopant atoms directly substituted single C atoms and bonded in graphitic configuration. Germanium is a structural and electronic analogue to silicon, but significantly heavier (atomic number 32 as compared to 14) and larger (covalent atomic radius of 122 pm as compared to 111 pm for Si and 77 pm for C). Following the successful implantation of lighter heteroatoms [40, 46], it was not clear whether heavier dopants can also be incorporated in graphene in the same manner.

It has been predicted that the bond length between Ge and C will result in a three-coordinated Ge to buckle out of the graphene plane [145]. Its structurally isovalence with Si anticipates [45] another possible bonding: a planar four-coordinated substitution in a graphene divacancy. From DFT simulations, it was predicted that doping graphene with germanium can open and control the band gap depending on concentration [145, 146]. However, direct evidence for the stability of direct lattice substitutions was lacking. We show here the first successful incorporation of Ge impurities into the graphene lattice using ion implantation.

Low-energy $^{74}Ge^{+}$ ions were implanted into commercially available monolayer graphene supported on Au TEM grids (Quantifoil® 2/4, Graphenea). A details description of the ion implantation can be found in Section 2.5.1.1. Ion energies in the range of 15–25 eV were chosen in order to suppress radiation damage. The transferable kinetic energy to a carbon atom in a head-on collision with such an ion is below the experimentally estimated displacement threshold energy of graphene (21.14 eV) [107]. However, due to a strong chemical effect between the incoming Ge ion and the structure around the C atom being displaced, these energies are sufficient as confirmed with simulations [47]. Unfortunately, contamination remains an issue for the ion-implanted samples, as explained earlier. In an effort to reduce it, laser annealing [121] was done using a 445 nm laser diode, aimed at the sample through a view port of the vacuum chamber both for 2 min before (nominal laser power 480 mW) and during the implantation (240 mW).

All samples were characterized in the Nion UltraSTEM100 operated at 60 kV. The atomic resolution STEM/MAADF image in Figure 3.22a shows an overview of a graphene sample irradiated with 20 eV $^{74}Ge^{+}$ ions. Most of the graphene surface is covered by a thick layer of contamination despite the laser annealing. Contamination introduced during implantation degrades

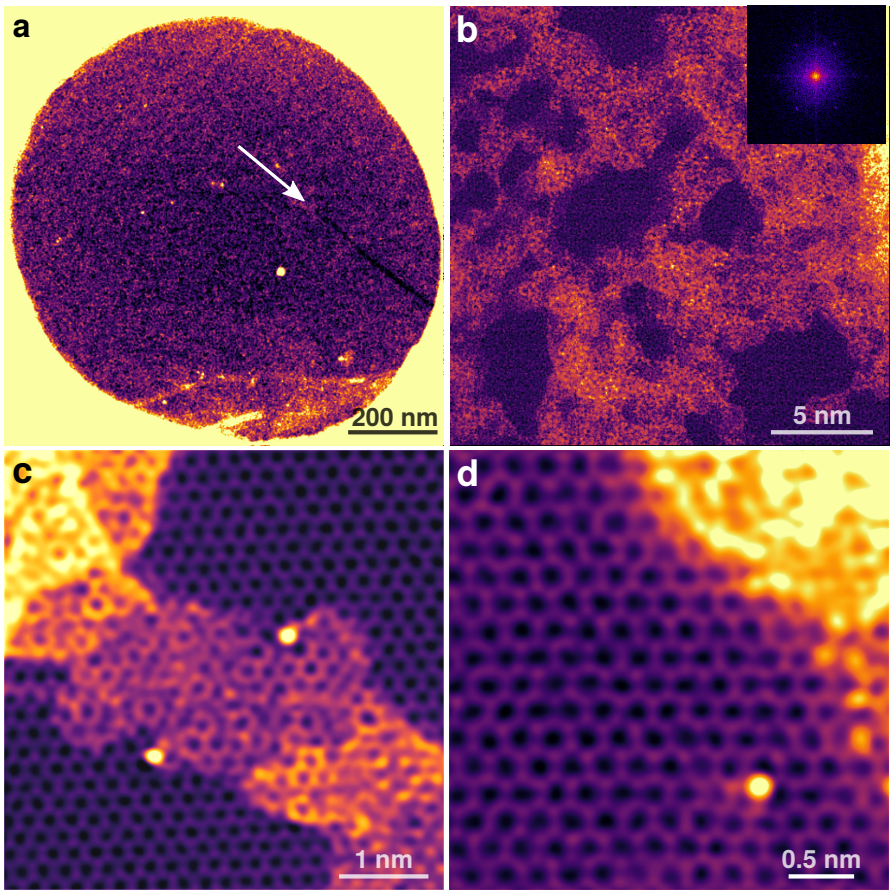

Figure 3.22: Overview images of a graphene sample implanted with 20 eV $^{74}Ge^{+}$ ions (MAADF/STEM, 1024×1024 px). (a) Raw image of heavily contaminated graphene suspended over a Quantifoil® hole after ion implantation, with the arrow indicating a narrow cleaner region. (b) Clean monolayer graphene areas some tens of nm^2 in size were found in this region. The FFT of the inset shows the hexagonal structure of the graphene lattice. (c) Two Ge atoms bonded at the edge of overlaying graphitized contamination. (d) A single Ge atom incorporated into the graphene lattice. (b-d) have been processed with double Gaussian filtering [35].

sample quality and makes electron microscopic characterization difficult. The degree of contamination was however not entirely consistent: in some samples we were not able to find any clean lattice despite extensive searching, whereas in others this was rare, but included regions with implanted impurity atoms. The arrow in Figure 3.22a shows the only clean regions (few nm^2) within this Quantifoil® hole. One possible explanation is that the alignment of our laser was not fixed and varied between the different experiments.

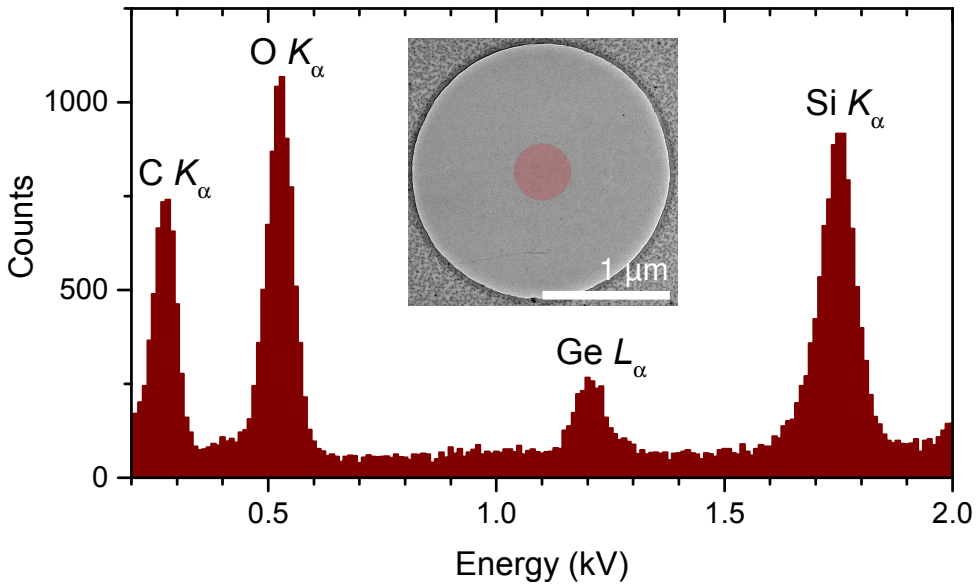

Figure 3.23: Spectroscopic characterization of implanted germanium. EDX spectrum with the approximate beam size indicated by the colored red area in the inset bright-field image of graphene suspended over a hole in the Quantifoil®.

Most of the data is from the cleanest sample that was irradiated at 20 eV. We did also find one incorporated impurity atom in a sample irradiated at 15 eV, but did not find a single Ge impurity in the 25 eV sample as it was totally covered with contamination. Due to this lack of statistics from different ion energies, it is difficult to deduce the ideal implantation energy from the experiments. In total, we found only seven Ge impurities directly in the lattice (roughly 1500 nm^2 of clean lattice was analyzed; with our ion fluence of 1 ion/nm^2, this yields an implantation efficiency of just 0.5%). Figure 3.22b shows an example of a somewhat clean sample area, illustrating how most lattice areas do not contain any Ge atoms, nor we did find defects in the lattice. Examples of two Ge impurities bonded at the edge of an overlaying contamination layer are shown in Figure 3.22c. Finally, Figure 3.22d shows a single Ge atom directly substituting a single carbon atom and bonding to three carbon neighbors in lattice.

ADF imaging in combination with EELS is usually the best tool for establishing chemical identities and bonding at the atomic level [46, 147, 148]. However, Ge impurities in graphene present a particular challenge: the weak Ge L-edge is located at ∼1150 eV, beyond the range of our spectrometer, whereas the $M_{4,5}$-edge, located at ∼32 eV, falls under the much more intense graphene $\pi + \sigma$ plasmon (which is further influenced by nearby contamina-

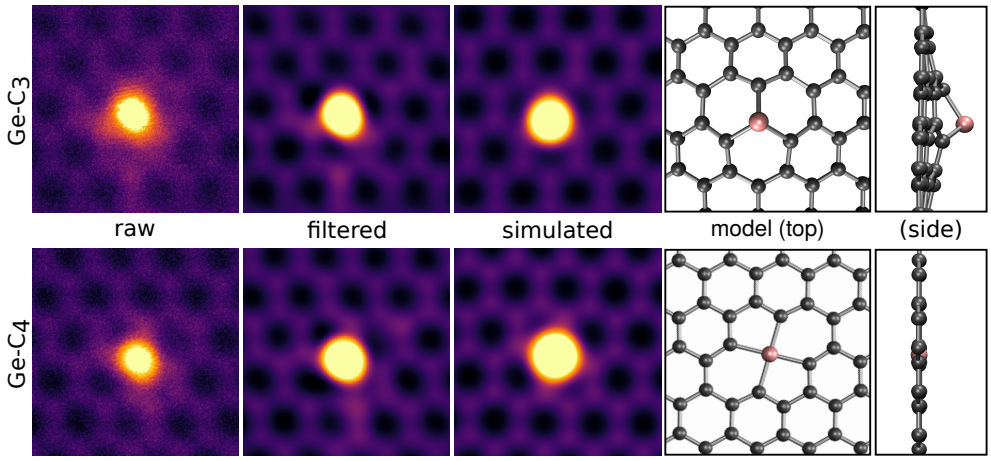

Figure 3.24: Germanium substitutions in graphene (top: three-coordinated single atom substitution, Ge-C_3; bottom: four-coordinated substitution in a double vacancy, Ge-C_4). The raw STEM/MAADF images have been averaged from 7 and 40 frames, and further double Gaussian filtered. Quantitative STEM simulation using our experimental parameters reproduces in both cases the high intensity of the Ge impurity. DFT simulations show that while the Ge-C_3 impurity buckles out of the graphene plane, the Ge-C_4 site is flat. The fields of view are $1{\times}1$ nm^2.

tion [149, 150]). The presence of Ge was thus confirmed through EDX in a Philips CM200 TEM instrument, operated at 80 kV. Figure 3.23 shows the clear intensity peak of Ge in the EDX spectrum acquired from the red circled region shown in the inset. The samples were further characterized in another TEM at University of Manchester to try to collect high resolution EDX of individual Ge atoms. However, detecting their spectroscopic signature was not possible due to their instability at the used 80 kV acceleration voltage.

Figure 3.24 shows atomic resolution STEM/MAADF images of a single germanium impurity in three-coordinated (Ge-C_3, top row) and four-coordinated (Ge-C_4, bottom row) configuration. To enhance the signal-to-noise ratio, multiple raw images have been aligned on top of each other and their intensities averaged. Double Gaussian filtering [35] has been used to remove the electron beam probe tails from the averaged MAADF images in both configurations, as can be seen in the second panels. Due to a very high scattering signal from the Ge impurities, their contrast is extremely intense in comparison to the C atoms even to the MAADF detector, making it difficult to distinguish the local bonding in the structure.

Simulated images of three-coordinated (Ge-C_3) and four-coordinated (Ge-C_4) germanium substitutions [47] in graphene match well with the double Gaussian filtered images as presented in Figure 3.24. Since images acquired

with the MAADF detector may have coherent contribution leading to additional image intensity, intensities of the atoms have been calculated from images recorded with the HAADF detector. We found the ratio of the intensity of the Ge impurity atom to that of C atoms distant from it as 21.5 ± 0.9 for Ge-C_3 and 21.7 ± 1.0 for Ge-C_4, with simulated ratios respectively of 21.8 and 22.5. This corresponds to a Ge/C contrast proportional to $Z^{1.86}$, confirming the chemical identity of the impurities. Significant structural rearrangement around the Ge-C_3 site was theoretically expected [145] and our DFT simulation reproduces the results with the Ge atom buckling 1.90 Å out of the graphene plane as shown in the top and side views of the relaxed model structure in Figure 3.24. A detailed description of the simulations can be found in Ref. [47].

In summary, we have implanted thus far the heaviest directly observed graphene impurity, and shown that despite its larger size, germanium can substitute a single atom, bonding to three carbon neighbors. This demonstrates that elements from the fourth period may be incorporated into the graphitic lattice, suggesting that substitutions from groups 3–13 with possible applications including single-atom catalysis and magnetism may also be possible. However, there are two fundamental challenges to achieving high-quality ion implantation of graphene. First, contamination induced during implantation remains a serious issue. Annealing samples using a heating holder during irradiation may remove contamination, and thus increase the achievable doping. Secondly, the used ion energies should be precisely measured. Addressing these two issues can improve the sample quality in future experiments. Nevertheless, ion implantation continues to progress as a versatile tool for large-scale and precise doping of low-dimensional materials.

3.4 Beam-driven dynamics at heteroatom sites

This Section is dedicated to electron-beam induced dynamics of N, Si, P and Ge impurities in single-layer graphene. The content is based on entries 2, 3, 6 and 7 of the list of publications.

During STEM imaging, electrons can transfer momentum (and energy) to individual atoms giving rise to interesting dynamics. However, considering a single-electron elastic collision in the static lattice approximation, a STEM probe at 60 keV energy can transfer only about 10.9 eV [43] to a static C atom, whereas many dynamics take place in the 15 eV energy range. However, in the presence of lattice vibrations there is greater energy transfer [107], making it possible to trigger such dynamics. Further details may be found in Refs. [106, 151].

Several atomic level dynamics have been reported at energies below the displacement threshold [32], such as Stone-Wales transformations by rotating a C-C bond, or the migration of dislocation cores [152] and double vacancies [36] in graphene. Electron-beam induced atom-conserving dynamics of impurity atoms in graphene include the bond-inversion between Si and C [115], B and C or N and C [42, 147, 153]. Following this mechanism, the directional manipulation of Si atoms in graphene has been demonstrated [144, 154, 155], as will be further discussed in Section 3.5. Further dynamics with Si atoms such as their trimer rotation or of Si_6 clusters in a pore in graphene [156] have also been observed.

The elemental identification of individual impurities can be done using quantitative intensity analysis from ADF imaging and using electron energy loss spectroscopy. Figure 3.25 shows a double Gaussian filtered STEM/MAADF image with three Si atoms in the graphene lattice. Si impurities in graphene [45, 143] or in SWCNTs bond in a three-coordinated out-of-plane (Si-C_3) atomic configuration where a Si atom substitutes a single C atom and bonds directly with three neighboring C atoms as can be seen in Figure 3.25a (bright atoms in bottom-left and top-right positions). Si atoms can also be found in a four-coordinated planar [157] atomic configuration (Si-C_4) at a double-vacancy site in graphene, bonding with four neighboring C atoms (bright atom close to center) as shown in Figure 3.25a. Figure 3.25b exhibits the EEL spectrum of an individual three-coordinated atom in graphene whose Si $L_{2,3}$ edge confirms the identity of Si.

In this Section, we present the beam-driven dynamics of nitrogen, phosphorous and silicon dopants in graphene and also the dynamics of Si in single-walled carbon nanotubes, caused by electron irradiation. Purposeful manipulation will be discussed in the next Section.

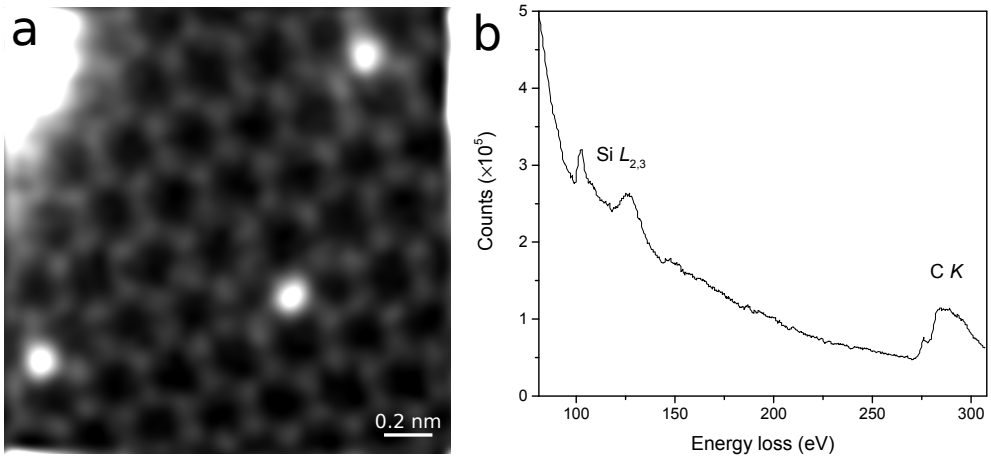

Figure 3.25: (a) STEM/MAADF image of individual three-coordinated and four-coordinated Si atoms in monolayer graphene. Image has been processed using double Gaussian filtering. (b) Elemental identification of a single Si atom in graphene via EELS (Si $L_{2,3}$ edge) collected at an acceleration voltage of 55 kV.

3.4.1 Pyridinic nitrogen in graphene

The bonding configurations of N impurities in CNTs [158] and graphene [42] can be mainly categorized into three atomic structures: graphitic/substitutional (N is bonded with three C neighbors), pyridinic (N is bonded with two C neighbors next to a monovacancy) and pyrrolic (N is bonded with two C neighbors in a pentagon). Similar to the Si-C bond inversion in graphene, N atoms can also switch their positions with C [153], while the latter two atomic configurations are rarely observed [148]. Pyridinic configurations tend be very reactive and attract various transition metal atoms to the defect site [42]. Due to electron beam irradiation, N atoms in pyridinic configuration have also been seen to jump across a monovacancy in graphene heated to 500°C [42].

Here, we observe several cases of pyridinic N atoms in STEM at primary beam energies of 55 and 60 keV, observing repeated hopping across a monovacancy in graphene at room temperature. Figure 3.26 shows selected STEM/MAADF images from two such series.

Pyridinic N atoms can remain stable for many frames before ejecting from the lattice upon electron-beam irradiation, forming a divacancy which starts migrating and transforming to more complex defect structures by rotating bonds [28, 32, 36]. Currently, the mechanism of repeated hopping across a vacancy in graphene is not fully clear and there is a large discrepancy between theoretical and experimental cross section values for these jump dynamics [153].

Figure 3.27 shows selected STEM/MAADF images from a long series with a point defect of one Si atom and one N atom replacing three C atoms in the lattice. Direct bonding of N with Si has been observed with ADF imaging and confirmed via EELS [149]. Interestingly, here we observe a new process for the directly bonded N and Si atoms where they switch their positions thus also changing the positions of the 5-membered rings.

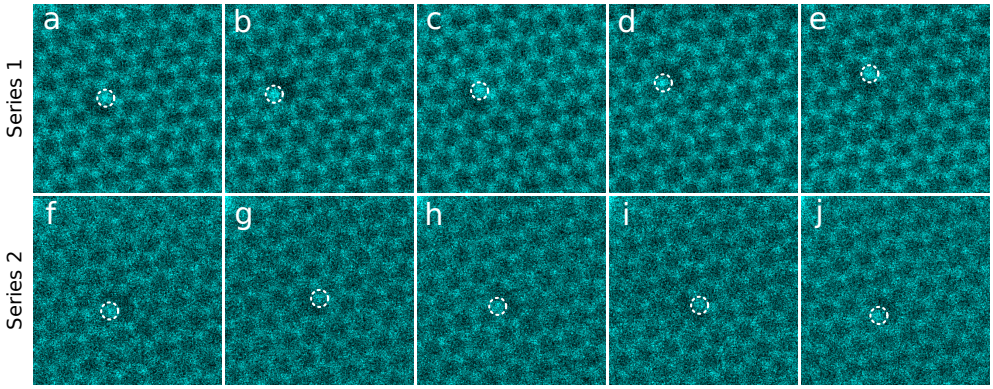

Figure 3.26: STEM/MAADF images show two series of a N dopant in pyridinic configuration jumping across a vacancy (highlighted with dashed white circles). The dose per frame was 2.3×10^6 $e^-/Å^2$.

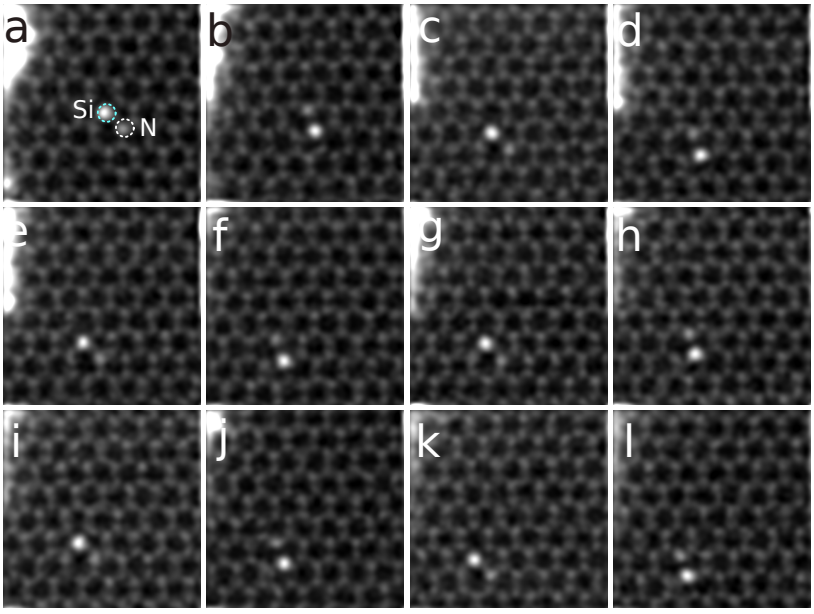

Figure 3.27: STEM/MAADF images showing selected frames out of a long series where Si and N atoms are switching places at a point defect in single-layer graphene. The dose per frame was 1.1×10^6 $e^-/Å^2$.

3.4.2 Phosphorus and germanium substitutions in graphene

Atomic resolution STEM imaging in combination with EELS has demonstrated the incorporation of phosphorus atoms in a buckled substitutional configuration in the graphene lattice [46]. Here, we focus on the atomic dynamics of individual P dopants. Targeting the Å-sized electron probe over a specific C atom induces certain dynamics with a significant probability. Atomic dynamics of P dopants can be primarily categorized into two parts: atom-conserving and atom non-conserving. In atom-conserving, no atoms are lost from the structure. In atom non-conserving, atoms are either lost by knocking out a C neighboring atom or the P is replaced by C, thus modifying the chemical stoichiometry.

To incorporate the impurities, low-energy P ions were earlier implanted into commercial monolayer graphene (Quantifoil® 2/4, Graphenea). More details about the ion implantation process, the atomic configuration and the elemental identification of P can be found in Ref. [46] as the same sample was used for our manipulation experiments. An additional sample was synthesized with CVD, with details given in Ref. [43]. Samples was characterized in the Nion UltraSTEM100 operated at 60 kV. The beam current was close to 50 pA.

Figure 3.28 shows an example of the conversion of a three-to four-coordinated P, bonded to three C neighbors in its initial position (Figure 3.28a). Due to an ejection of a C neighbor it changed configuration to being bonded with four C atoms in a graphene double vacancy (panel b). Once they change their coordination, impurity atoms can no longer be manipulated in graphene [44].

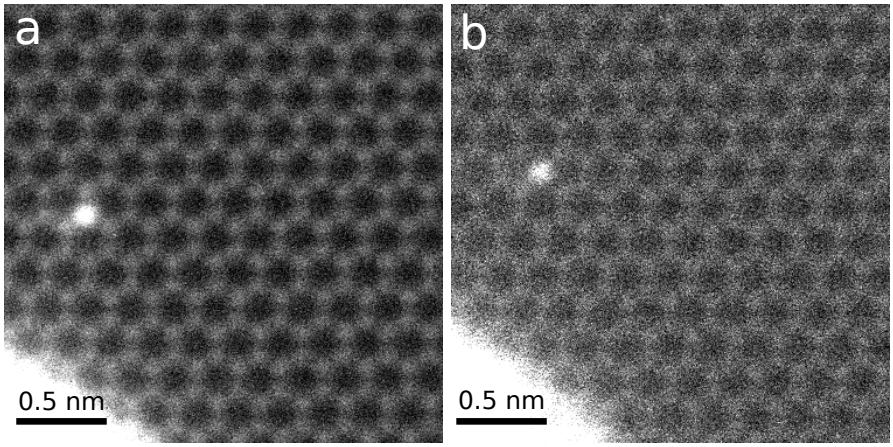

Figure 3.28: STEM/MAADF images of a three-to-four coordinated conversion of a P dopant due to spot irradiation. (a) P bonded to three C atoms. (b) P atom changes its symmetry to four-coordinated due to knocking out of a C neighbor.

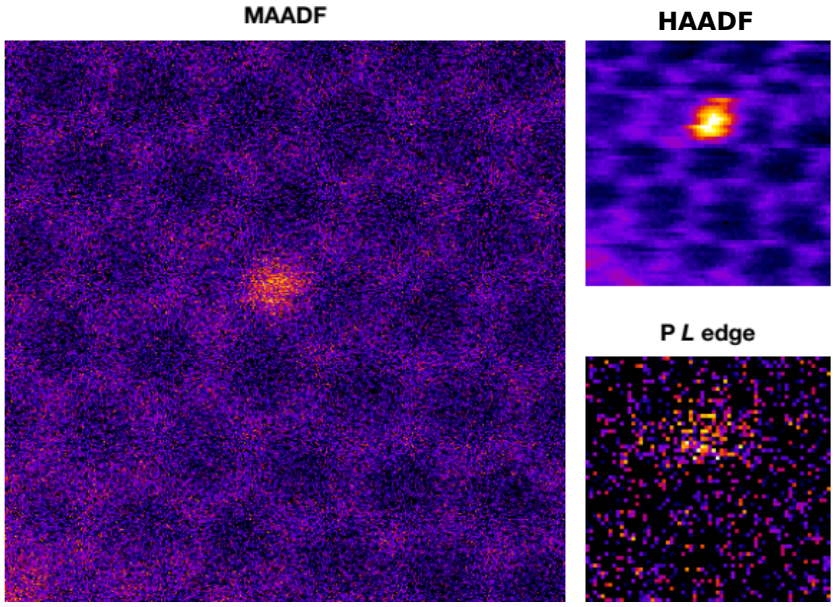

Figure 3.29: STEM/MAADF image of a four-coordinated P and a EEL spectrum image of the P L edge response and the corresponding HAADF image.

EELS spectrum imaging in combination with ADF allows to identify the impurities. Figure 3.29 shows an EEL spectrum image of a four-coordinated P in graphene. Due to the long acquisition time, scan distortions can be seen in the corresponding HAADF image; nevertheless, the P L edge response can be located on the impurity in the spectrum image.

One of the P lost a C neighbor, and seven were replaced by C, which is the most commonly observed outcome for P impurities after on average 22 ± 5 (mean ± std.err.) 10 s spot irradiations. This is in stark contrast to Si, for which we never observed such replacements. Figure 3.30 presents two different cases of P replacement. Since the displacement cross section for the heavier P atom is several orders of magnitude smaller than that for the lighter C atoms at 60 keV, we never observed a P being simply knocked out leaving a vacancy behind. A plausible explanation for the replacement process is that there are many C adatoms present on graphene surfaces under the electron beam in the microscope from the ubiquitous contamination. They tend to be highly mobile under the beam [159], and a diffusing carbon adatom needs only a small amount of energy to replace the dopant (for details, see Ref. [43]).

For Ge impurities, the displacement threshold energy is 11.75 eV, almost an order of magnitude more than what a 60 keV electron can transfer to such a heavy nucleus. However, we observed a similar replacement process where several Ge impurities got replaced by C (Figure 3.31a–c). In another case, Ge was replaced by a Si atom (Figure 3.31d–e).

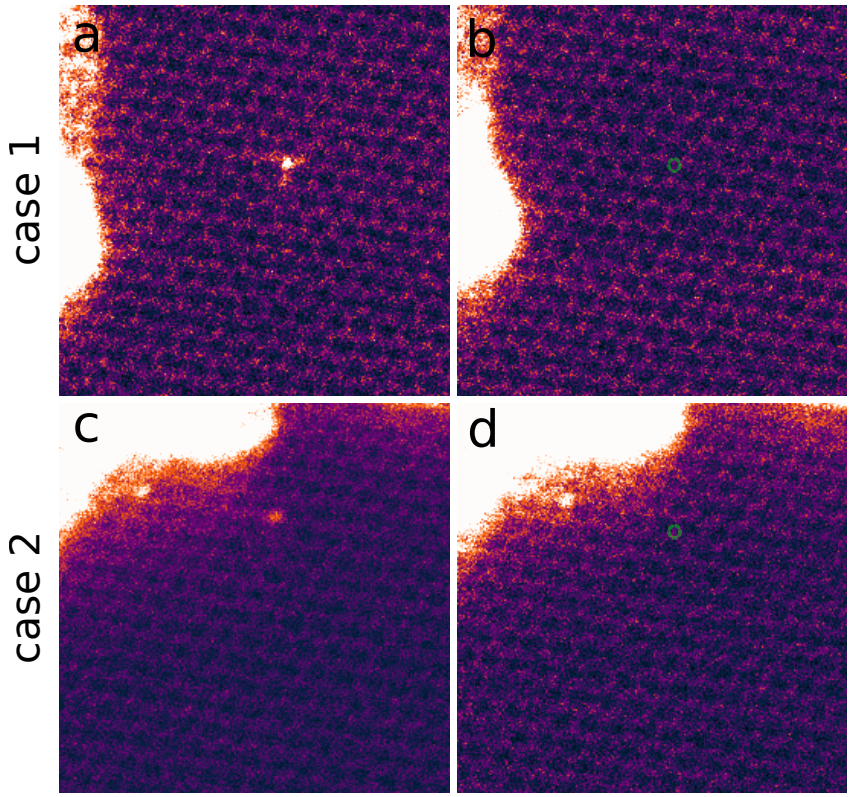

Figure 3.30: Two cases of P replacement by C atoms. STEM/MAADF images in (a & c) show three-coordinated P atoms in graphene. P atoms were replaced by C due to spot irradiations where the beam was iteratively parked on a C neighbor for 10 s. Green circles in (b & d) show the initial positions of the P atoms.

3.4.3 Silicon impurities in graphene and SWCNTs

A Stone-Wales transformation (rotation of a C-C bond) can be caused by the impact of an individual electron at energies below the carbon threshold displacement energy [32]. However, it is very rarely observed in pristine graphene at low acceleration voltages (for example at 60 or 55 kV), possibly because the back-transformation rate is too fast for it to be captured [160]. Interestingly, we did not observe any cases of Stone-Wales dynamics close to impurity atoms in graphene at 60 kV but did see them at 55 kV. DFT/MD simulations reveal that the local perturbation caused by the impurity allows this process to be activated by impacts with energies between 19.675 and 20.125 eV on the next-nearest C neighbor [107, 161] (and for a perpendicular momentum transfer, contrary to the pristine case [162]). Figure 3.32 shows two different examples of reversible Stone-Wales transformations at Si sites. We also observed a Stone-Wales defect in a SWCNT near the Si site as shown in Figure 3.33.

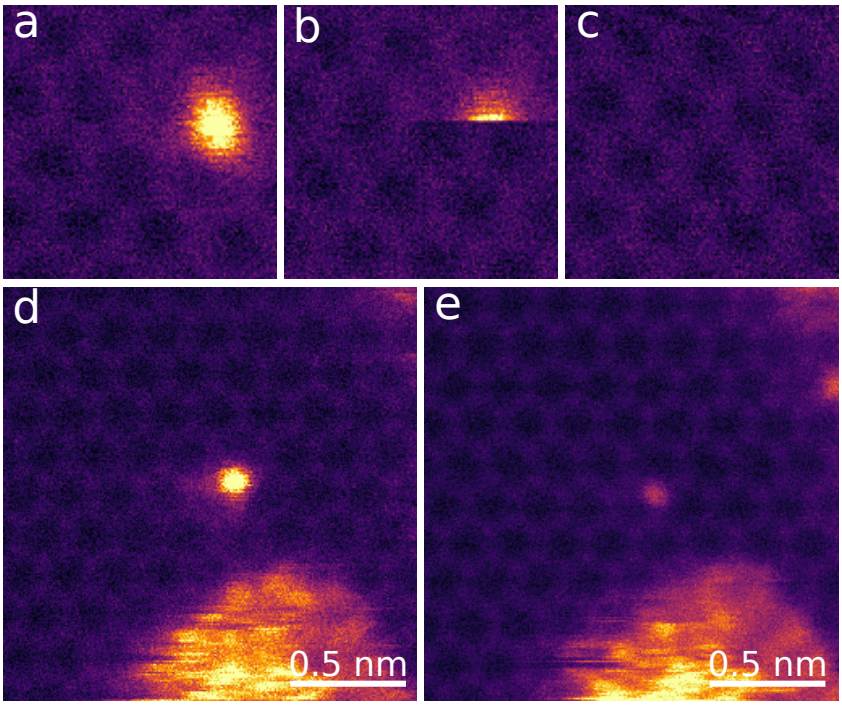

Figure 3.31: Ge replacement under electron irradiation (MAADF/STEM). (a–c) Three consecutive raw images of a single Ge impurity being replaced by C during the second frame (∼4 s per frame). (d,e) Replacement of another Ge impurity by Si.

In SWCNTs, we also observed various kinds of electron-beam induced dynamic processes that were more frequent in tubes smaller than 2 nm in diameter, whereas in larger ones jumps were prevalent. Examples are shown in Figures 3.33–3.35. Interestingly, we observed an event where the Si atom was ejected leaving a monovacancy behind; due to their low diffusion barrier and instability, monovacancies are not commonly found either in graphene or in SWCNTs. Notwithstanding, this vacancy created by the ejection of Si appeared to remain stable over timescales required to acquire a frame with our microscope (∼10 s), of which an example is shown in Figure 3.35b. Finally, we also noticed the frequent replacement of Si atoms in SWCNTs in contrast to graphene where this was never observed. The example images in Figure 3.36 show two different events where a single Si was replaced by a C atom.

In summary, we have presented electron-beam induced dynamics of individual heteroatoms in graphene and SWCNTs. Pyridinic N atoms jump across a monovacancy in graphene, and in a new dynamic, one Si and one N repeatedly switched their positions. Two kinds of P dynamics were observed: P were either replaced by C, or a C neighbor was knocked out thus changing their symmetry from three- to four-fold. We also observed several Ge atoms

being replaced by C or Si. In graphene, we saw further dynamics at Si sites such as Stone-Wales transformations at 55 kV due to a rotation of the next-nearest C-C bond. In SWCNTs, we also observed various configurations, such as a Stone-Wales defect near a Si site, three- to four-fold transformation of Si by knocking out a C neighbor, monovacancy creation due to ejection of Si, and frequent replacement of Si by C. In the next Section, we will discuss the purposeful manipulation of the impurities.

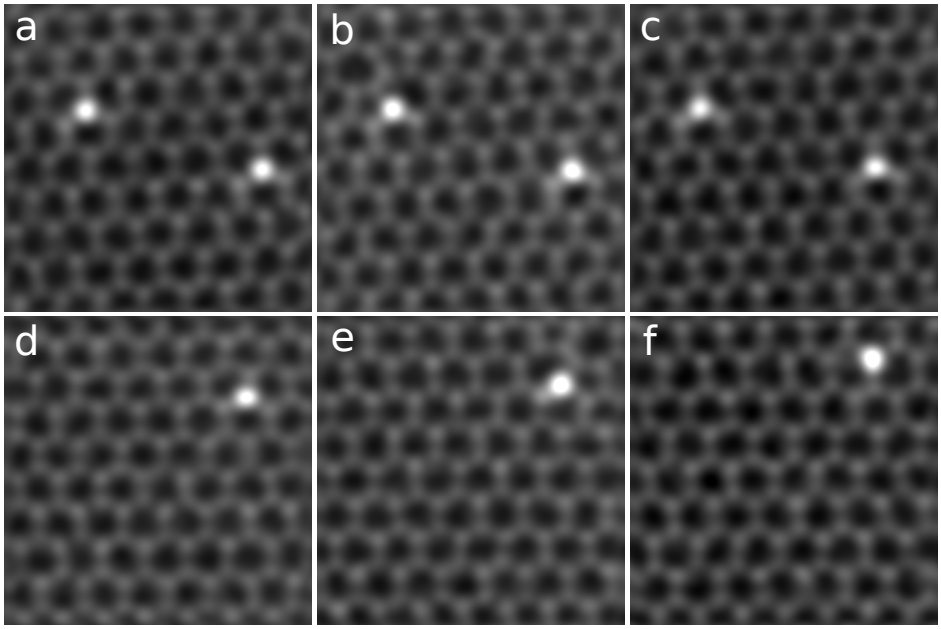

Figure 3.32: Stone-Wales dynamics and back-transformation near a Si site in graphene. Three consecutive STEM/MAADF double Gaussian filtered images of two different events captured at 55 kV.

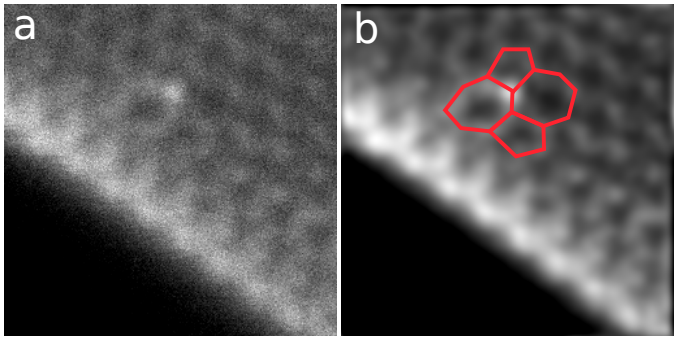

Figure 3.33: (a) STEM/MAADF image of a Stone-Wales defect with a Si atom in a SWCNT. (b) Double Gaussian filtered image with overlaid pentagons and heptagons.

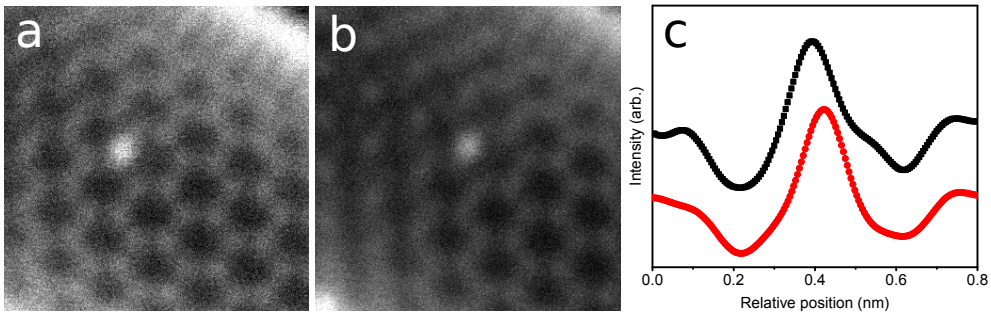

Figure 3.34: Three-to-fourfold conversion of Si in a SWCNT. (a) STEM/MAADF image shows that a Si is bonded with three C neighbors in three-coordinated configuration. (b) The impurity converts to four-coordinated due to an ejection of a C neighbor. (c) Line profiles. The dose per frame was 1.8×10^6 $e^-/Å^2$.

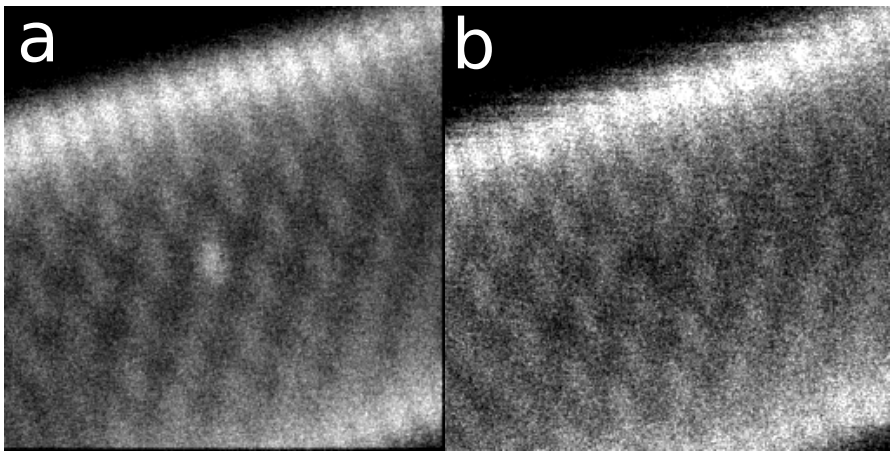

Figure 3.35: STEM/MAADF images showing the ejection of a Si leaving a monovacancy behind in a SWCNT. The dose per frame was 1.6×10^6 $e^-/Å^2$.

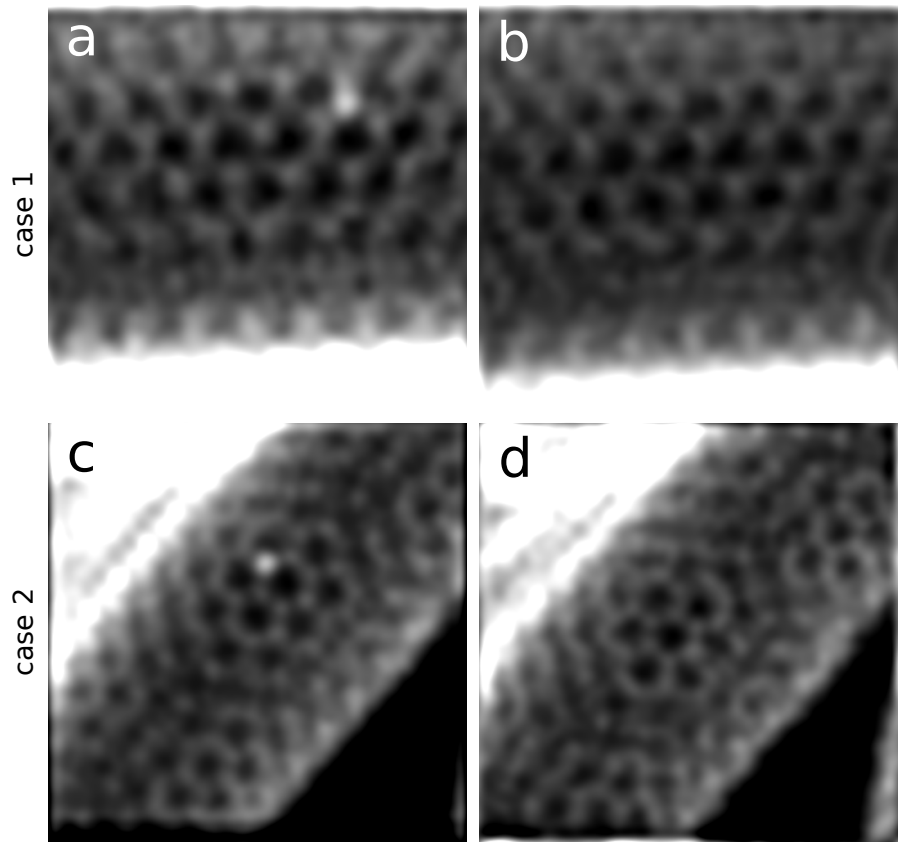

Figure 3.36: STEM/MAADF images showing the replacement of Si by C atoms in SWCNTs. Images have been processed using a double Gaussian filter. The dose per frame was 3.3×10^6 $e^-/Å^2$.

3.5 Electron-beam manipulation of impurities

This Section is dedicated to manipulating impurities using the electron beam in graphene and in single-walled carbon nanotubes. The content is based on entries 3 and 7 of the list of publications.

A main focus of this PhD thesis was the manipulation of heteroatoms, mainly silicon impurities in graphene and carbon nanotubes. In the previous Section, electron-beam induced dynamics at impurity sites were discussed. Importantly, the atomically focused probe in a STEM instrument allows us to place the beam on a single atom, directing their motion through the lattice in a fully controlled way. This has been used in earlier works to move Si atoms by a few sites in graphene [144, 154, 155]. However in those early works, the direction of Si atoms was not fully controlled due to some unintended double or triple jumps, most likely due to partly excessive dosing of the carbon atoms.

In contrast, we demonstrate here fully controlled manipulation of incidental Si impurities in monolayer graphene and Si atoms incorporated into SWCNTs through vacancy-assisted substitution [163]. We employed the Nion UltraSTEM100 for all the manipulation and imaging experiments at 55 & 60 keV primary beam energies. The beam current was 35 ± 10 pA which corresponds to a dose rate of (2.2 ± 0.6) × 10^8 e^-s^{-1} in the ∼1.1 Å diameter (full width at half maximum) probe.

3.5.1 Manipulation of impurities in graphene

To demonstrate the control we can achieve, we conducted various experiments to manipulate Si atoms over different paths at 55 and 60 kV. As a first step, after choosing a heteroatom, the Å-sized focused beam is targeted on top of one of its C neighbors for 10 s. After this selected irradiation time has passed, a new image is acquired. If the position of the heteroatom has changed, then the next C atom can be chosen. However, if the dopant site is unchanged due to drift or insufficient electron dose on the correct atom, the beam can be placed repetitively on the same C atom. Although this is a purely stochastic process, the atoms can be thus manipulated. We moved one Si over a path consisting of 34 lattice jumps precisely in the selected directions with no undesired motion or double jumps (Figure 3.37). However, we could not move the Si atom further beyond 34 jumps in this series due to the ejection of a C neighbor next to the Si thus changing the local symmetry from Si-C_3 to Si-C_4.

We further moved a Si around a graphene hexagon for a total of 75 jumps without changing its atomic configuration. Figure 3.39 shows selected STEM/MAADF images from the jumps series. In addition to the lateral path and the hexagon, individual Si atoms were moved repeatedly back and forth between the two graphene sublattices. Figure 3.38 presents selected STEM/MAADF images from a 67-jump series.

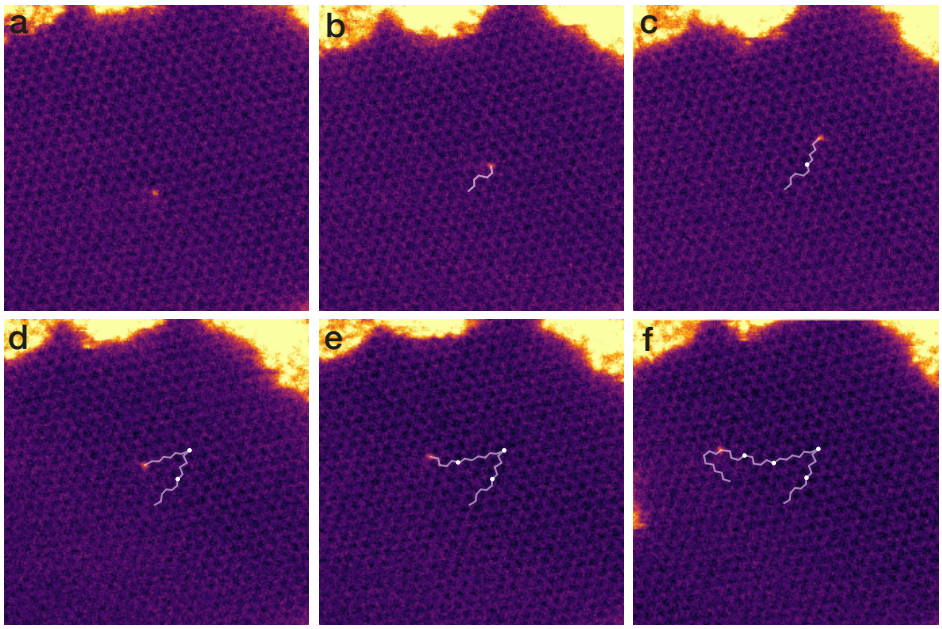

Figure 3.37: STEM/MAADF images show the controlled electron-beam manipulation of a Si heteroatom in graphene over an extended path at 60 kV. The images are overviews and the segmented line indicates each of the 34 precisely directed lattice jumps and dots the locations of the Si in each previous panel. The spot irradiation time was 10 s.

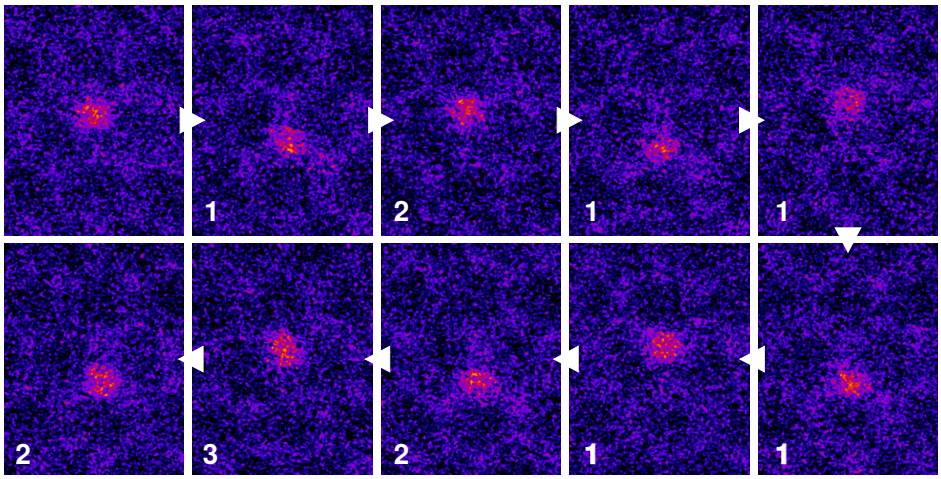

Figure 3.38: STEM/MAADF images showing electron-beam manipulation of Si in graphene from one sub-lattice to another at 60 kV acceleration voltage. The overlaid numbers show the number of 10 s spot irradiations for each jump.

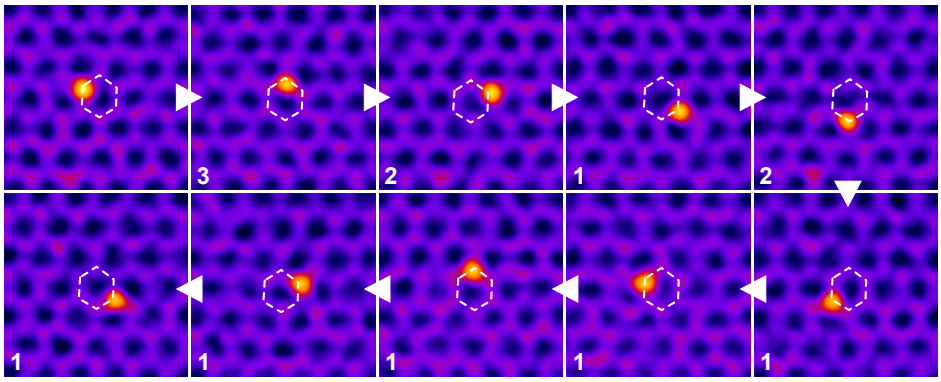

Figure 3.39: Double Gaussian filtered STEM/MAADF images show the electron-beam manipulation of a Si heteroatom along a single hexagon in graphene at 60 keV primary beam energy. Images are aligned to show the directed motion of Si and their order is given by the arrows. Overlaid are the number of 10 s spot irradiations for each jump.

We also conducted manipulation experiments at 55 kV and repeated the trajectories of Si atoms around a hexagon and between the two sublattices. A disadvantage of this manual method is excessive dosing of the C atom if its initial position already changed: we cannot see the change in the local structure in real time and can cause unintended or double lattice site jumps. The beam may also knock out the C atom next to the dopant site, subsequently changing their bonding from threefold-to-fourfold configuration, which is not amenable for manipulation [115].

As a first step towards automation and to avoid excessive or unintended dosing due to drift, we implemented real-time feedback by connecting a Keithley 2000 multimeter to the MAADF detector, reading out the scattering signal (raw detector voltage) averaged over 150 ms while the beam was parked on the desired C atom. These values were read into the Nion Swift microscope control software and used to trigger the acquisition of new frames. As control logic, an increased intensity corresponds to a successful manipulation (Si has taken the place of the C, leading to greater scattering), with a threshold of 10% change with respect to the cumulative average of the signal chosen as the trigger condition (Figure 3.40). The spot irradiation can now be stopped automatically when the intensity changes.

At 55 kV, due to the feedback we were also able to obtain more accurate timing for each jump, and observed only few double site jumps in these series of experiments [161]. An example of Si manipulation around a graphene hexagon is shown in Figure 3.41. The overlaid inset numbers indicate the actual time of spot irradiation between the frames for each jump. At 55 kV, we observed only one event of knock-on damage with an apparent rate of 0.0040 ± 0.0007 min^{-1} (corresponding to $(8.9 \pm 1.5) \times 10^{11}$ e^{-}).

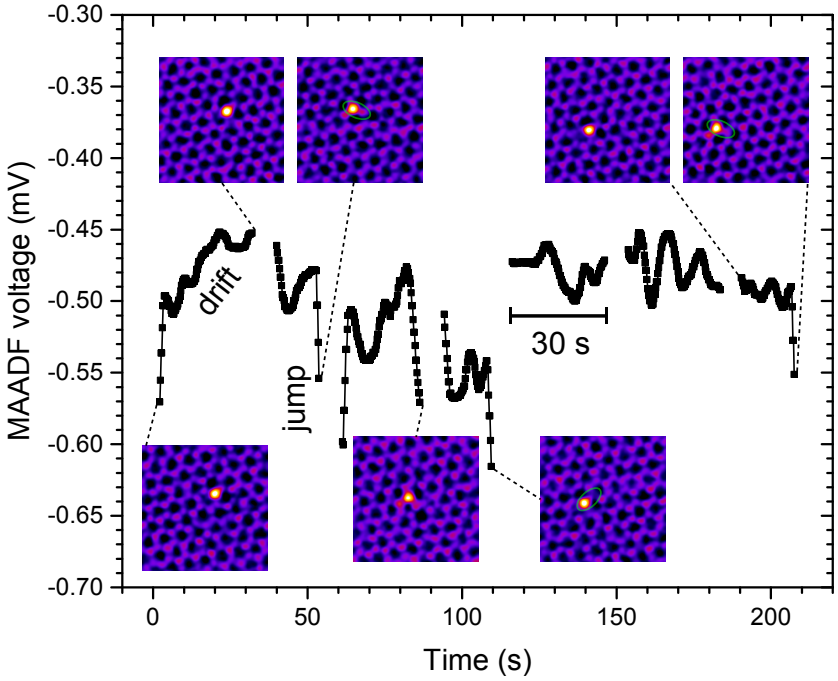

Figure 3.40: MAADF detector voltage read by a multimeter, averaged over 150 ms and used to trigger the acquisition of new image frames. Jumps are detected as change in the voltage corresponding to greater scattering intensity due to the Si atom jumping under the beam, whereas gradual drift was accounted for by a 30 s timeout if no jump has been detected. The double Gaussian filtered [35] MAADF images are acquired between the feedback periods, with overlaid green ovals highlighting the Si jumps. Image is reused with permission from Ref. [161] (CC-BY).

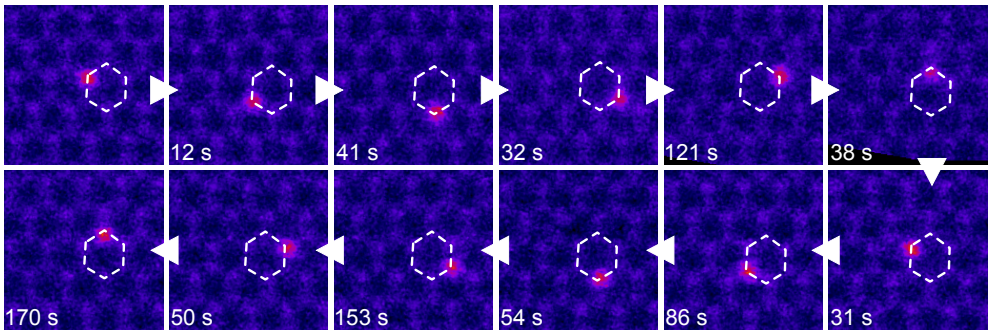

Figure 3.41: Consecutive STEM/MAADF images showing Si manipulation around a graphene hexagon at 55 kV. The inset numbers indicate the actual time of spot irradiation between the frames.

A stacked histogram of all 60 kV manipulation events (Figure 3.42b) shows that in most cases (136/164 = 0.83), the required irradiation time is 20 s or less (the geometric mean of 15.1 s providing a good estimate for the Poisson expectation value [115]), corresponding to a dose of $(8.9 \pm 0.9) \times 10^8$ electrons per event and a rate close to four jumps per minute (discarding the frame time of 4.2 s). Remarkably, despite the simplicity of the experimental procedure this is nearly on par with the state-of-the-art in automated STM-based single-atom manipulation [110]. In total, at 55 kV we moved individual Si impurities 102 times with an average rate or 0.73 ± 0.16 jumps per minute, corresponding to an average irradiation dose per event of $(8.8 \pm 1.0) \times 10^9$ e^-.

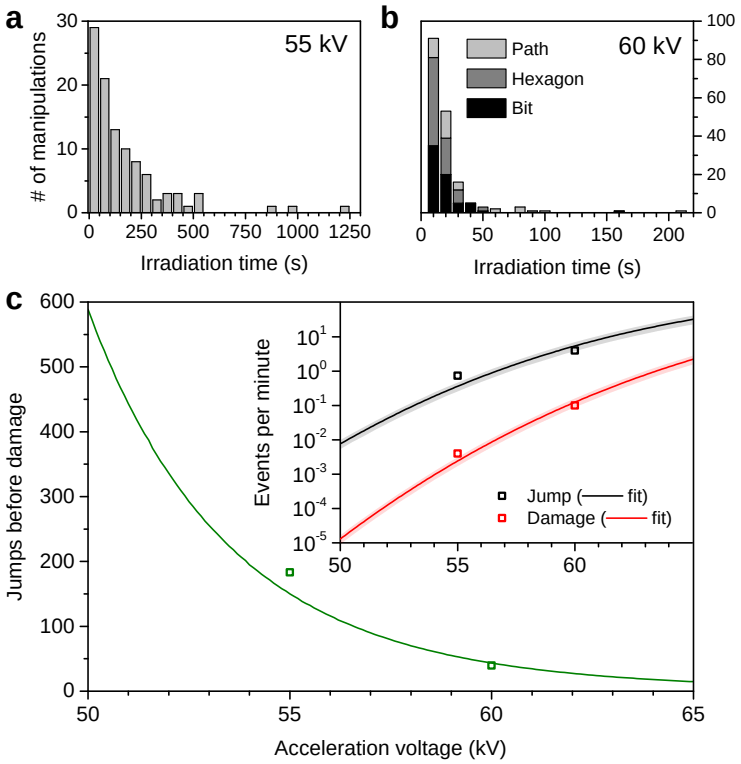

Figure 3.42: Histogram of spot irradiation times for each manipulation event at 55 kV (a) and 10 s spot irradiations at 60 kV (b). Theoretically predicted rates of manipulation events (jumps) and knock-on damage, as well as the predicted number of successful manipulations before damage for electron acceleration voltages close to 60 kV and for a realistic beam shape with a current of 35 ± 10 pA are shown in (c). The open squares correspond to our spot irradiation experiments, the solid lines to a theoretical model [107] with best-fit event threshold energies and shaded areas to error estimates based on the uncertainty of the irradiation dose. Image is reused with permission from Ref. [161] (CC-BY).

The manipulation rate could be increased by increasing the electron acceleration voltage but this would also increase the probability of knock-on damage. On the other hand, a lower voltage would decrease the manipulation rate, but also decrease the probability of damage as shown in Figure 3.42c. Because of their differing threshold energies, the damage probability decreases more than the probability of a jump as a function of electron energy, which means that the statistically expected number of successful jumps can be increased by lowering the voltage. Improving the sharpness of the electron probe would be clearly beneficial; for our expected probe shape [36] we estimate that only 26% of the dose impinges on the area of the targeted C atom. Thus, a sharper probe would allow us to increase the manipulation rate without impacting the relative probability of damage.

In addition to the manipulation of single atoms, two Si were brought closer to each other at 60 kV, ending up as next-nearest neighbors separated by only a single C atom in the graphene lattice as presented in the filtered STEM/MAADF images in Figure 3.44. It was not clear how stable multiple Si atoms within a single hexagon are. Theoretically, it was estimated that the energy of the system goes down when two Si atoms are brought closer together up to next nearest neighbour in the lattice [115]. However, in the last frame of the series, one Si atom was apparently replaced by a C atom in one of the only instances of this process that we observed in graphene (Figure 3.44f).

To further explore the limits of heteroatom manipulation in graphene, we attempted to manipulate three-coordinated P impurities in a similar way to the Si. Figure 3.43 shows the only two successful outcomes of P manipulation. The brighter atom in all panels is P and the green marked circle on a C neighbor shows the position where the electron probe was intentionally placed to move it. Similar to Si manipulation, the spot irradiation time was 10 s for all the attempts, and after each spot irradiation, a new frame was acquired. In the first case, the P moved by one lattice site after 68 ineffective 10 s spot irradiations and in the second one, it jumped one lattice site after 12 spot irradiations. The experimentally estimated cross section for this process was 0.05 ± 0.02 barn. P atoms are much thus harder to manipulate in graphene and further hampered by the high probability of C replacement, whereas Si in the same conditions can be easily moved over many sites as presented earlier.

Similar to the electron-beam manipulation of Si and P impurities, we further attempted to move Ge by iteratively placing the electron probe on one C neighbor for 10 s between acquiring images. In total, 24 such irradiations were attempted on several different Ge impurities, without success. The bond-inversion mechanism for Ge and C seems to not work due to the greater mass of Ge: during the out-of-plane trajectory of the ejecting C atom, the Ge does not move sufficiently fast to relax into the resulting vacancy. As a result, the C atom cannot pass onto the other side of the impurity, and thus the Ge does not move in the lattice [47].

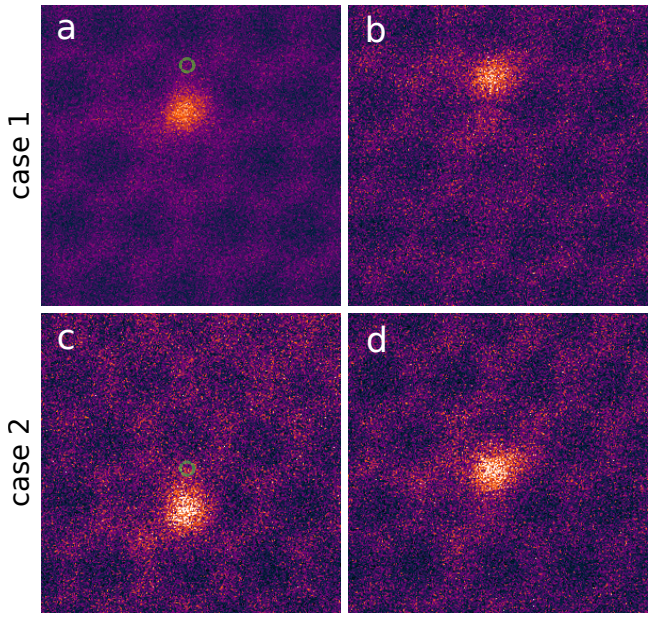

Figure 3.43: STEM/MAADF images showing two cases of controlled manipulation of P in graphene. A green marked circle on the C neighbor shows the position where the electron probe was placed to purposefully move the P atom by one lattice site (a & c). The P jumped by one lattice site after many 10 s spot irradiations (b & d).

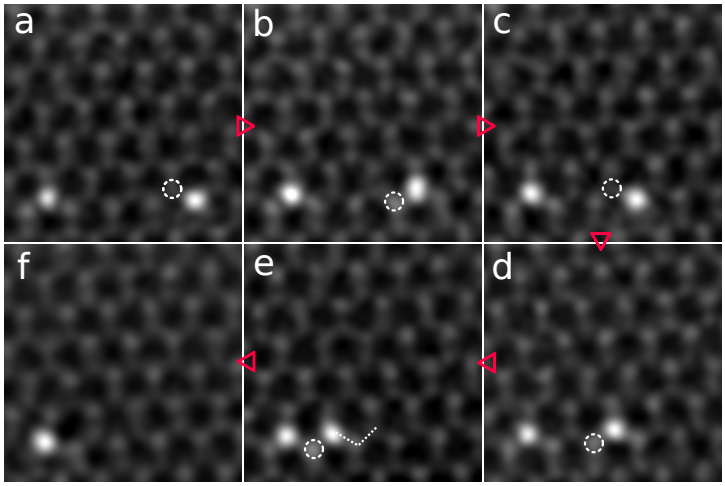

Figure 3.44: STEM/MAADF images of two Si dopants brought towards each other in graphene, separated by only one C atom in the end. In the last frame one Si has been replaced by C. The dashed circle shows the electron probe position. The dotted line indicates a double site jump.

3.5.2 Manipulation of Si in SWCNTs

Very recently, we also manipulated Si impurities in SWCNTs using the same method. Si can be incorporated in the SWCNT lattice using post-synthesis doping methods, in our case plasma irradiation [163]; the sample synthesis process was briefly described in Section 2.5.2. In our experiments, we first found suitable Si sites in large-diameter tubes with low chiral angle. To move the Si, again a focused electron probe can be used to irradiate a carbon neighbor, repeated iteratively, and an image recorded after each spot irradiation.

We again used two primary beam energies, 55 and 60 keV. At 55 keV, the spot irradiation time was 10 s whereas at 60 keV we reduced it to 7 s. Figure 3.45 presents STEM/MAADF images from a manipulation series of a Si atom at 60 keV in an armchair tube with a diameter of ∼2.75 nm. The trajectory of the atom is shown along the tube axis in Figure 3.45b. Since we did not use real-time feedback here, we did observe some double and one triple jump. Nonetheless, we were able to move the Si through a total of 30 sites along the zigzag lattice direction.

Another example of Si manipulation in a SWCNT is shown in Figure 3.46. The Si atom was moved repeatedly back and forth from one sublattice to the other in a controlled way, now along the armchair direction perpendicular to the tube axis. This tube diameter is nearly the same as for the previous case but with a small chiral angle near the armchair configuration.

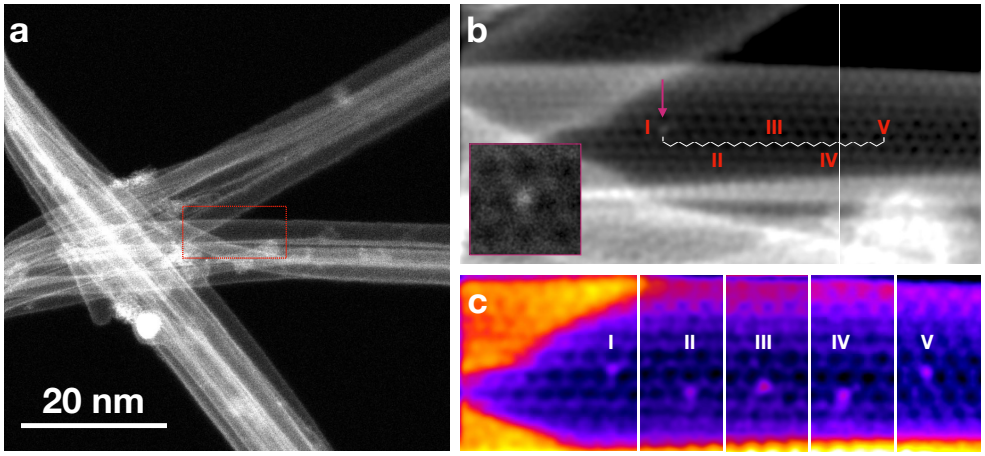

Figure 3.45: STEM/MAADF images showing controlled electron-beam manipulation of a Si atom in a single-walled carbon nanotube, at 60 kV acceleration voltage and a spot irradiation time of 7 s. (a) Overview of the SWCNT where the highlighted rectangle shows the region of interest. (b) Path of directed lattice jumps of the Si along the tube axis in the zigzag direction. (c) The intermediate frames are aligned and positioned as marked by I-V in (b).

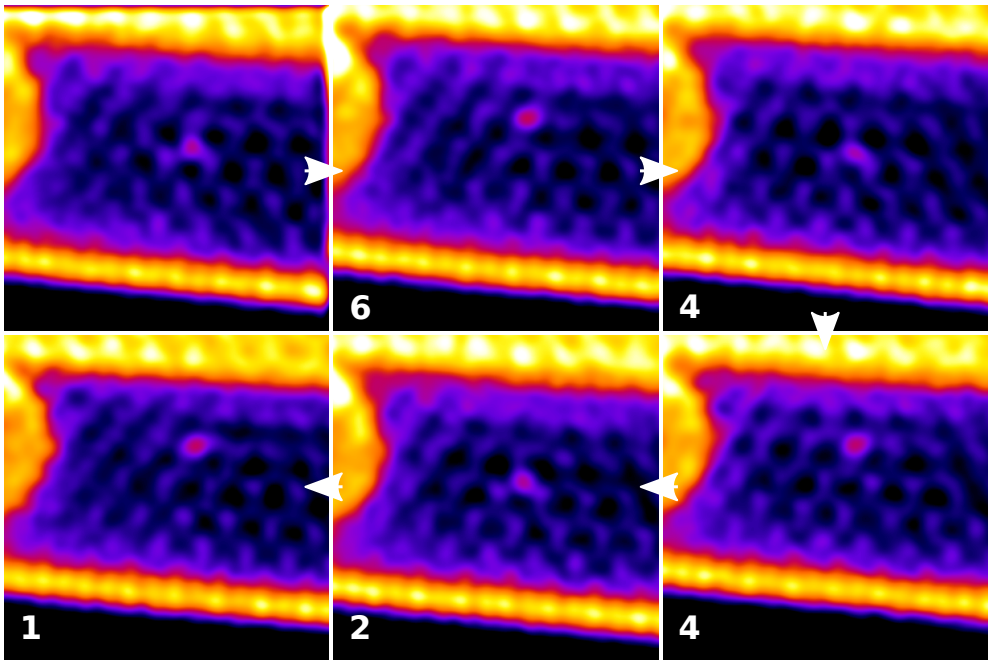

Figure 3.46: STEM/MAADF images showing the manipulation of Si back and forth between two sublattices in the armchair direction in a SWCNT at 55 kV acceleration voltage with a spot irradiation time of 10 s.

To estimate the probability of triggering jumps in SWCNTs, we estimated the distribution of doses per event (taking into account that only 26% of the total beam current impinges on the target atom [161] as calculated for our expected probe shape [36]) and approximated the underlying Poisson expectation value by their geometric mean [115]. The electron dose required to trigger a jump at 55 kV was $(1.98\pm0.13)\times10^9$ e^- (N=24) in the zigzag and $(2.51\pm0.33)\times10^9$ e^- (N=13) in the armchair direction (geometric mean $\pm$ standard error), with corresponding values at 60 kV being 5.58×10^8 e^- (N=2) and $(5.60\pm0.20)\times10^8$ e^- (N=54). These result in cross sections of 0.132 $\pm$ 0.004 barn in the zigzag direction and 0.104 $\pm$ 0.006 barn in the armchair one at 55 kV whereas at 60 kV, they are 0.469 $\pm$ 0.008 barn in the zigzag direction and 0.468 $\pm$ 0.002 barn in the armchair one. Within these limited statistics, the two directions thus appear identical in these large-diameter tubes.

These are slightly higher than the values measured for graphene (0.03 barn at 55 kV and 0.29 barn at 60 kV [161]), reflecting the slightly curved geometry of even large-diameter SWCNTs. Additionally, manipulation was successful only for half of the found impurity atoms. Simulations revealed that the successful bond inversion can be achieved only when the Si atom is in the "back wall" of the tube and thus facing away from the electron beam [164] explain-

ing the ∼50 % success rate. In the case of SWCNTs, curvature, diameter and chiral angle further play an important role. For example, the chiral angle determines the direction in which the bonds around the Si site are bent, introducing asymmetry. Also, the energy required to trigger a jump (or to knock out a C) can be lower than in graphene. For our smallest diameter tube (∼1.5 nm), we observed only a single jump followed by Si atom ejection.

In summary, we have shown how targeted electron irradiation with an Å-sized electron probe can reliably move individual Si impurities through the graphene and carbon nanotube lattices, and the possibility of electron-beam manipulation of P. Manipulation of P atoms is difficult in comparison to Si, whereas Ge appear too heavy to be manipulated. In the case of nanotubes, the curvature affects the threshold energies for smaller diameter tubes [164] and the orientation of the silicon atomic site with respect to the beam direction also plays an important role: only impurities along the axis can be easily visualized, and only those incorporated into the wall facing away from the beam can be moved by the beam. Although all atoms in graphene or in SWCNTs are surface atoms, their impurities are much stronger bound than the surface adatoms or vacancies that can be manipulated with scanning probe techniques, resulting in inherent temperature stability. Electron-beam induced dynamics and the manipulation of impurities is further not only limited to low-dimensional materials but also recently extended to three-dimensional crystals [165]. Ultimately, there is potential to scale-up the use of atomically precision manipulation and to fabricate nanostructures from multiple impurity atoms in STEM.

Chapter 4

Summary

In summary, this thesis demonstrates several ways to defect-engineer low-dimensional materials using ion and electron beams. Clean samples are an essential requirement for any state-of-the-art experiments. Cleaning of low-dimensional materials was demonstrated via radiative or laser-induced heating in the same vacuum system as the scanning transmission electron microscope (STEM). Using this *pre-situ* cleaning, large atomically clean areas can be easily obtained especially in graphene.

Atomic resolution STEM imaging revealed intrinsically present nanopores along the grain boundaries (GBs) of chemical vapor deposition (CVD) grown MoS_2. An analysis of pore areas showed their grain-misorientation dependent size distribution: areas decrease until 15° misorientation angle and then increase again for higher angles until 30°. The distance between dislocation cores decreases exponentially with the increase in relative mismatch angle of the GBs, in agreement with the Frank-Bilby equation.

The structure of freestanding mono- and bilayers of MoS_2 and WS_2 can be permanently modified using highly charged ions. After Xe ion irradiation, roundish pores were formed in MoS_2, while triangular pores with sharp edges were found in WS_2. The pore size distributions shows that the radius of these pores can be controlled by the ion charge state. The pore creation efficiency from each individual ion also decreases with their decreasing potential energy. This effective technique presents an unique approach to create pores of a suitable size in transition metal dichalcogenides.

Ion implantation of germanium impurities into graphene has been shown. Ge is significantly larger in size than carbon, yet atomic resolution STEM imaging demonstrated the direct substitution of a single C atom, bonding to three neighbors. Although ion implantation continues to progress as a versatile tool for precise doping, achieving high-quality clean sample and high efficiency of implantation still remains a challenge.

Aberration-corrected STEM revealed the electron-beam induced dynamics of individual impurity atoms including nitrogen, silicon, phosphorous and

germanium in graphene, and silicon in single-walled carbon nanotubes (SWCNTs). A better understanding of the dynamics of heteroatoms can help to scale up the fabrication of nanostructures from multiple atoms in the STEM.

Finally, we have pushed forward the emerging field of single-atom manipulation by using STEM to manipulate Si and P impurity atoms in graphene. The manipulation of Si has also been extended to one-dimensional SWCNTs. We found that P atoms are much harder than Si to manipulate. In the case of SWCNTs, the orientation of the Si site with respect to the beam direction plays an important role: only impurities along the axis can be easily visualized, and only those incorporated into the wall facing away from the beam can be moved by the beam.

The level of control and the manipulation rate is already on par with the state-of-the-art in other atom manipulation techniques such as scanning probe microscopy. After the density of Si atoms is increased by post-synthesis doping techniques such as ion implantation or plasma irradiation, aberration-corrected STEM can be used as an efficient tool to fabricate extended nanostructures in graphene or in SWCNTs using arrangements of several Si atoms. In the future, instrumental advances in beam shaping combined with a carefully chosen acceleration voltage as well as optimization of direct feedback and the implementation of drift compensation will enhance our capabilities further, to be followed by structure recognition and software-controlled beam repositioning as the next steps toward full automation.

List of publications

Published:

1. **Cleaning graphene: Comparing heat treatments in air and in vacuum**

   Mukesh Tripathi, Andreas Mittelberger, Kimmo Mustonen, Clemens Mangler, Jani Kotakoski, Jannik C. Meyer and Toma Susi

   physica status solidi (RRL)- Rapid Research Letters, 11,1700124 (2017)

   Author contributions: M.T., A.M., K.M, and C.M carried out experiments. **M.T.** and T.S. analyzed the data. **M.T.** and T.S. wrote the paper and all authors participated in its revision. J.C.M., J.K and T.S. supervised the work.

2. **Implanting Germanium into Graphene**

   Mukesh Tripathi, Alexander Markevich, Roman Bttger, Stefan Facsko, Elena Besley, Jani Kotakoski and Toma Susi

   ACS Nano, 12, 4641-4647 (2018)

   Author contributions: M.T. carried out the sample preparation, STEM experiments and their analysis, and wrote the paper. **M.T.**, T.S., and R.B. participated in ion implantation experiments. A.M. performed DFT/MD simulations. T.S. carried out QSTEM simulations. S.F., E.B. and T.S. supervised the study. All authors participated in the revision of the manuscript.

3. **Electron-Beam Manipulation of Silicon Dopants in Graphene**
   Mukesh Tripathi, Andreas Mittelberger, Nicholas A. Pike, Clemens

   Mangler, Jannik C. Meyer, Matthieu J. Verstraete, Jani Kotakoski and Toma Susi

   Nano Letters, 18, 5319-5323 (2018)

   Author contributions: M.T. and T.S. carried out the scanning transmission electron microscopy experiment. A.M. and C.M. participated in EELS and feedback implementation. **M.T.** prepared the samples and analyzed the data. N.A.P and M.J.V. calculated the phonon dispersion, density of states and the velocities of atoms. T.S. performed the DFT/MD simulations and supervised the project. **M.T.** and T.S. drafted the manuscript and all authors participated in its revision.

4. **Intrinsic Core Level Photoemission of Suspended Monolayer Graphene**

   Toma Susi, Mattia Scardamaglia, Kimmo Mustonen, **Mukesh Tripathi**, Andreas Mittelberger, Mohamed Al-Hada, Matteo Amati, Hikmet Sezen, Patrick Zeller, Ask H. Larsen, Clemens Mangler, Jannik C. Meyer, Luka Gregoratti, Carla Bittencourt and Jani Kotakoski

   Physical Review Materials, 2, 074005 (2018)

   Author contributions: T.S., **M.T.**, A.M. and C.M. carried out the scanning transmission electron microscopy experiments. K.M. performed Raman spectroscopy measurements. **M.T.** prepared the samples. M.S., M.A.H., M.A., H.S., P.Z., A.H.L participated in X-ray photoelectron spectroscopy and scanning photoelectron microscopy experiments and analysis. T.S. performed the binding energy simulations. T.S., L.G., C.B. and J.K. supervised the project. T.S. drafted the manuscript and all authors participated in its revision.

5. **Perforating freestanding molybdenum disulfide monolayers with highly charged ions**

   Roland Kozubek, **Mukesh Tripathi**, Mahdi Ghorbani-Asl, Silvan Kretschmer, Lukas Madau, Maria O' Brien, Niall McEvoy, Ursula Ludacka, Toma Susi, Georg S. Duesberg, Richard A. Wilhelm, Arkady V. Krasheninnikov, Jani Kotakoski and Marika Schleberger

   The Journal of Physical Chemistry Letters, 0, 904-910, 10 (2019)

   Author contributions: M.O-B., N.M., L.M. and G.S.D. synthesized the monolayer molybdenum disulfide samples. R.K., L.M. and **M.T.** prepared the freestanding TEM samples. R.K. and L.M. performed highly charged ions irradiation experiments. **M.T.**, U.L., T.S. and J.K. participated in electron microscopy experiments. R.K., L.M. and **M.T.** analyzed the data. M.G-A. and S.K. performed the simulations. R.A.W., A.V.K., J.K. and M.S. supervised the project. R.K. drafted the manuscript and all authors participated in its revision.

To be published:

6. **Engineering single-atom dynamics with electron irradiation**

   Cong Su, **Mukesh Tripathi**, Qing-Bo Yan, Zegao Wang, Zihan Zhang, Christoph Hofer, Haozhe Wang, Leonardo Basile, Gang Su, Mingdong Dong, Jannik C. Meyer, Jani Kotakoski, Jing Kong, Juan-Carlos Idrobo, Toma Susi, and Ju Li

   Science Advances, XX, XXXXX (2019)

Author contributions: C.S., T.S. and J.L. conceived the idea. J.-C.I., C.S., **M.T.**, C.H., and T.S. carried out the electron microscopy experiments. Z.W. synthesized the doped graphene. C.S., H.W., C.H. and **M.T.** prepared the TEM samples. C.S. performed the ab-initio MD calculations. Q.-B.Y., Z.Z., and T.S. performed cNEB calculations. C.S., **M.T.**, and C.H. performed the beam dose analysis for each event. C.S. wrote the Matlab code for visualizing the PKS and calculating the cross sections. L.B. performed the STEM image simulation. C.S. performed the EELS simulation. J.L., T.S., J.-C.I. and J.K. supervised the project. C.S. and T.S. drafted the manuscript and all authors participated in its revision.

7. **Silicon Substitution in Nanotubes and Graphene via Intermittent Vacancies**

   Heena Inani, Kimmo Mustonen, Alexander Markevich, Er-Xiong Ding, **Mukesh Tripathi**, Aqeel Hussain, Clemens Mangler, Esko I. Kauppinen, Toma Susi, and Jani Kotakoski

   Author contributions: H.I. and K.M. carried out the scanning transmission electron microscopy experiment. H.I. analyzed the data. C.M. participated in EELS measurements. A.H. and E-X. D. prepared the samples. **M.T.**, K.M. and H.I. carried out the plasma irradiation experiment. A.M. performed the DFT/MD simulations. E.I.K. and J.K. supervised the project. K.M. and H.I. drafted the manuscript and all authors participated in its revision.

8. **Electron-Beam Manipulation of Silicon Impurities in Single-Walled Carbon Nanotubes**

   Kimmo Mustonen, Alexander Markevich, **Mukesh Tripathi**, Heena Inani, Aqeel Hussain, Er-Xiong Ding, Clemens Mangler, Esko I. Kauppinen, Jani Kotakoski, and Toma Susi

   Author contributions: K.M. and **M.T.** carried out the scanning transmission electron microscopy experiment. **M.T.** analyzed the data. C.M. participated in EELS measurements. A.H. and E-X. D. prepared the samples. K.M. and H.I. carried out the plasma irradiation experiment. A.M. performed the DFT/MD simulations. E.I.K. and T.S. supervised the project. K.M., **M.T.**, A.M. and T.S. drafted the manuscript and all authors participated in its revision.

In preparation:

- A novel platinum nanowire electrocatalyst on single-walled carbon nanotubes to drive hydrogen evolution

- Misorientation-angle dependent grain boundary pores in MoS_2

Seminar presentations:

- October 12, 2018. Seminar "Micro- and Nanomaterials", Vienna: "Modification of low-dimensional materials using energetic charged particles"

- February 20, 2019. Highlight Lecture at the Faculty Open Presentations, Vienna: "Modifying low-dimensional materials using energetic charged particles"

Contributions to scientific events

Participation in international conferences

Date & Venue	**Conference**	**Type**	**Title of contribution**
Aug 7-13, 2016 Vienna, Austria	NT16 Science and Applications of Nanotubes and low-dimensional Materials	Poster	Spray-coated carbon nanotube film for NH_3 gas sensing
Sep 19-22, 2016 Warsaw, Poland	European Materials Reseach Society (EMRS) fall meeting	Poster	STEM analysis of pores in MoS_2 irradiated with highly charged ions
Mar 04-11, 2017 Kirchberg, Austria	XXXIst Int. Winterschool on Electronic Properties of Novel Materials (IWEPNM)	Poster	Scanning transmission electron microscopy of nanopores in irradiated MoS_2
Sep 25-29, 2017 Athens, Greece	Graphene Week	Poster	Cleaning graphene: comparing heat treatments in air and in vacuum
Oct 11-13, 2017 Indore, India	4^{th} Int. Conference on Nano Structuring by Ion Beam (ICNIB)	Oral	Ion beam modifications of MoS_2 and graphene
Jul 9-13, 2018 Trieste, Italy	Conference on Physics of Defects in Solids: Quantum Mechanics Meets Topology	Oral	Atomic Precision Manipulation and Implantation of Graphene Heteroatoms
Aug 27-29, 2018 Belgrade, Serbia	Electron Microscopy of Nanostructures (ELMINA2018)	Poster	Ion Implantation and Electron-Beam Modifications of Graphene
Sep 10-14, 2018 San Sebastian, Spain	Graphene Week	Poster	Ion Implantation and Electron-Beam Modifications of Graphene

Bibliography

[1] Peierls, "Quelques propriétés typiques des corps solides," *Annales de l'institut Henri Poincaré*, vol. 5, no. 3, pp. 177–222, 1935.

[2] L. D. Landau, "Zur Theorie der phasenumwandlungen II," *Phys. Z. Sowjetunion*, vol. 11, pp. 26–35, 1937.

[3] P. R. Wallace, "The Band Theory of Graphite," *Phys. Rev.*, vol. 71, no. 9, p. 622, 1947.

[4] K. S. Novoselov, A. K. Geim, S. V. Morozov, D. Jiang, Y. Zhang, S. V. Dubonos, I. V. Grigorieva, and A. A. Firsov, "Electric Field Effect in Atomically Thin Carbon Films," *Science*, vol. 306, no. 5696, pp. 666–669, 2004.

[5] A. H. Castro Neto, F. Guinea, N. M. R. Peres, K. S. Novoselov, and A. K. Geim, "The electronic properties of graphene," *Rev. Mod. Phys.*, vol. 81, no. 1, pp. 109–162, 2009.

[6] A. K. Geim and K. S. Novoselov, "The rise of graphene," *Nat. Mater.*, vol. 6, no. 3, pp. 183–191, 2007.

[7] K. S. Novoselov, A. K. Geim, S. V. Morozov, D. Jiang, M. I. Katsnelson, I. V. Grigorieva, S. V. Dubonos, and A. A. Firsov, "Two-dimensional gas of massless {D}irac fermions in graphene," *Nature*, vol. 438, no. 7065, pp. 197–200, 2005.

[8] K. I. Bolotin, K. J. Sikes, Z. Jiang, M. Klima, G. Fudenberg, J. Hone, P. Kim, and H. L. Stormer, "Ultrahigh electron mobility in suspended graphene," *Solid State Communications*, vol. 146, no. 9, pp. 351–355, 2008.

[9] A. A. Balandin, S. Ghosh, W. Bao, I. Calizo, D. Teweldebrhan, F. Miao, and C. N. Lau, "Superior Thermal Conductivity of Single-Layer Graphene," *Nano Letters*, vol. 8, no. 3, pp. 902–907, 2008.

[10] C. Lee, X. Wei, J. W. Kysar, and J. Hone, "Measurement of the Elastic Properties and Intrinsic Strength of Monolayer Graphene," *Science*, vol. 321, no. 5887, pp. 385–388, 2008.

[11] S. Bae, H. Kim, Y. Lee, X. Xu, J.-S. Park, Y. Zheng, J. Balakrishnan, T. Lei, H. Ri Kim, Y. I. Song, Y.-J. Kim, K. S. Kim, B. Özyilmaz, J.-H. Ahn, B. H. Hong, and S. Iijima, "Roll-to-roll production of 30-inch graphene films for transparent electrodes," *Nature Nanotechnology*, vol. 5, p. 574, 2010.

[12] F. Bonaccorso, Z. Sun, T. Hasan, and A. C. Ferrari, "Graphene photonics and optoelectronics," *Nat Photon*, vol. 4, no. 9, pp. 611–622, 2010.

[13] R. S. Pantelic, J. C. Meyer, U. Kaiser, and H. Stahlberg, "The application of graphene as a sample support in transmission electron microscopy," *Solid State Communications*, vol. 152, no. 15, pp. 1375–1382, 2012.

[14] R. R. Nair, P. Blake, A. N. Grigorenko, K. S. Novoselov, T. J. Booth, T. Stauber, N. M. R. Peres, and A. K. Geim, "Fine Structure Constant Defines Visual Transparency of Graphene," *Science*, vol. 320, no. 5881, p. 1308, 2008.

[15] S. Iijima, "Helical microtubules of graphitic carbon," *Nature*, vol. 354, p. 56, 1991.

[16] S. Iijima and T. Ichihashi, "Single-shell carbon nanotubes of 1-nm diameter," *Nature*, vol. 363, p. 603, 1993.

[17] M.S.˜Dresselhaus, G.˜Dresselhaus, and P.˜Avouris,

[18] A. Splendiani, L. Sun, Y. Zhang, T. Li, J. Kim, C.-Y. Chim, G. Galli, and F. Wang, "Emerging Photoluminescence in Monolayer MoS2," *Nano Letters*, vol. 10, no. 4, pp. 1271–1275, 2010.

[19] K. F. Mak, C. Lee, J. Hone, J. Shan, and T. F. Heinz, "Atomically Thin MoS2: A New Direct-Gap Semiconductor," *Phys. Rev. Lett.*, vol. 105, no. 13, p. 136805, 2010.

[20] D. Sarkar, W. Liu, X. Xie, A. C. Anselmo, S. Mitragotri, and K. Banerjee, "MoS2 Field-Effect Transistor for Next-Generation Label-Free Biosensors," *ACS Nano*, vol. 8, no. 4, pp. 3992–4003, 2014.

[21] B. Radisavljevic, A. Radenovic, J. Brivio, V. Giacometti, and A. Kis, "Single-layer MoS2 transistors," *Nature Nanotechnology*, vol. 6, p. 147, 2011.

[22] H. R. Gutiérrez, N. Perea-López, A. L. Elías, A. Berkdemir, B. Wang, R. Lv, F. López-Urías, V. H. Crespi, H. Terrones, and M. Terrones, "Extraordinary Room-Temperature Photoluminescence in Triangular WS2 Monolayers," *Nano Letters*, vol. 13, no. 8, pp. 3447–3454, 2013.

[23] W. Zhao, Z. Ghorannevis, L. Chu, M. Toh, C. Kloc, P.-H. Tan, and G. Eda, "Evolution of Electronic Structure in Atomically Thin Sheets of WS2 and WSe2," *ACS Nano*, vol. 7, no. 1, pp. 791–797, 2013.

[24] A. Kuc and T. Heine, "On the Stability and Electronic Structure of Transition-Metal Dichalcogenide Monolayer Alloys Mo1xXxS2ySey with X = W, Nb," *Electronics*, vol. 5, no. 1, 2016.

[25] K. S. Novoselov, D. Jiang, F. Schedin, T. J. Booth, V. V. Khotkevich, S. V. Morozov, and A. K. Geim, "Two-dimensional atomic crystals," *Proceedings of the National Academy of Sciences of the United States of America*, vol. 102, no. 30, pp. 10 451 LP – 10 453, 2005.

[26] M. O'Brien, N. McEvoy, T. Hallam, H.-Y. Kim, N. C. Berner, D. Hanlon, K. Lee, J. N. Coleman, and G. S. Duesberg, "Transition Metal Dichalcogenide Growth via Close Proximity Precursor Supply," *Scientific Reports*, vol. 4, p. 7374, 2014.

[27] S. J. Yun, S. H. Chae, H. Kim, J. C. Park, J.-H. Park, G. H. Han, J. S. Lee, S. M. Kim, H. M. Oh, J. Seok, M. S. Jeong, K. K. Kim, and Y. H. Lee, "Synthesis of Centimeter-Scale Monolayer Tungsten Disulfide Film on Gold Foils," *ACS Nano*, vol. 9, no. 5, pp. 5510–5519, 2015.

[28] F. Banhart, J. Kotakoski, and A. V. Krasheninnikov, "Structural Defects in Graphene," *ACS Nano*, vol. 5, no. 1, pp. 26–41, 2011.

[29] J. Kotakoski, A. V. Krasheninnikov, U. Kaiser, and J. C. Meyer, "From Point Defects in Graphene to Two-Dimensional Amorphous Carbon," *Phys. Rev. Lett.*, vol. 106, no. 10, p. 105505, 2011.

[30] O. Lehtinen, J. Kotakoski, A. V. Krasheninnikov, A. Tolvanen, K. Nordlund, and J. Keinonen, "Effects of ion bombardment on a two-dimensional target: Atomistic simulations of graphene irradiation," *Phys. Rev. B*, vol. 81, no. 15, p. 153401, 2010.

[31] H.-P. Komsa, J. Kotakoski, S. Kurasch, O. Lehtinen, U. Kaiser, and A. V. Krasheninnikov, "Two-Dimensional Transition Metal Dichalcogenides under Electron Irradiation: Defect Production and Doping," *Phys. Rev. Lett.*, vol. 109, no. 3, p. 35503, 2012.

[32] J. Kotakoski, J. C. Meyer, S. Kurasch, D. Santos-Cottin, U. Kaiser, and A. V. Krasheninnikov, "Stone-{W}ales-type transformations in carbon nanostructures driven by electron irradiation," *Phys. Rev. B*, vol. 83, no. 24, p. 245420, 2011.

[33] Y.-C. Lin, T. Björkman, H.-P. Komsa, P.-Y. Teng, C.-H. Yeh, F.-S. Huang, K.-H. Lin, J. Jadczak, Y.-S. Huang, P.-W. Chiu, A. V.

Krasheninnikov, and K. Suenaga, "Three-fold rotational defects in two-dimensional transition metal dichalcogenides," *Nature Communications*, vol. 6, p. 6736, 2015.

[34] J. D. Wadey, A. Markevich, A. Robertson, J. Warner, A. Kirkland, and E. Besley, "Mechanisms of monovacancy diffusion in graphene," *Chemical Physics Letters*, vol. 648, pp. 161–165, 2016.

[35] O. L. Krivanek, M. F. Chisholm, V. Nicolosi, T. J. Pennycook, G. J. Corbin, N. Dellby, M. F. Murfitt, C. S. Own, Z. S. Szilagyi, M. P. Oxley, S. T. Pantelides, and S. J. Pennycook, "Atom-by-atom structural and chemical analysis by annular dark-field electron microscopy," *Nature*, vol. 464, no. 7288, pp. 571–574, 2010.

[36] J. Kotakoski, C. Mangler, and J. C. Meyer, "Imaging atomic-level random walk of a point defect in graphene," *Nature Communications*, vol. 5, p. 3991, 2014.

[37] Z. Lin, B. R. Carvalho, E. Kahn, R. Lv, R. Rao, H. Terrones, M. A. Pimenta, and M. Terrones, "Defect engineering of two-dimensional transition metal dichalcogenides, 2016."

[38] H. P. Komsa, S. Kurasch, O. Lehtinen, U. Kaiser, and A. V. Krasheninnikov, "From point to extended defects in two-dimensional MoS2: Evolution of atomic structure under electron irradiation," *Physical Review B - Condensed Matter and Materials Physics*, vol. 88, no. 3, pp. 1–8, 2013.

[39] J. Kotakoski, A. V. Krasheninnikov, Y. Ma, A. S. Foster, K. Nordlund, and R. M. Nieminen, "B and N ion implantation into carbon nanotubes: Insight from atomistic simulations," *Phys. Rev. B*, vol. 71, no. 20, p. 205408, 2005.

[40] U. Bangert, W. Pierce, D. M. Kepaptsoglou, Q. Ramasse, R. Zan, M. H. Gass, J. A. den Berg, C. B. Boothroyd, J. Amani, and H. Hofsäss, "Ion Implantation of Graphene—Toward IC Compatible Technologies," *Nano Lett.*, vol. 13, no. 10, pp. 4902–4907, 2013.

[41] P. Willke, J. A. Amani, A. Sinterhauf, S. Thakur, T. Kotzott, T. Druga, K. Maiti, H. Hofsa, and M. Wenderoth, "Doping of Graphene by Low-Energy Ion Beam Implantation: Structural, Electronic, and Transport Properties, 2015."

[42] Y.-C. Lin, P.-Y. Teng, C.-H. Yeh, M. Koshino, P.-W. Chiu, and K. Suenaga, "Structural and Chemical Dynamics of Pyridinic-Nitrogen Defects in Graphene," *Nano Letters*, vol. 15, no. 11, pp. 7408–7413, 2015.

[43] C. Su, M. Tripathi, Q.-B. Yan, Z. Wang, Z. Zhang, L. Basile, G. Su, M. Dong, J. Kotakoski, J. Kong, J.-C. Idrobo, T. Susi, and J. Li, "Competing dynamics of single phosphorus dopant in graphene with electron irradiation," p. arXiv:1803.01369," 2018.

[44] T. Susi, J. Kotakoski, D. Kepaptsoglou, C. Mangler, T. C. Lovejoy, O. L. Krivanek, R. Zan, U. Bangert, P. Ayala, J. C. Meyer, and Q. Ramasse, "Silicon-carbon bond inversions driven by 60-kev electrons in graphene," *Physical Review Letters*, vol. 113, no. 11, pp. 1–5, 2014.

[45] Q. M. Ramasse, C. R. Seabourne, D.-m. Kepaptsoglou, R. Zan, U. Bangert, and A. J. Scott, "Probing the Bonding and Electronic Structure of Single Atom Dopants in Graphene with Electron Energy Loss Spectroscopy," *Nano Letters*, vol. 13, no. 10, pp. 4989–4995, 2013.

[46] T. Susi, T. P. Hardcastle, H. Hofsäss, A. Mittelberger, T. J. Pennycook, C. Mangler, R. Drummond-Brydson, A. J. Scott, J. C. Meyer, and J. Kotakoski, "Single-atom spectroscopy of phosphorus dopants implanted into graphene," *2D Materials*, vol. 4, no. 2, p. 21013, 2017.

[47] M. Tripathi, A. Markevich, R. Böttger, S. Facsko, E. Besley, J. Kotakoski, and T. Susi, "Implanting Germanium into Graphene," *ACS Nano*, vol. 12, no. 5, pp. 4641–4647, 2018.

[48] U. Bangert, A. Stewart, E. O'Connell, E. Courtney, Q. Ramasse, D. Kepatsoglou, H. Hofsäss, J. Amani, S.-S. Tu, and B. Kardynal, "Ion-beam modification of 2-D Materials - single implant atom analysis via annular dark-field electron microscopy," *Ultramicroscopy*," 2016.

[49] O. Lehtinen, N. Vats, G. Algara-Siller, P. Knyrim, and U. Kaiser, "Implantation and Atomic-Scale Investigation of Self-Interstitials in Graphene," *Nano Lett.*, vol. 15, no. 1, pp. 235–241, 2015.

[50] O. V. Yazyev and S. G. Louie, "Topological defects in graphene: Dislocations and grain boundaries," *Physical Review B - Condensed Matter and Materials Physics*, vol. 81, no. 19, 2010.

[51] A. Azizi, X. Zou, P. Ercius, Z. Zhang, A. L. Elías, N. Perea-López, G. Stone, M. Terrones, B. I. Yakobson, and N. Alem, "Dislocation motion and grain boundary migration in two-dimensional tungsten disulphide," *Nature Communications*, vol. 5, p. 4867, 2014.

[52] S. Kurasch, J. Kotakoski, O. J. Lehtinen, V. Skakalova, J. H. Smet, C. Krill, A. V. Krasheninnikov, and U. Kaiser, "Atom-by-Atom Observation of Grain Boundary Migration in Graphene," *Nano Lett.*, vol. 12, pp. 3168–3173, 2012.

[53] A. M. van der Zande, P. Y. Huang, D. A. Chenet, T. C. Berkelbach, Y. You, G.-H. Lee, T. F. Heinz, D. R. Reichman, D. A. Muller, and J. C. Hone, "Grains and grain boundaries in highly crystalline monolayer molybdenum disulphide," *Nature Materials*, vol. 12, p. 554, 2013.

[54] X. Zou, Y. Liu, and B. I. Yakobson, "Predicting dislocations and grain boundaries in two-dimensional metal-disulfides from the first principles," *Nano Letters*, vol. 13, no. 1, pp. 253–258, 2013.

[55] K. Elibol, T. Susi, M. O'Brien, B. C. Bayer, T. J. Pennycook, N. McEvoy, G. S. Duesberg, J. C. Meyer, and J. Kotakoski, "Grain boundary-mediated nanopores in molybdenum disulfide grown by chemical vapor deposition," *Nanoscale*, vol. 9, no. 4, pp. 1591–1598, 2017.

[56] S. Najmaei, Z. Liu, W. Zhou, X. Zou, G. Shi, S. Lei, B. I. Yakobson, J.-C. Idrobo, P. M. Ajayan, and J. Lou, "Vapour phase growth and grain boundary structure of molybdenum disulphide atomic layers," *Nature Mater.*, vol. 12, no. 8, pp. 754–759, 2013.

[57] P. Y. Huang, S. Kurasch, A. Srivastava, V. Skakalova, J. Kotakoski, A. V. Krasheninnikov, R. Hovden, Q. Mao, J. C. Meyer, J. Smet, D. A. Muller, and U. Kaiser, "Direct Imaging of a Two-Dimensional Silica Glass on Graphene," *Nano Lett.*, vol. 12, no. 2, pp. 1081–1086, 2012.

[58] L. M. Schleberger, O. Ochedowski, H. Lebius, B. Ban-d'Etat, C. H. Naylor, A. T. C. Johnson, J. Kotakoski, and Marika, "Defect engineering of single- and few-layer MoS 2 by swift heavy ion irradiation," *2D Materials*, vol. 4, no. 1, p. 15034, 2017.

[59] C. A. Merchant, K. Healy, M. Wanunu, V. Ray, N. Peterman, J. Bartel, M. D. Fischbein, K. Venta, Z. Luo, A. T. C. Johnson, and M. Drndić, "DNA Translocation through Graphene Nanopores," *Nano Letters*, vol. 10, no. 8, pp. 2915–2921, 2010.

[60] D. B. Williams and C. B. Carter, "The Transmission Electron Microscope BT - Transmission Electron Microscopy: A Textbook for Materials Science," pp. 3–22.

[61] O. L. Krivanek, N. Dellby, M. F. Murfitt, M. F. Chisholm, T. J. Pennycook, K. Suenaga, and V. Nicolosi, "Gentle STEM: ADF imaging and EELS at low primary energies," *Ultramicroscopy*, vol. 110, no. 8, pp. 935–945, 2010.

[62] O. L. Krivanek, G. J. Corbin, N. Dellby, B. F. Elston, R. J. Keyse, M. F. Murfitt, C. S. Own, Z. S. Szilagyi, and J. W. Woodruff, "An electron

microscope for the aberration-corrected era," *Ultramicroscopy*, vol. 108, no. 3, pp. 179–195, 2008.

[63] P. D. Nellist, 2008, vol. 113.

[64] A. V. Crewe, "The physics of the high-resolution scanning microscope," *Reports on Progress in Physics*, vol. 43, no. 5, p. 621, 1980.

[65] S. J. Pennycook and D. E. Jesson, "High-resolution Z-contrast imaging of crystals," *Ultramicroscopy*, vol. 37, no. 1, pp. 14–38, 1991.

[66] P. D. Nellist and S. J. Pennycook, "The principles and interpretation of annular dark-field Z-contrast imaging," vol. 113, pp. 147–203.

[67] R. F. Egerton, "Electron energy-loss spectroscopy in the TEM," *Reports on Progress in Physics*, vol. 72, no. 1, p. 16502, 2009.

[68] O. L. Krivanek, T. C. Lovejoy, M. F. Murfitt, G. Skone, P. E. Batson, and N. Dellby, "Towards sub-10 meV energy resolution STEM-EELS," *Journal of Physics: Conference Series*, vol. 522, no. 1, p. 12023, 2014.

[69] F. Hofer, F. P. Schmidt, W. Grogger, and G. Kothleitner, "Fundamentals of electron energy-loss spectroscopy," *IOP Conference Series: Materials Science and Engineering*, vol. 109, no. 1, 2016.

[70] Graphenea, "Graphenea.Inc, 2018."

[71] P. Blake, E. W. Hill, A. H. Castro Neto, K. S. Novoselov, D. Jiang, R. Yang, T. J. Booth, and A. K. Geim, "Making graphene visible," *Applied Physics Letters*, vol. 91, no. 6, p. 63124, 2007.

[72] M. Regmi, M. F. Chisholm, and G. Eres, "The effect of growth parameters on the intrinsic properties of large-area single layer graphene grown by chemical vapor deposition on Cu," *Carbon*, vol. 50, no. 1, pp. 134–141, 2012.

[73] X. Li, C. W. Magnuson, A. Venugopal, J. An, J. W. Suk, B. Han, M. Borysiak, W. Cai, A. Velamakanni, Y. Zhu, L. Fu, E. M. Vogel, E. Voelkl, L. Colombo, and R. S. Ruoff, "Graphene Films with Large Domain Size by a Two-Step Chemical Vapor Deposition Process," *Nano Letters*, vol. 10, no. 11, pp. 4328–4334, 2010.

[74] E.-X. Ding, H. Jiang, Q. Zhang, Y. Tian, P. Laiho, A. Hussain, Y. Liao, N. Wei, and E. I. Kauppinen, "Highly conductive and transparent single-walled carbon nanotube thin films from ethanol by floating catalyst chemical vapor deposition," *Nanoscale*, vol. 9, no. 44, pp. 17 601–17 609, 2017.

[75] Z. Li, Y. Wang, A. Kozbial, G. Shenoy, F. Zhou, R. McGinley, P. Ireland, B. Morganstein, A. Kunkel, S. P. Surwade, L. Li, and H. Liu, "Effect of airborne contaminants on the wettability of supported graphene and graphite," *Nat Mater*, vol. 12, no. 10, pp. 925–931, 2013.

[76] W. Xie, L.-T. Weng, K. M. Ng, C. K. Chan, and C.-M. Chan, "Clean graphene surface through high temperature annealing," *Carbon*, vol. 94, pp. 740–748, 2015.

[77] G. Algara-Siller, O. Lehtinen, A. Turchanin, and U. Kaiser, "Dry-cleaning of graphene," *Applied Physics Letters*, vol. 104, no. 15, p. 153115, 2014.

[78] M. Schleberger and J. Kotakoski, "2D Material Science: Defect Engineering by Particle Irradiation," *Materials*, vol. 11, no. 10, p. 1885, 2018.

[79] J. F. Ziegler and J. P. Biersack, "The Stopping and Range of Ions in Matter BT - Treatise on Heavy-Ion Science: Volume 6: Astrophysics, Chemistry, and Condensed Matter," pp. 93–129.

[80] A. V. Krasheninnikov and F. Banhart, "Engineering of nanostructured carbon materials with electron or ion beams," *Nature Materials*, vol. 6, p. 723, 2007.

[81] E. Balanzat and S. Bouffard, "Basic Phenomena of the Particle-Matter Interaction," *Solid State Phenomena*, vol. 30-31, pp. 7–74, 1992.

[82] E. H. Åhlgren, J. Kotakoski, and A. V. Krasheninnikov, "Atomistic simulations of the implantation of low-energy boron and nitrogen ions into graphene," *Phys. Rev. B*, vol. 83, no. 11, p. 115424, 2011.

[83] W. Li and J. Xue, "Ion implantation of low energy Si into graphene: insight from computational studies," *RSC Adv.*, vol. 5, no. 121, pp. 99 920–99 926, 2015.

[84] U. Bangert, A. Stewart, E. O'Connell, E. Courtney, Q. Ramasse, D. Kepatsoglou, H. Hofsäss, J. Amani, J.-S. Tu, and B. Kardynal, "Ion-beam modification of 2-D materials - single implant atom analysis via annular dark-field electron microscopy," *Ultramicroscopy*, pp. –, 2016.

[85] F. Aumayr, H. Kurz, D. Schneider, M. A. Briere, J. W. McDonald, C. E. Cunningham, and H. P. Winter, "Emission of electrons from a clean gold surface induced by slow, very highly charged ions at the image charge acceleration limit," *Phys. Rev. Lett.*, vol. 71, no. 12, pp. 1943–1946, 1993.

[86] F. Aumayr, S. Facsko, A. S. El-Said, C. Trautmann, and M. Schleberger, "Single ion induced surface nanostructures: a comparison between slow highly charged and swift heavy ions," *Journal of Physics: Condensed Matter*, vol. 23, no. 39, p. 393001, 2011.

[87] S. Knust, D. Kreft, R. Hillmann, A. Meyer, M. Viefhues, P. Reimann, and D. Anselmetti, "Measuring DNA Translocation Forces through MoS2-Nanopores with Optical Tweezers," *Materials Today: Proceedings*, vol. 4, pp. S168–S173, 2017.

[88] M. Ghorbani-Asl, S. Kretschmer, D. Spearot, and A. V. Krasheninnikov, "Two-dimensional MoS2 under ion irradiation: from controlled defect production to electronic structure engineering," *2D Materials*, vol. 110, no. 1, pp. 76–91, 2017.

[89] J. Hopster, R. Kozubek, J. Krämer, V. Sokolovsky, and M. Schleberger, "Ultra-thin MoS2 irradiated with highly charged ions," *Nuclear Instruments and Methods in Physics Research Section B: Beam Interactions with Materials and Atoms*, vol. 317, pp. 165–169, 2013.

[90] J. H. Schleberger, R. Kozubek, B. Ban-d'Etat, S. Guillous, H. Lebius, and M, "Damage in graphene due to electronic excitation induced by highly charged ions," *2D Materials*, vol. 1, no. 1, p. 11011, 2014.

[91] R. Ritter, R. A. Wilhelm, M. Stöger-Pollach, R. Heller, A. Mücklich, U. Werner, H. Vieker, A. Beyer, S. Facsko, A. Gölzhäuser, and F. Aumayr, "Fabrication of nanopores in 1 nm thick carbon nanomembranes with slow highly charged ions," *Applied Physics Letters*, vol. 102, no. 6, pp. 1–5, 2013.

[92] E. Gruber, R. A. Wilhelm, R. Pétuya, V. Smejkal, R. Kozubek, A. Hierzenberger, B. C. Bayer, I. Aldazabal, A. K. Kazansky, F. Libisch, A. V. Krasheninnikov, M. Schleberger, S. Facsko, A. G. Borisov, A. Arnau, and F. Aumayr, "Ultrafast electronic response of graphene to a strong and localized electric field," *Nature Communications*, vol. 7, p. 13948, 2016.

[93] R. Zan, Q. M. Ramasse, U. Bangert, and K. S. Novoselov, "Graphene Reknits Its Holes," *Nano Letters*, vol. 12, no. 8, pp. 3936–3940, 2012.

[94] R. Kozubek, P. Ernst, C. Herbig, T. Michely, and M. Schleberger, "Fabrication of Defective Single Layers of Hexagonal Boron Nitride on Various Supports for Potential Applications in Catalysis and DNA Sequencing," *ACS Applied Nano Materials*, vol. 1, no. 8, pp. 3765–3773, 2018.

[95] T. Peters, C. Haake, J. Hopster, V. Sokolovsky, A. Wucher, and M. Schleberger, "HICS: Highly charged ion collisions with surfaces," *Nuclear Instruments and Methods in Physics Research Section B: Beam Interactions with Materials and Atoms*, vol. 267, no. 4, pp. 687–690, 2009.

[96] R. F. Egerton, P. Li, and M. Malac, "Radiation damage in the TEM and SEM," *Micron*, vol. 35, no. 6, pp. 399–409, 2004.

[97] R. F. Egerton, "Control of radiation damage in the {TEM}," *Ultramicroscopy*, vol. 127, pp. 100–108, 2013.

[98] F. Banhart, "Irradiation effects in carbon nanostructures," *Rep. Prog. Phys.*, vol. 62, no. 8, p. 1181, 1999.

[99] H. P. Komsa, J. Kotakoski, S. Kurasch, O. Lehtinen, U. Kaiser, and A. V. Krasheninnikov, "Two-dimensional transition metal dichalcogenides under electron irradiation: Defect production and doping," *Physical Review Letters*, vol. 109, no. 3, pp. 1–5, 2012.

[100] T. Lehnert, O. Lehtinen, G. AlgaraSiller, and U. Kaiser, "Electron radiation damage mechanisms in 2D MoSe2," *Applied Physics Letters*, vol. 110, no. 3, p. 33106, 2017.

[101] F. Banhart, "the Formation and Transformation of Carbon Nanoparticles Under Electron Irradiation," p. 89069," 2004.

[102] A. Zobelli, A. Gloter, C. P. Ewels, G. Seifert, and C. Colliex, "Electron knock-on cross section of carbon and boron nitride nanotubes," *Phys. Rev. B*, vol. 75, no. 24, p. 245402, 2007.

[103] J. C. Meyer, F. Eder, S. Kurasch, V. Skakalova, J. Kotakoski, H. J. Park, S. Roth, A. Chuvilin, S. Eyhusen, G. Benner, A. V. Krasheninnikov, and U. Kaiser, "Accurate measurement of electron beam induced displacement cross sections for single-layer graphene," *Phys. Rev. Lett.*, vol. 108, no. 19, p. 196102, 2012.

[104] M. N. Francis and B. N. H. David, "The scattering of fast electrons by atomic nuclei," *Proceedings of the Royal Society of London. Series A, Containing Papers of a Mathematical and Physical Character*, vol. 124, no. 794, pp. 425–442, 1929.

[105] W. A. McKinley Jr. and H. Feshbach, "The {C}oulomb Scattering of Relativistic Electrons by Nuclei," *Phys. Rev.*, vol. 74, no. 12, pp. 1759–1763, 1948.

[106] J. C. Meyer, F. Eder, S. Kurasch, V. Skakalova, J. Kotakoski, H. J. Park, S. Roth, A. Chuvilin, S. Eyhusen, G. Benner, A. V. Krasheninnikov, and U. Kaiser, "Accurate measurement of electron beam induced displacement cross sections for single-layer graphene," *Physical Review Letters*, vol. 108, no. 19, pp. 1–6, 2012.

[107] T. Susi, C. Hofer, G. Argentero, G. T. Leuthner, T. J. Pennycook, C. Mangler, J. C. Meyer, and J. Kotakoski, "Isotope analysis in the transmission electron microscope," *Nature Communications*, vol. 7, no. May, pp. 1–8, 2016.

[108] D. M. Eigler and E. K. Schweizer, "Positioning single atoms with a scanning tunnelling microscope," *Nature*, vol. 344, no. 6266, pp. 524–526, 1990.

[109] M. F. Crommie, C. P. Lutz, and D. M. Eigler, "Confinement of Electrons to Quantum Corrals on a Metal Surface," *Science*, vol. 262, no. 5131, pp. 218–220, 1993.

[110] F. E. Kalff, M. P. Rebergen, E. Fahrenfort, J. Girovsky, R. Toskovic, J. L. Lado, J. Fernández-Rossier, and A. F. Otte, "A kilobyte rewritable atomic memory," *Nature Nanotechnology*, vol. 11, pp. 926–929, 2016.

[111] T. Susi, J. C. Meyer, and J. Kotakoski, "Manipulating low-dimensional materials down to the level of single atoms with electron irradiation," vol. 0, pp. 1–10, 2017.

[112] M. Tripathi, A. Markevich, R. Böttger, S. Facsko, E. Besley, J. Kotakoski, and T. Susi, "Implanting Germanium into Graphene," *ACS Nano*, vol. 12, no. 5, pp. 4641–4647, 2018.

[113] T. Susi, J. Kotakoski, R. Arenal, S. Kurasch, H. Jiang, V. Skakalova, O. Stephan, A. V. Krasheninnikov, E. I. Kauppinen, U. Kaiser, and J. C. Meyer, "Atomistic Description of Electron Beam Damage in Nitrogen-Doped Graphene and Single-Walled Carbon Nanotubes," *ACS Nano*, vol. 6, no. 10, pp. 8837–8846, 2012.

[114] C. Hofer, V. Skakalova, M. R. A. Monazam, C. Mangler, J. Kotakoski, T. Susi, and J. C. Meyer, "Direct visualization of the 3D structure of silicon impurities in graphene," pp. 1–13," 2018.

[115] T. Susi, J. Kotakoski, D. Kepaptsoglou, C. Mangler, T. C. Lovejoy, O. L. Krivanek, R. Zan, U. Bangert, P. Ayala, J. C. Meyer, and Q. Ramasse, "Silicon–Carbon Bond Inversions Driven by 60-ke{V} Electrons in Graphene," *Phys. Rev. Lett.*, vol. 113, no. 11, p. 115501, 2014.

[116] H. Y. Nan, Z. H. Ni, J. Wang, Z. Zafar, Z. X. Shi, and Y. Y. Wang, "The thermal stability of graphene in air investigated by Raman spectroscopy," *Journal of Raman Spectroscopy*, vol. 44, no. 7, pp. 1018–1021, 2013.

[117] K. Kim, W. Regan, B. Geng, B. Alemán, B. M. Kessler, F. Wang, M. F. Crommie, and A. Zettl, "High-temperature stability of suspended single-layer graphene," *Physica Status Solidi - Rapid Research Letters*, vol. 4, no. 11, pp. 302–304, 2010.

[118] W. Gao and R. Huang, "Thermomechanics of monolayer graphene: Rippling, thermal expansion and elasticity," *Journal of the Mechanics and Physics of Solids*, vol. 66, pp. 42–58, 2014.

[119] F. C. Nix and D. MacNair, "The Thermal Expansion of Pure Metals: Copper, Gold, Aluminum, Nickel, and Iron," *Phys. Rev.*, vol. 60, no. 8, pp. 597–605, 1941.

[120] T. J. Booth, P. Blake, R. R. Nair, D. Jiang, E. W. Hill, U. Bangert, A. Bleloch, M. Gass, K. S. Novoselov, M. I. Katsnelson, and A. K. Geim, "Macroscopic Graphene Membranes and Their Extraordinary Stiffness," *Nano Letters*, vol. 8, no. 8, pp. 2442–2446, 2008.

[121] M. Tripathi, A. Mittelberger, K. Mustonen, C. Mangler, J. Kotakoski, J. C. Meyer, and T. Susi, "Cleaning graphene: Comparing heat treatments in air and in vacuum, 2017."

[122] M. H. Rummeli, H. Q. Ta, R. G. Mendes, I. G. Gonzalez-Martinez, L. Zhao, J. Gao, L. Fu, T. Gemming, A. Bachmatiuk, and Z. Liu, "New Frontiers in Electron BeamDriven Chemistry in and around Graphene," *Advanced Materials*, vol. 0, no. 0, p. 1800715.

[123] J. C. Meyer, C. O. Girit, M. F. Crommie, and A. Zettl, "Hydrocarbon lithography on graphene membranes," *Applied Physics Letters*, vol. 92, no. 12, p. 123110, 2008.

[124] T. Susi, M. Scardamaglia, K. Mustonen, M. Tripathi, A. Mittelberger, M. Al-Hada, M. Amati, H. Sezen, P. Zeller, A. H. Larsen, C. Mangler, J. C. Meyer, L. Gregoratti, C. Bittencourt, and J. Kotakoski, "Intrinsic core level photoemission of suspended monolayer graphene," *Phys. Rev. Materials*, vol. 2, no. 7, p. 74005, 2018.

[125] G. Schiwietz, M. Briere, D. Schneider, J. McDonald, and C. Cunningham, "Measurement of negative-ion and -cluster sputtering with highly-charged heavy ions," *Nuclear Instruments and Methods in Physics Research Section B: Beam Interactions with Materials and Atoms*, vol. 100, no. 1, pp. 47–54, 1995.

[126] W. Li, X. Wang, X. Zhang, S. Zhao, H. Duan, and J. Xue, "Mechanism of the Defect Formation in Supported Graphene by Energetic Heavy Ion Irradiation: the Substrate Effect," *Scientific Reports*, vol. 5, p. 9935, 2015.

[127] S. Kretschmer, M. Maslov, S. Ghaderzadeh, M. Ghorbani-Asl, G. Hlawacek, and A. V. Krasheninnikov, "Supported Two-Dimensional Materials under Ion Irradiation: The Substrate Governs Defect Production," *ACS Applied Materials & Interfaces*, vol. 10, no. 36, pp. 30 827–30 836, 2018.

[128] R. A. Wilhelm, E. Gruber, J. Schwestka, R. Kozubek, T. I. Madeira, J. P. Marques, J. Kobus, A. V. Krasheninnikov, M. Schleberger, and F. Aumayr, "Interatomic Coulombic Decay: The Mechanism for Rapid Deexcitation of Hollow Atoms," *Phys. Rev. Lett.*, vol. 119, no. 10, p. 103401, 2017.

[129] H.-P. Komsa, S. Kurasch, O. Lehtinen, U. Kaiser, and A. V. Krasheninnikov, "From point to extended defects in two-dimensional MoS$\{\}_\{2\}$: Evolution of atomic structure under electron irradiation," *Phys. Rev. B*, vol. 88, no. 3, p. 35301, 2013.

[130] M. Heiranian, A. B. Farimani, and N. R. Aluru, "Water desalination with a single-layer MoS2 nanopore," *Nature Communications*, vol. 6, p. 8616, 2015.

[131] J. Feng, K. Liu, R. D. Bulushev, S. Khlybov, D. Dumcenco, A. Kis, and A. Radenovic, "Identification of single nucleotides in MoS2 nanopores," *Nature Nanotechnology*, vol. 10, p. 1070, 2015.

[132] W. Zhou, X. Zou, S. Najmaei, Z. Liu, Y. Shi, J. Kong, J. Lou, P. M. Ajayan, B. I. Yakobson, and J.-C. Idrobo, "Intrinsic Structural Defects in Monolayer Molybdenum Disulfide," *Nano Letters*, vol. 13, no. 6, pp. 2615–2622, 2013.

[133] S. Wang, H. Sawada, X. Han, S. Zhou, S. Li, Z. X. Guo, A. I. Kirkland, and J. H. Warner, "Preferential Pt Nanocluster Seeding at Grain Boundary Dislocations in Polycrystalline Monolayer MoS2," *ACS Nano*, vol. 12, no. 6, pp. 5626–5636, 2018.

[134] T. H. Ly, J. Zhao, M. O. Cichocka, L.-J. Li, and Y. H. Lee, "Dynamical observations on the crack tip zone and stress corrosion of two-dimensional MoS2," *Nature Communications*, vol. 8, p. 14116, 2017.

[135] S. Wang, Z. Qin, G. S. Jung, F. J. Martin-Martinez, K. Zhang, M. J. Buehler, and J. H. Warner, "Atomically Sharp Crack Tips in Monolayer

MoS2 and Their Enhanced Toughness by Vacancy Defects," *ACS Nano*, vol. 10, no. 11, pp. 9831–9839, 2016.

[136] O. V. Yazyev and S. G. Louie, "Electronic transport in polycrystalline graphene," *Nature Materials*, vol. 9, no. 10, pp. 806–809, 2010.

[137] M. J. Hÿtch, E. Snoeck, and R. Kilaas, "Quantitative measurement of displacement and strain fields from HREM micrographs," *Ultramicroscopy*, vol. 74, no. 3, pp. 131–146, 1998.

[138] V. Grillo, "Advances in STEM-CELL. A Free Software for TEM and STEM Analysis and Simulations: Probe Deconvolution in STEM-HAADF," *Microscopy and Microanalysis*, vol. 17, no. S2, pp. 1292–1293, 2011.

[139] F. C. Frank, "Martensite," *Acta Metallurgica*, vol. 1, no. 1, pp. 15–21, 1953.

[140] R. Bullough and B. A. Bilby, "Continuous Distributions of Dislocations: Surface Dislocations and the Crystallography of Martensitic Transformations," *Proceedings of the Physical Society. Section B*, vol. 69, no. 12, pp. 1276–1286, 1956.

[141] B. A. Bilby and F. C. Frank, "The analysis of the crystallography of martensitic transformations by the method of prism matching," *Acta Metallurgica*, vol. 8, no. 4, pp. 239–248, 1960.

[142] B. A. Bradley, R. W. Jacob, J. F. Hermance, and J. F. Mustard, "A curve fitting procedure to derive inter-annual phenologies from time series of noisy satellite NDVI data," *Remote Sensing of Environment*, vol. 106, no. 2, pp. 137–145, 2007.

[143] W. Zhou, M. D. Kapetanakis, M. P. Prange, S. T. Pantelides, S. J. Pennycook, and J.-C. Idrobo, "Direct Determination of the Chemical Bonding of Individual Impurities in Graphene," *Phys. Rev. Lett.*, vol. 109, no. 20, p. 206803, 2012.

[144] T. Susi, J. Meyer, and J. Kotakoski, "Manipulating low-dimensional materials down to the level of single atoms with electron irradiation," *Ultramicroscopy*, vol. in press, 2017.

[145] M. L. Ould Ne, A. Abbassi, A. G. El hachimi, A. Benyoussef, H. Ez-Zahraouy, and A. El Kenz, "Electronic optical, properties and widening band gap of graphene with Ge doping," *Optical and Quantum Electronics*, vol. 49, no. 6, 2017.

[146] P. A. Denis, "Chemical Reactivity and Band-Gap Opening of Graphene Doped with Gallium, Germanium, Arsenic, and Selenium Atoms," *ChemPhysChem*, vol. 15, no. 18, pp. 3994–4000, 2014.

[147] D. Kepaptsoglou, T. P. Hardcastle, C. R. Seabourne, U. Bangert, R. Zan, J. A. Amani, H. Hofsa, R. J. Nicholls, R. M. D. Brydson, A. J. Scott, and Q. M. Ramasse, "Electronic Structure Modi fi cation of Ion Implanted Graphene : The Spectroscopic Signatures of p- and nType Doping," *ACS Nano*, vol. 9, no. 11, pp. 11 398–11 407, 2015.

[148] U. Bangert, W. Pierce, D. M. Kepaptsoglou, Q. Ramasse, R. Zan, M. H. Gass, J. A. Van den Berg, C. B. Boothroyd, J. Amani, and H. Hofsäss, "Ion Implantation of GrapheneToward IC Compatible Technologies," *Nano Letters*, vol. 13, no. 10, pp. 4902–4907, 2013.

[149] W. Zhou, J. Lee, J. Nanda, S. T. Pantelides, S. J. Pennycook, and J.-C. Idrobo, "Atomically localized plasmon enhancement in monolayer graphene," *Nat. Nanotechnol.*, vol. 7, no. 3, pp. 161–165, 2012.

[150] F. S. Hage, T. P. Hardcastle, M. N. Gjerding, D. M. Kepaptsoglou, C. R. Seabourne, K. T. Winther, R. Zan, J. A. Amani, H. C. Hofsaess, U. Bangert, K. S. Thygesen, and Q. M. Ramasse, "Local Plasmon Engineering in Doped Graphene," *ACS Nano*, vol. 12, no. 2, pp. 1837–1848, 2018.

[151] T. Susi, C. Hofer, G. Argentero, G. T. Leuthner, T. J. Pennycook, C. Mangler, J. C. Meyer, and J. Kotakoski, "Isotope analysis in the transmission electron microscope," *Nature Communications*, vol. 7, no. May, p. 13040, 2016.

[152] O. Lehtinen, S. Kurasch, A. V. Krasheninnikov, and U. Kaiser, "Atomic scale study of the life cycle of a dislocation in graphene from birth to annihilation," *Nature Communications*, vol. 4, p. 2098, 2013.

[153] T. Susi, D. Kepaptsoglou, Y.-C. Lin, Q. Ramasse, J. C. Meyer, K. Suenaga, and J. Kotakoski, "Towards atomically precise manipulation of 2D nanostructures in the electron microscope," *2D Mater.*, vol. 4, no. 042004, p. 42004, 2017.

[154] O. Dyck, S. Kim, S. V. Kalinin, and S. Jesse, "Placing single atoms in graphene with a scanning transmission electron microscope," *Appl. Phys. Lett.*, vol. 111, no. 11, p. 113104, 2017.

[155] O. Dyck, S. Kim, E. Jimenez-Izal, A. Alexandrova, S. Kalinin, and S. Jesse, "Assembling Di- and Multiatomic Si Clusters in Graphene via Electron Beam Manipulation, 2017."

[156] J. Lee, W. Zhou, S. J. Pennycook, J.-C. Idrobo, and S. T. Pantelides, "Direct visualization of reversible dynamics in a {Si}$_6$ cluster embedded in a graphene pore," *Nature*, vol. 4, p. 1650, 2013.

[157] R. Nieman, A. J. A. Aquino, T. P. Hardcastle, J. Kotakoski, T. Susi, and H. Lischka, "Structure and electronic states of a graphene double vacancy with an embedded Si dopant," *J. Chem. Phys.*, vol. 147, no. 19, p. 194702, 2017.

[158] R. Arenal, K. March, C. P. Ewels, X. Rocquefelte, M. Kociak, A. Loiseau, and O. Stéphan, "Atomic Configuration of Nitrogen-Doped Single-Walled Carbon Nanotubes," *Nano Letters*, vol. 14, no. 10, pp. 5509–5516, 2014.

[159] R. F. Egerton, "Beam-Induced Motion of Adatoms in the Transmission Electron Microscope," *Microscopy and Microanalysis*, vol. 19, no. 02, pp. 479–486, 2013.

[160] S. T. Skowron, V. O. Koroteev, M. Baldoni, S. Lopatin, A. Zurutuza, A. Chuvilin, and E. Besley, "Reaction kinetics of bond rotations in graphene," *Carbon*, vol. 105, pp. 176–182, 2016.

[161] M. Tripathi, A. Mittelberger, N. Pike, C. Mangler, J. Meyer, M. Verstraete, J. Kotakoski, and T. Susi, "Electron-Beam Manipulation of Silicon Dopants in Graphene," *Nano Letters*," 2018.

[162] J. Kotakoski, J. C. Meyer, S. Kurasch, D. Santos-Cottin, U. Kaiser, and A. V. Krasheninnikov, "Stone-Wales-type transformations in carbon nanostructures driven by electron irradiation," *Physical Review B - Condensed Matter and Materials Physics*, vol. 83, no. 24, pp. 1–6, 2011.

[163] H. Inani, K. Mustonen, A. Markevich, E.-X. Ding, M. Tripathi, A. Hussain, C. Mangler, E. I. Kauppinen, T. Susi, and J. Kotakoski, "Si Substitution in Nanotubes and Graphene via Intermittent Vacancies," *ArXiv:1902.0261*," 2019.

[164] K. Mustonen, A. Markevich, M. Tripathi, H. Inani, E.-X. Ding, A. Hussain, C. Mangler, E. I. Kauppinen, J. Kotakoski, and T. Susi, *ArXiv:1902.03972*.

[165] B. M. Hudak, J. Song, H. Sims, M. C. Troparevsky, T. S. Humble, S. T. Pantelides, P. C. Snijders, and A. R. Lupini, "Directed Atom-by-Atom Assembly of Dopants in Silicon," *ACS Nano*," 2018.